

Range Dependent Matched Field Source Localization and Tracking in
Shallow Water on a Continental Slope Region of the North-East
Pacific Ocean

S. 240
2/89

Lieutenant(N) Martin L. Taillefer
D.E.C., College Militaire Royal de St-Jean, 1984
B. Sc., Royal Roads Military College, 1987

A Thesis submitted in Partial Fulfillment of the Requirements for the Degree of

**RANGE DEPENDENT MATCHED FIELD SOURCE
LOCALIZATION AND TRACKING IN SHALLOW WATER ON
A CONTINENTAL SLOPE REGION OF THE NORTH-EAST
PACIFIC OCEAN**

[Signature]
Dr. B.R. Chapman, Supervisor (School of Earth and Ocean Science)

by
[Signature]
Dr. S.E. Dosso, Departmental Member (School of Earth and Ocean Science)

[Signature]
Lieutenant(N) Martin L. Taillefer
Dr. G. Spence, Departmental Member (School of Earth and Ocean Science)

[Signature]
Dr. A. Zielinski, Outside Member (Department of Electrical Engineering)

[Signature]
Dr. M. Wilmut, External Examiner (Department of Mathematics, Royal Military
College of Canada, Kingston)

© Lieutenant(N) Martin L. Taillefer, 1998
UNIVERSITY OF VICTORIA

All rights reserved. This work may not be reproduced, stored in a retrieval system, or transmitted in whole or in part, by photocopy or other means, without the permission of the author.

Range Dependent Matched Field Source Localization and Tracking in
Shallow Water on a Continental Slope Region of the North-East
Pacific Ocean

by

Supervisor: Dr. N.R. Chapman

Lieutenant(N) Martin L. Taillefer

D.E.C., College Militaire Royal de St-Jean, 1984

B. Sc., Royal Roads Military College, 1987

Source tracking using a vertical line array (VLA) is not possible in general unless the

A Thesis submitted in Partial Fulfillment of the Requirements for the Degree of

matched-field (MF) source localization data from an experiment over the continental slope

off Vancouver Island. A CW source was towed along a radial track over the slope out to

ranges of 5.5 km, and then along a navigational arc in water depths from 380 m at the

array to 750 m. The data were collected using a multi-element vertical line array (MEVA).

The MEVA We accept this thesis as conforming to the required standard in 90 m and

MASTER OF SCIENCE

in the

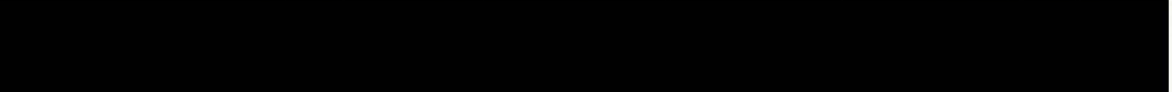
SCHOOL OF EARTH AND OCEAN SCIENCE



Dr. N.R. Chapman, Supervisor (School of Earth and Ocean Science)



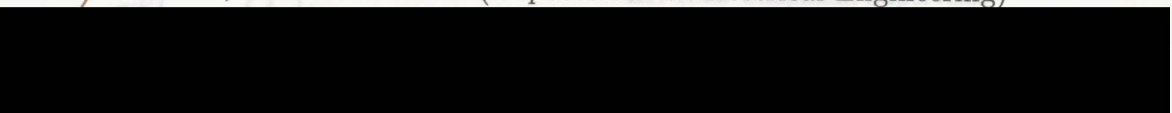
Dr. S.E. Dosso, Departmental Member (School of Earth and Ocean Science)



Dr. G. Spence, Departmental Member (School of Earth and Ocean Science)



Dr. A. Zielinski, Outside Member (Department of Electrical Engineering)



Dr. M. Wilmot, External Examiner (Department of Mathematics, Royal Military
College of Canada, Kingston)

Dr. G. Spence, Department Member
(School of Earth and Ocean Science)

© Lieutenant(N) Martin L. Taillefer, 1998
UNIVERSITY OF VICTORIA

All rights reserved. This thesis may not be reproduced in whole or in part,
by photocopy or other means, without the permission of the author.

Royal Military College of Canada, Kingston

Supervisor: Dr. N.R. Chapman

Abstract

Source tracking using a vertical line array (VLA) is not possible in general unless the cylindrical symmetry of the acoustic field is broken. This thesis describes the analysis of matched-field (MF) source localization data from an experiment over the continental slope off Vancouver Island. A CW source was towed along a radial track over the slope out to ranges of 5.5 km, and then along a navigational arc in water depths from 380 m at the array to 750 m. The data were collected using a multi-element vertical line array (MEVA). The MEVA is a 16-element array with sensors evenly spaced at depths between 90 m and 315 m. The environment was modelled using an *adiabatic normal mode* approximation that accounted for elastic wave propagation in the sediment layers. A bathymetric database of the experimental region was compiled to provide a reliable set of depth contours used for computing the acoustic replica-fields. Using a Bartlett MF processor, the source was tracked in *range, depth and bearing* over the duration of the track, with Bartlett processor values of up to 0.88. The analysis and results presented here demonstrate remarkably good tracking performance indicating that the slope is effective in breaking the symmetry of the acoustic field to provide bearing resolution with a VLA.

Examiners:

Dr. S.E. Dosso, Department Member
(School of Earth and Ocean Science)

Dr. A. Zielinski, Outside Member
(Department of Electrical Engineering)

Dr. N.R. Chapman, Supervisor
(School of Earth and Ocean Science)

Dr. G. Spence, Department Member
(School of Earth and Ocean Science)

Dr. M. Wilmut, External Examiner
(Department of Mathematics,
Royal Military College of Canada, Kingston)

| | |
|--|-----------|
| 3 Matched Field Source Localization | 41 |
| 3.1 Matched Field Processing | 41 |
| 3.1.1 Measured Signal | 42 |
| 3.1.2 The Bartlett Processor | 43 |
| 1 The Transparent Ocean | 1 |
| 1.1 Historical | 1 |
| 1.2 Shallow Water Environmental Factors | 4 |
| 1.2.1 Continental Slope | 6 |
| 1.2.2 Horizontal Refraction | 8 |
| 1.3 Pacific Shelf Experiment | 9 |
| 1.4 Purpose and Scope of Thesis | 12 |
| 2 Acoustic Modelling | 15 |
| 2.1 The Wave Equation | 15 |
| 2.1.1 Helmholtz Equation | 16 |
| 2.2 The Method of Normal Modes | 16 |
| 2.3 Multi-Layered Acousto-Elastic Ocean Environment Modelling | 21 |
| 2.3.1 Parabolic Equation Method - Range-dependent Acoustic Model (RAM) | 21 |
| 2.3.2 Normal Mode Method - Range-independent Acoustic Model (ORCA) | 21 |
| 2.3.3 ORCA - General Derivation | 22 |
| 2.3.4 Adiabatic Normal Mode Method (OAR) | 24 |
| 2.3.5 Reciprocity of the Adiabatic Approximation | 27 |
| 2.4 OAR model Formulation | 29 |
| 2.4.1 Wave Number and Mode Function Lookup Tables | 30 |
| 2.5 OAR model Validation | 35 |
| 6.1.1 Adiabatic Reciprocity | 97 |

| | | |
|----------|--|-----------|
| 3 | Matched Field Source Localization | 41 |
| 3.1 | Matched Field Processing | 41 |
| 3.1.1 | Measured Signal | 42 |
| 3.1.2 | The Bartlett Processor | 43 |
| 3.1.3 | Cross-Spectral Matrix | 44 |
| 3.2 | Matched Field Validation | 46 |
| 3.2.1 | Mismatch and Errors | 48 |
| 3.3 | MFP Tracking (N x 2D) | 51 |
| 4 | Ocean Acoustics Sea Trial - Pacific Shelf (MEVA 5) | 54 |
| 4.1 | Oceanography | 56 |
| 4.1.1 | Bathymetric Database | 56 |
| 4.1.2 | Geoacoustic data | 58 |
| 4.1.3 | Sound Speed Profile | 62 |
| 4.2 | Array Drift | 65 |
| 4.3 | Received Signal Processing | 67 |
| 5 | Matched-Field Localization and Surface to Surface Tracking | 71 |
| 5.1 | Observation 1: OAR model propagation results | 72 |
| 5.2 | Observation 2: Matched-field localization - azimuth assumed known | 74 |
| 5.3 | Observation 3: Horizontal refraction | 77 |
| 5.4 | Observation 4: Matched-field localization - source azimuth unknown | 80 |
| 5.5 | Observation 5: Tracking results | 85 |
| 5.6 | Observation 6: Range Versus Time Tracking | 92 |
| 5.7 | Observation 7: Model Comparisons | 94 |
| 6 | Conclusion | 96 |
| 6.1 | Acoustic Modelling | 96 |
| 6.1.1 | Adiabatic Reciprocity | 97 |

| | | |
|-----------------------------------|--|------------|
| 6.1.2 | Horizontal Refraction | 97 |
| 6.2 | Matched-Field Localization | 98 |
| 6.3 | Concepts and Scope of Matched-Field Tracking | 100 |
| 6.3.1 | Defence Needs for Progress in Matched-Field Processing Local- ization and Tracking Techniques | 100 |
| 6.3.2 | Rapid Environmental Assessment (REA) | 101 |
| References | | 103 |
| Appendix A OAR - IDL Codes | | 108 |
| A.1 | Reading Lookup Tables | 108 |
| A.2 | Radial depths and coordinate information | 108 |
| A.3 | Wave number interpolation and integration | 110 |
| A.4 | Mode function interpolation | 111 |
| A.5 | Adiabatic summation | 111 |
| Appendix B MFP - IDL Codes | | 113 |
| B.1 | Linear Processor: Bartlett | 113 |

List of Tables

| | | |
|------|--|----|
| 3.1 | Match-Field Power Values (Validation case) | 46 |
| 4.1 | Bathymetric database sources | 57 |
| 4.2 | Continental shelf and slope geoacoustic properties | 60 |
| 4.3 | Geoacoustic properties based on the Hannay & Chapman (1996) report of a three-layer system | 61 |
| 4.4 | Geoacoustic properties based on OAR/MFP inversions | 61 |
| 4.5 | Sound Speed profile information: 15 Sep 93 | 62 |
| 5.1 | Summary of MFP from selected radials | 75 |
| 5.2 | Occurrences of horizontal refraction | 78 |
| 5.3 | Target Tracking Summary | 86 |
| 5.4 | Model comparison | 94 |
| 2.7 | ASA Benchmark comparison | 36 |
| 2.8 | Horizontal and vertical wavenumber geometry | 37 |
| 2.9 | $W(x)$ as a function of range | 38 |
| 2.10 | Analytic Vs. OAR solution | 39 |
| 3.1 | Vertical source array configuration in a matched field environment . . | 41 |
| 3.2 | Schematic of matched-field processing procedure | 43 |
| 3.3 | Factors affecting acoustic arrival phases on individual hydrophones . . | 45 |
| 3.4 | MFP ambiguity surface plot matching an ORCA produced measured signal and OAR as the replica field | 47 |
| 3.5 | Ray paths showing convergence errors due to mismatch depths | 49 |
| 3.6 | Mismatch due to horizontal refraction | 50 |

List of Figures

| | | |
|------|---|----|
| 4.1 | Tow track from 1805 hrs to 1930 hrs | 54 |
| 4.2 | MEVA 5 - Vertical line array configuration | 55 |
| 4.3 | Diagram showing all irregular gridded bathymetric points used in database | 58 |
| 1.1 | Sloping bottom acoustics: ray diagram of interaction along a sloping bottom | 6 |
| 1.2 | Effects of boundaries in shallow water propagation | 7 |
| 1.3 | Vancouver Island geographic area | 10 |
| 1.4 | Vertical line array configuration | 11 |
| 1.5 | MEVA 5 - Tracking Run | 13 |
| 4.9 | Spectral amplitude components at source time: T1920 | 68 |
| 2.1 | Plane wave reflection coefficients | 23 |
| 4.10 | Spectral amplitude components at source time: T1922 (doppler shifted) | 69 |
| 2.2 | Range segmentation for adiabatic approximation | 24 |
| 2.3 | Samples of ORCA produced mode functions | 31 |
| 2.4 | Eigenvalue Lookup Table - uncorrected | 32 |
| 2.5 | Eigenvalue Lookup Table - corrected | 33 |
| 2.6 | Highest order mode evaluation | 34 |
| 2.7 | ASA Benchmark comparison | 36 |
| 2.8 | Horizontal and vertical wavenumber geometry | 37 |
| 2.9 | $W(x)$ as a function of range | 38 |
| 2.10 | Analytic Vs. OAR solution | 39 |
| 5.9 | Estimated horizontal refracted rays | 80 |
| 3.1 | Vertical source array configuration in a matched field environment | 41 |
| 3.2 | Schematic of matched-field processing procedure | 43 |
| 3.3 | Factors affecting acoustic arrival phases on individual hydrophones | 45 |
| 3.4 | MFP ambiguity surface plot matching an ORCA produced measured signal and OAR as the replica field | 47 |
| 5.14 | Search results range depth at 1900 hrs (360°) | 82 |
| 3.5 | Ray paths showing convergence errors due to mismatch depths | 49 |
| 5.15 | Search results range depth at 1910 hrs (360°) | 83 |
| 3.6 | Mismatch due to horizontal refraction | 50 |
| 5.16 | Geographic track showing matched field correlator results | 84 |

| | | |
|------|--|----|
| 4.1 | Tow track from 1805 hrs to 1930 hrs | 54 |
| 4.2 | MEVA 5 - Vertical line array configuration | 55 |
| 4.3 | Diagram showing all irregular gridded bathymetric points used in database | 90 |
| 5.20 | for MEVA 5 experiment region | 58 |
| 4.4 | Final MEVA 5 bathymetric contour chart | 59 |
| 4.5 | Diurnal variability of temperature: SVP #25, 26, 27 | 63 |
| 4.6 | Diurnal variability of temperature: SVP #27, 28, 29 | 64 |
| 4.7 | MEVA 5 array drift | 66 |
| 4.8 | Shelf & slope currents | 67 |
| 4.9 | Spectral amplitude components at source time: T1920 | 68 |
| 4.10 | Spectral amplitude components at source time: T1822 (doppler shifted) | 69 |
| 5.1 | Target track with selected radials of interest | 71 |
| 5.2 | OAR-produced acoustic propagation field along T1851 Radial | 72 |
| 5.3 | Lloyd's Mirror sound pattern | 73 |
| 5.4 | Ambiguity surface at 1819 hrs | 75 |
| 5.5 | Ambiguity surface at 1840 hrs | 76 |
| 5.6 | Ambiguity surface at 1900 hrs | 76 |
| 5.7 | MFP at 1920 hrs | 77 |
| 5.8 | Multi-plot at 1920 hrs | 79 |
| 5.9 | Estimated horizontal refracted rays | 80 |
| 5.10 | Search results (<i>range, depth, & bearing</i>) at 1840 hrs | 82 |
| 5.11 | Search results (<i>range, depth, & bearing</i>) at 1900 hrs | 82 |
| 5.12 | Search results (<i>range, depth, & bearing</i>) at 1910 hrs | 83 |
| 5.13 | Search results (<i>range, depth, & bearing</i>) at 1920 hrs | 83 |
| 5.14 | Search results (<i>range, depth, & bearing</i>) at 1900 hrs (360°) | 84 |
| 5.15 | Search results (<i>range, depth, & bearing</i>) at 1910 hrs (360°) | 84 |
| 5.16 | Geographic tracking from highest <i>Bartlett correlator</i> results | 87 |

| | |
|--|----|
| 5.17 Tracking from highest <i>Bartlett correlator</i> showing discrepancies | 88 |
| 5.18 Geographic tracking from best <i>depth and bearing</i> results | 89 |
| 5.19 Geographic tracking from peak-Bartlett results with known bearing | 90 |
| 5.20 Peak-Bartlett fluctuation as a function of time | 91 |
| 5.21 Highest Bartlett correlation along the true bearing plotted as Range Vs Time | 92 |

would also like to thank Dr. Stan Dosso for his meticulous attention to detail, dissecting this document to ensure viability. I wish to acknowledge the the outstanding help from Dr. Ron Kessel and Dr. Oleg Godin for their insightful guidance in acoustic theory and for their avid interest in this project, and to Dr. Mike Wilmut for the many hours of helpful discussions on MF tracking.

I wish to thank my DND sponsor, Mr. Doug Bancroft who in many more ways than one ensured that I was successful with this endeavour. To Lt(N) Alex Grant for providing many words and deeds of encouragement and friendship during darker academic times. Also to Dr. Warren Wolfe and Dr. David Krauel who took a risk with their initial support and encouragement (remembering earlier precarious days). To my good friends at SEOS, Mark, Nicole, Fabian, Simon and of course, to Lothar Jaschke. Thanks also to my very good friend, John Manning.

Several years back, I had the good fortune of serving aboard HMCS Annapolis, under the command of Commander Rick R. Town. As an underwater warfare director, I had the privilege of learning the art of submarine hunting which evoked my interest, along with Cdr Town's strong support, to further my knowledge of ocean acoustics. With the completion of this document, in turn I wish to thank him.

Finally, it has been a long road for my wife, Sherry. I wish to dedicate this thesis to her.

Acknowledgements

A number of people have extended themselves in such a way that it made the start and completion of this thesis possible. First and foremost I wish to thank my supervisor Dr. Ross Chapman for his support, guidance and enormous patience. I would also like to thank Dr. Stan Dosso for his meticulous attention to detail, dissecting this document to ensure viability. I wish to acknowledge the the outstanding help from Dr. Ron Kessel and Dr. Oleg Godin for their insightful guidance in acoustic theory and for their avid interest in this project, and to Dr. Mike Wilmut for the many hours of helpful discussions on MF tracking.

I wish to thank my DND sponsor, Mr. Doug Bancroft who in many more ways than one ensured that I was successful with this endeavour. To Lt(N) Alex Grant for providing many words and deeds of encouragement and friendship during darker academic times. Also to Dr. Warren Wolfe and Dr. David Krauel who took a risk with their initial support and encouragement (remembering earlier precarious days). To my good friends at SEOS, Mark, Nicole, Fabian, Simon and of course, to Lothar Jaschke. Thanks also to my very good friend, John Manning.

Several years back, I had the good fortune of serving aboard HMCS Annapolis, under the command of Commander Rick R. Town. As an underwater warfare director, I had the privilege of learning the art of submarine hunting which evoked my interest, along with Cdr Town's strong support, to further my knowledge of ocean acoustics. With the completion of this document, in turn I wish to thank him.

Finally, it has been a long road for my wife, Sherry. I wish to dedicate this thesis to her.

Chapter 1

The Transparent Ocean

"The threat is stronger than its execution ...

a submarine's covert nature is its greatest strength"

- Keynote speaker

Subcommittee on Non-Atomic Military Research and Development

Subgroup G - Symposium on Shallow Water Undersea Warfare

21 October 1996

1.1 Historical

The remarkable advances in ocean acoustics can largely be attributed to research, developments and progress made within the last half century. Notably, the advent of the submarine significantly propelled the desires and needs to understand the acoustic nature of the world's oceans. Notwithstanding the above, the relative ease that underwater sound can be applied to a variety of purposes allowed scientists to expand these requirements to a wide range of research and explorations (Urick 1975).

Since the end of World War II, literature on underwater acoustics and its scientific applications have grown to great proportions. As a result, sonar systems and acoustic devices have been developed, perpetually improved and used to suit the many growing needs of humans as we race to acquire a greater understanding of the planet's oceans. Interestingly, *passive* acoustics has its origins as far back as 1490 when Leonardo da Vinci, an archetypal engineer, wrote (Bell 1962):

“If you cause your ship to stop, and place the head of a long tube in the water and place the other extremity to your ear, you will hear ships at a great distance from you.”

The Leonardo air tube used for passive listening was improved around the time of World War I. At about the same time *active* sound ranging was employed to meet the German U-boat threat in a highly secretive set of experiments conducted by a group of physicists who coined the term *asdic* (Hadley 1985)¹ for the *active* echo-ranging sonar systems. The passive system (MV device) consisted of a pair of line arrays of 12 air tubes each, mounted along the bottom of a ship (Urlick 1975) on the port and starboard sides, respectively. With surprising precision the bearing of a noisy target was observed to within $\frac{1}{2}^\circ$. Another insightful development of that time was a neutrally buoyant flexible line array called the *eel* (Urlick 1975) which could be easily fitted to any ship and towed astern and away from the noisy vessel on which it was mounted. Collectively, these devices culminated in methods of target acquisition that allowed some measure of success in the detection of underwater targets, be it experimental or hostile.

The postwar developments saw further advances in the exploitation of underwater sound, particularly with advances in electronics that allowed new domains of amplification, processing and displaying sonar information to an observer. At that time, the most important milestone of underwater acoustic research was the greater understanding of the many aberrations of sound propagation at sea. For example, the seawater medium greatly affected the nature of the sound path and transmission characteristics. Diurnal heating causing poorer sonar performance (known as *the afternoon effect*) also was noticed (Jensen *et al.* 1994). Other characteristics such as

¹According to M.L. Hadley, *ASDIC* is an acronym for the Allied Submarine Detection Investigation Committee, established in 1918. The system was used for underwater sound detection for submerged submarines. A similar system later developed by the U.S. Navy was called SONAR (Sound Navigation and Ranging), a term exclusively used today in all NATO navies. In ideal conditions, *asdic* ranges lay between 1200 and 1500 yards. *Asdic* was also employed in passive mode by listening to sounds in the water, such as engine noise and propeller wash.

mixed layers and *surface duct* regions, deep sound channels, refraction of sound deep into the depths, "shadow zones", attenuation, absorption and reverberations effects of shallow water; all needed to be accounted for to effectively employ *active* and *passive* sensors. Subsequently, there is little of our current knowledge of underwater acoustics that cannot be traced back to those earlier discoveries of these two war-time periods of the 20th century.

As *tactical* and *strategic* considerations shifted over the past 50 years, the response to any perceived threat has culminated in an equal shift of acoustic requirements. Sensors continued to become more sophisticated as the submarine targets became more difficult to locate and track. Passive sonar arrays containing many hydrophones have been deployed in various locations on deep ocean floors as surveillance platforms to meet the quieter submarine lurking in the ocean's depths. The emergence of faster and more efficient digital computer systems, complex signal processing along with sophisticated hydrophone systems have allowed scientists to exploit even further the ocean environment in ways which five decades ago would have been deemed improbable (Urick 1975).

By the early 1990s, the end of the cold war perpetuated a great proliferation of quiet non-nuclear submarines to third world nations. International peacekeeping suddenly emerged as a growing industry for many NATO countries in regions of political and social conflicts. Many, if not most, of these regions are situated along coastal, shallow water continental slopes. To meet this new threat environment, the impetus in passive acoustics has focused on advanced beamforming techniques such as *adaptive beam-forming* and *matched-field processing*. The noisy coastal acoustic environment dictates that these signal processing methods should be used if passive sensors are to provide useful operational capability against the quiet modern diesel-electric submarine (Goldsberry 1996).

1.2 Shallow Water Environmental Factors

The radiated noise signals from ships and submarines can be collected, for passive detection, by a hydrophone array either horizontally towed by another vessel or vertically moored to the bottom. The effects of shallow water on the detection ability of a source (or target) are significantly different than those observed in deeper oceanic regions. In these littoral regions, the sound speed profile, the ocean surface, water depth and bottom properties are all important, are spatially varying and the parameters are generally not known in sufficient detail and with enough accuracy to permit long-range predictions in a satisfactory way (Jensen *et al.* 1994).

Propagation studies generally involve experimental measurements at sea which, when compared with numerical models that solve the wave equation or some approximation to it (Dosso 1982), provide the means to predict geoacoustic or oceanic properties or to enable an observer to track a submerged target. The numerical approximation can reliably define the position of the target within a reasonable parentheses of error if this comparison is "matched" with the measured data. It then becomes imperative that the numerical model be as realistic as possible to reflect the true nature of the acoustic environment.

Early propagation studies were *range-independent*, where sound speed alone was taken to depend only upon its vertical configuration. This yielded a two-dimensional (2-D) problem. When the sound speed varied in range and azimuth, the full 3-D character of the Helmholtz equation surfaced as a problem to solve. Most are handled by intermediate solutions ($N \times 2D$, PE, adiabatic normal modes, etc) (Robinson and Lee 1994). In a range-independent case, there are no oceanographic features that cause limitations to the point-to-point propagation. The one-way outgoing solution is the total solution. However, *range-dependent* scenarios present a great variety of problems. Numerically, the solutions to these problems may not represent the true acoustic field. Yet, an approximation of the "true" acoustic field, as dictated by its

environment, in many cases, may lead to reasonable forecasts.

In choosing a model to replicate the true acoustic field, one should consider certain characteristics of the water column that may be dominant variables in a littoral environment. A principle characteristic of shallow-water propagation is the downward refracting sound speed profile. These sound paths have strong interaction with the surface or bottom reflection-refraction combinations. This is typical of continental shelf and sloping bottoms from 200 m to 1000 m of water depth (Jensen *et al.* 1994). It is these bottom interactions that arise as a dominant factor in the modelling algorithms, and subsequently define the propagation paths.

Often the ocean bottom is modelled as a fluid. This means that only one type of wave is supported - a compressional wave. If the sediment is solid or semi-consolidated, the medium is modelled as elastic, supporting both compressional and shear waves. To add to this, the media are *viscoelastic*, meaning that the sediments are lossy. According to Jensen *et al.* (1994) and Hamilton (1980), bottom materials are three to four orders of magnitude more lossy than seawater. For example, the attenuation of sound at 100 Hz in seawater is approximately 0.004 dB/km, whereas the compressional wave attenuation in bottom materials varies between 2 dB/km in basalt to 63 dB/km in silt. The error in a model is compounded if the properties of the bottom layers are not known or are incorrect. Generally, the information required for a complete geoaoustic model should include (note Fig. 1.1): bathymetry, compressional wave speed C_p , shear wave speed C_s , compressional wave attenuation α_p , shear wave attenuation α_s and density ρ . In addition, information is required on the variation of all these parameters with geographical position.

the slope angle.

This enhancement is usually best understood in terms of ray theory. As the

²The continental shelf extends from the shore seaward to an average width of 65 km and an average depth of 165 m. The continental slope is the steep gradient section of the ocean floor that vertically extends from the shelf to the deep sea bottom averaging about 4000 m. (Pickard and Emery 1990)

1.2.1 Continental Slope

The propagation along a continental slope² is strongly influenced by the variation in ocean depth and range. Acoustic rays, defined as normals to the propagating wavefronts, traverse the slope by a series of bottom and surface reflections. At each bottom reflection the grazing angle of the ray is increased or decreased by twice the sloping angle. In the case of upslope propagation, as shown in Figure 1.1, the

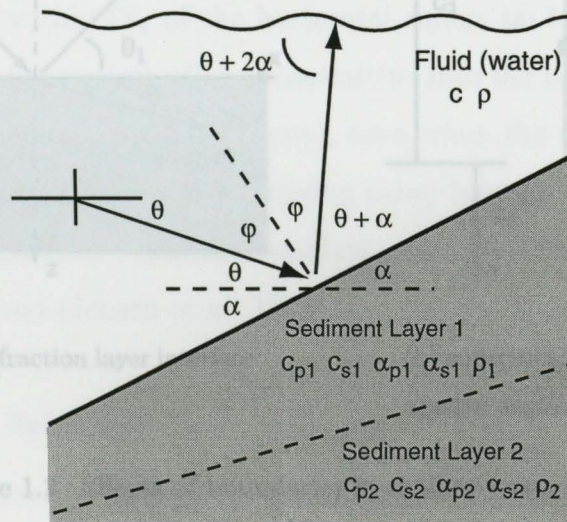


Figure 1.1 Propagation of an acoustic ray path when interacting with an upsloping bottom.

In addition, Figure 1.2(a) depicts reflection and refraction at an interface. The sediment interface (or a sediment-sediment interface) becomes an important measure angle becomes steeper with each bottom reflection (Dosso 1982). As the grazing angle increases, the loss due to transmission into the sediments increases. Eventually, the acoustic wave propagates entirely into the sediments. Conversely, in downslope acoustic propagation, the grazing angle at each bottom reflection reduces by twice the slope angle.

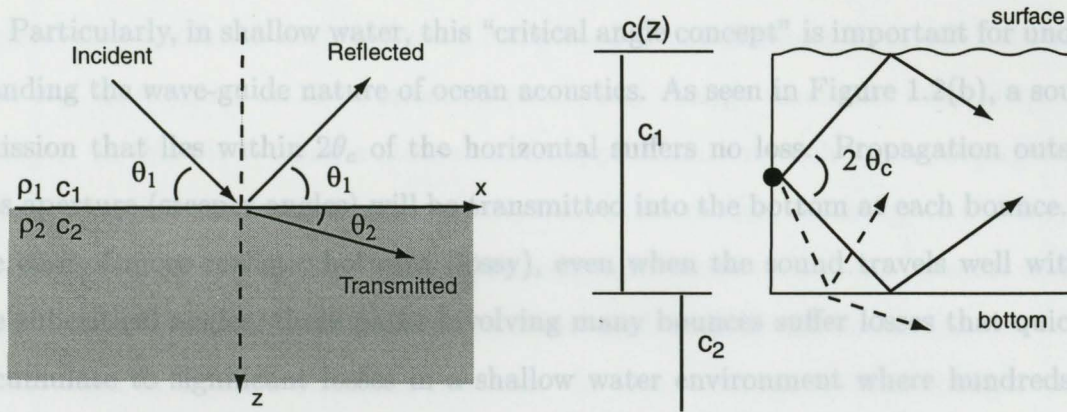
This enhancement is usually best understood in terms of ray theory. As the

²The *continental shelf* extends from the shore seaward to an average width of 65 km and an average depth of 165 m. The *continental slope* is the steep gradient section of the ocean floor that vertically extends from the shelf to the deep sea bottom averaging about 4000 m. (Pickard and Emery 1990)

wave continues to traverse downslope, the steep angle bottom interacting paths are consequently converted into shallow angle paths that propagate with low loss. The ray becomes continuously refracted. Such effects are demonstrated in Chapman *et al.* (1987).

fect reflection is found when the incident angle at a boundary is smaller than the critical grazing angle.

Particularly, in shallow water, this "critical angle concept" is important for understanding the wave-guide nature of ocean acoustics. As seen in Figure 1.2(b), a sound emission that is within 20% of the horizontal suffers no loss of propagation outside this shallow water environment (Jensen *et al.* 1994).



(a) reflection-refraction layer interface

(b) subcritical and supercritical propagation angles

1.2.2 Horizontal Refraction

In a range-dependent environment, the ray paths are observed to "bend" or refract as they propagate through regions on a sloping bottom.

In addition, Figure 1.2(a) depicts reflection and refraction at an interface. The ratio of the amplitude of a reflected plane wave to a plane wave incident to the water-sediment interface (or a sediment-sediment interface) becomes an important measure of the effect of the bottom on sound propagation. Jensen *et al.* (1994) discussed these bottom loss mechanisms which yield an important expression, *Snell's law of refraction*,

Horizontal ray theory for ocean acoustics is a phenomena where the ray paths are

$$k_1 \cos \theta_1 = k_2 \cos \theta_2, \quad (1.1)$$

This is often neglected in range-dependent modelling, the most prevalent reason being

the enormous computer time required to calculate an acoustic field in 3-D. As a

shortcut, combining the results along supersector bearings allows one to build a 3-D

$$\theta_c = \arccos\left(\frac{c_1}{c_2}\right) \quad (1.2)$$

This denotes that the grazing angle(s), Equation (1.2), of a ray at the layer boundaries are related to the sound speeds c_1 and c_2 of the layers. From Snell's law, the critical angle only exists when the sound speed of the second medium is higher than the first layer. Perfect reflection is found when the incident angle at a boundary is smaller than the *critical grazing angle*.

Particularly, in shallow water, this "critical angle concept" is important for understanding the wave-guide nature of ocean acoustics. As seen in Figure 1.2(b), a sound emission that lies within $2\theta_c$ of the horizontal suffers no loss. Propagation outside this aperture (steeper angles) will be transmitted into the bottom at each bounce. In the case of more realistic bottoms (lossy), even when the sound travels well within the subcritical angles, these paths involving many bounces suffer losses that quickly accumulate to significant losses in a shallow water environment where hundreds of bounces are observed (Jensen *et al.* 1994).

1.2.2 Horizontal Refraction

In a range dependent waveguide, the problem of modelling correctly the environment is a much more difficult problem than seen when applying theory in a 2-D view point. In a "real" system, the variability is also observed azimuthally, or out of the vertical plane. The problem was stated by Pierce (1965): "... if the measured direction of propagation of a normal-mode wave detected at a point is different from the direction from the source to the receiver, the explanation may be given in the context of horizontal ray paths."

Horizontal ray theory for ocean acoustics is a phenomena where the ray paths are observed to "bend" or refract away from the shallower regions on a sloping bottom. This is often neglected in range-dependent modelling, the most prevalent reason being the enormous computer time required to calculate an acoustic field in 3-D. As a shortcut, combining the results along numerous bearings allows one to build a 3-D

image (Jensen *et al.* 1994), or more appropriately an $N \times 2$ -D acoustic field. However, the true nature of horizontal refraction is not properly included; thus the observed direction measurement does not 'match' the calculated direction that would be used in the matched-field processor.

In Brekhovskikh and Godin's (1992) account of horizontal ray theory, they explained that a solution derived from a complete 3-D coordinate system will determine that ray trajectories on the horizontal plane may change when the wave frequency changes. In this view, using a normal mode approximation, each mode propagates in a slowly varying waveguide *independently* from other modes, adjusting to the varying conditions in the waveguide. This adjustment near shore conditions (coastal wedge) allow calculations of horizontal rays that are analogous to the determination of ordinary rays in a plane stratified medium. In ideal settings, with a straight shore line and sufficient perturbation area, a turning point in a ray (refraction) may result in a *caustic of horizontal rays* (Brekhovskikh and Godin 1992) and a well defined refraction.

1.3 Pacific Shelf Experiment

In September 1993, a series of acoustic experiments were carried out at the edge of the continental shelf off the west coast of Vancouver Island, B.C. in the North-East Pacific Ocean (Figure 1.3). This experiment is referred to as the *Ocean Acoustics Sea Trial Pacific Shelf* and was conducted by scientists from the Canadian Department of National Defence - Defence Research Establishment Pacific (DREP). The experiment covered nine experiments with the Canadian Ocean Acoustic Measurement System (COAMS) horizontal array and ten experiments with a Multi-Element Vertical Array (MEVA). The analysis of this document pertains to an acoustic trial run (MEVA 5) that started at 1805 hrs on the 15 Sept 1993 and was completed by 2200 hrs of the

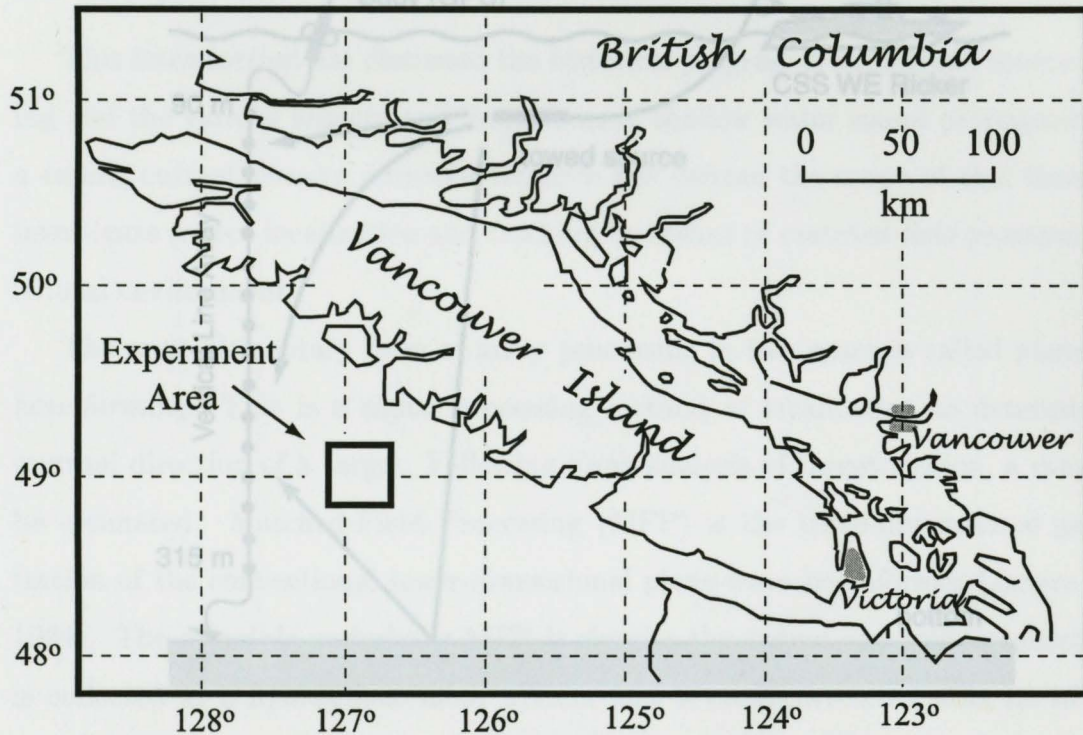


Figure 1.3 Geographic location of the Pacific Shelf Sea Trials 25-30 nm off the west coast of Vancouver Island

Several conditions were unintentionally imposed upon the experiment; during an earlier storm, the moorage line broke causing the VLA to drift freely in tidal currents off the coast. Although the VLA was fitted with a GPS (Global Positioning System) receiver, the error in source position is uncertain as the drift denoted the buoy position and not the entire array. Second, the source depth was not monitored due to a malfunction of the source depth monitoring system. Third, the source depth is assigned an error of 80-100 m. GPS differential corrections were not available for non-military purposes. Notwithstanding, the experiment was conducted under very realistic set of conditions.

Two ships participated in the sea trial. CFAV ENDEAVOUR monitored the receiver, a 16-element vertical array (VLA) that was suspended from a surface float in water depths of 380-400 m. The other vessel, CSS W.E. RICKER, towed a CW sound source at a recorded speed of 4-6 knots. The array and source configuration is shown in Figure 1.4. The downslope progression of the source vessel began in water of approximately 370 m depth and progressed to deeper water, 700 m to 750 m. The track subsequently followed two arcs, one arcing upslope 5-6 km from the receiver and the second arcing downslope 10-11 km from the receiver (Figure 1.5). Two strong tonals were emitted from the sound projector at 45 and 70 Hz. A weaker line at 72 Hz with a 20 dB lower source level was also transmitted.

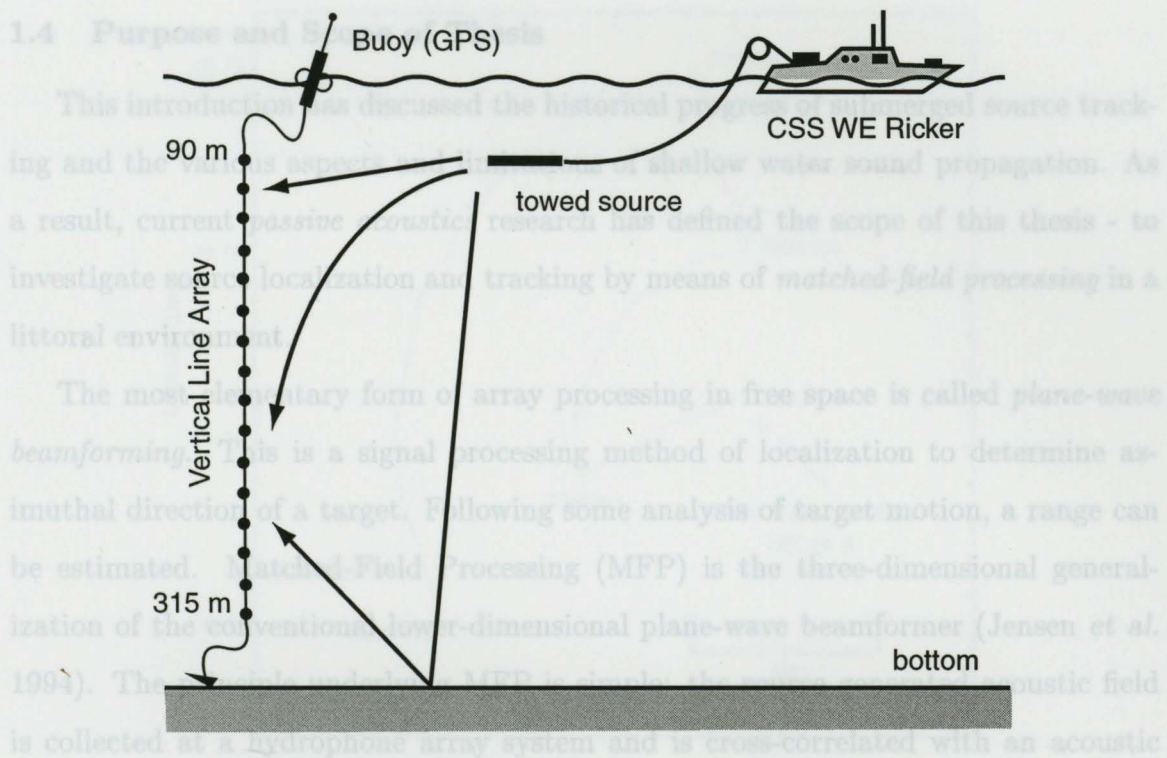


Figure 1.4 Vertical line array configuration

Several limitations were unintentionally imposed upon the experiment; during an earlier storm, the moorage line broke causing the VLA to drift freely in tidal currents off the coast. Although the VLA was fitted with a GPS (Global Positioning System) receiver, the error in source position is uncertain as the drift denoted the buoy position and not the entire array. Second, the source depth was also unknown due to a malfunction of the source depth monitoring system. Third, the GPS range estimates are assigned an error of 80-100 m. GPS differential settings were not yet available for non-military public use. Notwithstanding these limitations, the experiment offered a very realistic set of conditions.

The characteristics of the continental slope also offered a means to break the symmetry of the acoustic propagation to allow accurate observations of range, depth

1.4 Purpose and Scope of Thesis

This introduction has discussed the historical progress of submerged source tracking and the various aspects and limitations of shallow water sound propagation. As a result, current *passive acoustics* research has defined the scope of this thesis - to investigate source localization and tracking by means of *matched-field processing* in a littoral environment.

The most elementary form of array processing in free space is called *plane-wave beamforming*. This is a signal processing method of localization to determine azimuthal direction of a target. Following some analysis of target motion, a range can be estimated. Matched-Field Processing (MFP) is the three-dimensional generalization of the conventional lower-dimensional plane-wave beamformer (Jensen *et al.* 1994). The principle underlying MFP is simple: the source generated acoustic field is collected at a hydrophone array system and is cross-correlated with an acoustic replica-field computed, for a variety of trial source locations, by means of an appropriate propagation model. The highest correlation value corresponds to a localization (Tolstoy 1993). An observer can determine the target's location in *range*, *depth* and *bearing* - even course and speed if needed.

This thesis will describe such a process. As seen in Figure 1.5, the target was towed along a two-arc track producing a signal. The signal is matched to a modelled acoustic field replicated using a normal mode propagation model for multi-layered acousto-elastic ocean environments called ORCA, developed by Evan K. Westwood (1996). The calculated output of ORCA were used to build an *adiabatic normal mode* model which was named OAR (ORCA Adiabatic Replica). The OAR model simulated the varying environment of a continental slope, including the spatially varying elastic bottom.

The characteristics of the continental slope also offered a means to break the symmetry of the acoustic propagation to allow accurate observations of *range*, *depth*

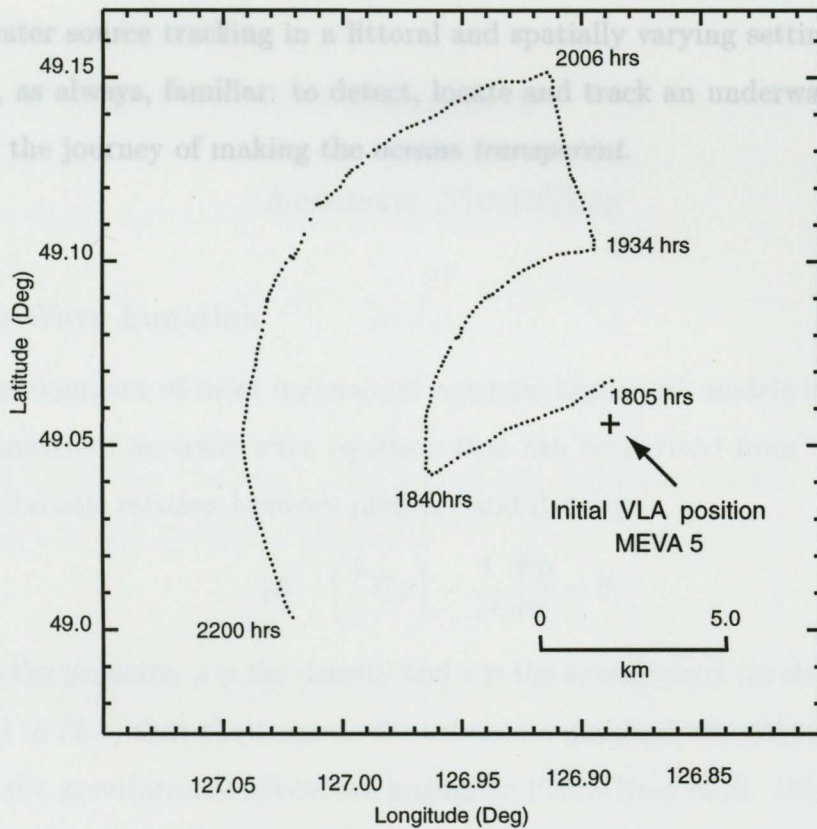


Figure 1.5 The display shows the source track towed by CSS W.E. RICKER. Each point represents the GPS navigation position at every minute. The cross indicates where the VLA was located at the beginning of the experiment as it continued to drift with the currents

and *bearing* of the target while it continuously altered course direction. The MFP model allows a broad search of an area of interest, analogous to a “radar sweep”, to detect and track the underwater source. Aspects of horizontal refraction are discussed in section 1.2.2 showing evidence of out of plane (3-D) propagation presented in “mismatch” observations of the MFP algorithms.

To date, a great deal of material has been published about MFP, yet little has been compiled and correlated to draw conclusions based on “real-time” and “real-measured-data”. The goal of this thesis is to do just that and to gain a greater understanding

of underwater source tracking in a littoral and spatially varying setting. Finally the pursuit is, as always, familiar: to detect, locate and track an underwater target and to further the journey of making the oceans *transparent*.

Acoustic Modelling

2.1 The Wave Equation

The development of most underwater acoustic numerical models begins with the classical linearized acoustic wave equation that can be derived from hydrodynamics and the adiabatic relation between pressure and density:

$$\rho \nabla \cdot \left(\frac{1}{\rho} \nabla p \right) - \frac{1}{c^2} \frac{\partial^2 p}{\partial t^2} = 0, \quad (2.1)$$

where p is the pressure, ρ is the density and c is the sound speed (in an ideal fluid). It is assumed in (2.1) that the acoustic disturbance is propagated without transporting mass and the gravitational effects are negligible (Chiu-Bing *et al.* 1994).

Following the development detailed in Jensen *et al.* (1994) and Frisk (1994), in an ideal fluid, the assumption is made that density is constant in space. This results in the wave equation in standard form,

$$\nabla^2 p - \frac{1}{c^2} \frac{\partial^2 p}{\partial t^2} = 0. \quad (2.2)$$

In an ocean environment, underwater sound is produced by a forcing mechanism, be it natural or artificial. A forcing expression can easily be introduced that when applied to (2.2) the following *inhomogeneous wave equation* is produced (Frisk 1994)

$$\nabla^2 p(\mathbf{r}, t) - \frac{1}{c^2(\mathbf{r})} \frac{\partial^2 p(\mathbf{r}, t)}{\partial t^2} = f(\mathbf{r}, t), \quad (2.3)$$

where $f(\mathbf{r}, t)$ is the forced volume energy as a function of space and time.¹

¹The forced point source is defined as vibrating in space and time at $\mathbf{r} = \mathbf{r}_0$. The point source can be represented by the Dirac delta function $\delta(\mathbf{r} - \mathbf{r}_0)$. The delta function has the following properties: $\delta(\mathbf{r} - \mathbf{r}_0) = 0$ for $\mathbf{r} \neq \mathbf{r}_0$; $\int \delta(\mathbf{r} - \mathbf{r}_0) dV = 1$; and $\int g(\mathbf{r})\delta(\mathbf{r} - \mathbf{r}_0) dV = g(\mathbf{r}_0)$. Note dV is the volume element. The representation of the Dirac delta function will be used in the following expressions to denote the forced point source.

2.1.1 Helmholtz Equation

Chapter 2

Acoustic Modelling

2.1 The Wave Equation

The development of most underwater acoustic numerical models begins with the classical linearized acoustic wave equation that can be derived from hydrodynamics and the adiabatic relation between pressure and density:

$$\rho \nabla \cdot \left(\frac{1}{\rho} \nabla p \right) - \frac{1}{c^2} \frac{\partial^2 p}{\partial t^2} = 0, \quad (2.1)$$

where p is the pressure, ρ is the density and c is the sound speed (in an ideal fluid). It is assumed in (2.1) that the acoustic disturbance is propagated without transporting mass and the gravitational effects are negligible (Chin-Bing *et al.* 1994).

Following the development detailed in Jensen *et al.* (1994) and Frisk (1994), in an ideal fluid, the assumption is made that density is constant in space. This results in the wave equation in standard form,

$$\nabla^2 p - \frac{1}{c^2} \frac{\partial^2 p}{\partial t^2} = 0. \quad (2.2)$$

In an ocean environment, underwater sound is produced by a forcing mechanism, be it natural or artificial. A forcing expression can easily be introduced that when applied to (2.2) the following *inhomogeneous wave equation* is produced (Frisk 1994)

$$\nabla^2 p(\mathbf{r}, t) - \frac{1}{c^2(\mathbf{r})} \frac{\partial^2 p(\mathbf{r}, t)}{\partial t^2} = f(\mathbf{r}, t), \quad (2.3)$$

where $f(\mathbf{r}, t)$ is the forced volume energy as a function of space and time.¹

¹The forced point source is defined as vibrating in space and time at $\mathbf{r} = \mathbf{r}_0$. The point source can be represented by the *Dirac delta function* $\delta(\mathbf{r} - \mathbf{r}_0)$. The delta function has the following properties: $\delta(\mathbf{r} - \mathbf{r}_0) = 0$ for $\mathbf{r} \neq \mathbf{r}_0$; $\int \delta(\mathbf{r} - \mathbf{r}_0) dV = 1$; and $\int g(\mathbf{r}) \delta(\mathbf{r} - \mathbf{r}_0) dV = g(\mathbf{r}_0)$. Note dV is the volume element. The representation of the *Dirac delta function* will be used in the following expressions to denote the forced point source.

2.1.1 Helmholtz Equation

The coefficients of the differential operators in (2.3) are independent of time. To shift the expression to a frequency-domain wave equation, the reduction can be achieved by using frequency-time Fourier transforms,

$$f'(t) = \frac{1}{2\pi} \int_{-\infty}^{\infty} f(\omega) e^{i\omega t} d\omega, \quad (2.4)$$

$$f(\omega) = \int_{-\infty}^{\infty} f'(t) e^{-i\omega t} dt. \quad (2.5)$$

The above Equations (2.4) and (2.5) lead to the frequency domain wave equation, better known as the *Helmholtz equation*,

$$[\nabla^2 + k^2(\mathbf{r})] p(\mathbf{r}, \omega) = f(\mathbf{r}, \omega), \quad (2.6)$$

where $\omega = 2\pi f$ and $k(\mathbf{r})$ is the wavenumber at radial frequency ω ,

$$k(\mathbf{r}) = \frac{\omega}{c(\mathbf{r})}. \quad (2.7)$$

Introducing the *Dirac delta function* to (2.6) produces the *inhomogeneous Helmholtz equation*:²

$$[\nabla^2 + k^2(\mathbf{r})] p(\mathbf{r}) = -4\pi\delta(\mathbf{r} - \mathbf{r}_0). \quad (2.8)$$

Equation (2.8) now forms the basis to which the theoretical numerical method describing normal modes will take place.

2.2 The Method of Normal Modes

Cylindrical symmetry of the propagating sound wave within a shallow water waveguide is usually assumed in ocean acoustics. In the case where 3-D effects are

²The introduction of a forcing term cited in Frisk (1994) shows a source representing a volume injection amplitude necessary to produce a pressure amplitude of 1 Pa at 1m distance from the source, at radial frequency ω . As a result, the point source reflects a spherical surface area denoted as $-4\pi\delta(\mathbf{r} - \mathbf{r}_0)$. This is the convention used in this development. In Jensen *et al.* (1994) the forcing term used is one of a point source with no spherical surface area.

not important (*i.e.* horizontal refraction) cylindrical symmetry is a good simplifying assumption in a single look direction. For a *cylindrical coordinate system* $\mathbf{r} = (r, \varphi, z)$ the source coincides with the z -axis, $\mathbf{r}_0 = (0, 0, z_0)$, and the Laplacian operator for the Helmholtz equation satisfies the following,

$$\nabla^2 = \frac{1}{r} \frac{\partial}{\partial r} r \frac{\partial}{\partial r} + \frac{1}{r^2} \frac{\partial^2}{\partial \varphi^2} + \frac{\partial^2}{\partial z^2}. \quad (2.9)$$

The Helmholtz equation (2.8) in cylindrical coordinates reduces to two-dimensions that varies with r , sound speed $c(z)$ and density $\rho(z)$ ³

$$\frac{1}{r} \frac{\partial}{\partial r} \left(r \frac{\partial p}{\partial r} \right) + \rho(z) \frac{\partial}{\partial z} \left(\frac{1}{\rho(z)} \frac{\partial p}{\partial z} \right) + \frac{\omega^2}{c^2(z)} p = -4\pi \frac{\delta(r)}{r} \delta(\varphi) \delta(z - z_s) \quad (2.10)$$

For cylindrical symmetry (*i.e.* no dependence on φ), the right hand side of (2.10) when integrated by $\int_0^{2\pi} d\varphi$ will equal $-4\pi \frac{\delta(r)}{r} \delta(z - z_s)$. Equation (2.10) reduces to

$$\frac{1}{r} \frac{\partial}{\partial r} \left(r \frac{\partial p}{\partial r} \right) + \rho(z) \frac{\partial}{\partial z} \left(\frac{1}{\rho(z)} \frac{\partial p}{\partial z} \right) + \frac{\omega^2}{c^2(z)} p = -2 \frac{\delta(r)}{r} \delta(z - z_s). \quad (2.11)$$

Using the method of *separation of variables*, a solution is obtained for the “unforced” general *Helmholtz equation*. The form $p(r, z) = \Phi(r)\Psi(z)$ will be substituted into (2.10) to obtain⁴

$$\frac{1}{\Phi} \left[\frac{1}{r} \frac{d}{dr} \left(r \frac{d\Phi}{dr} \right) \right] + \frac{1}{\Psi} \left[\rho(z) \frac{d}{dz} \left(\frac{1}{\rho(z)} \frac{d\Psi}{dz} \right) + \frac{\omega^2}{c^2(z)} \Psi \right] = 0. \quad (2.12)$$

This equation (2.12) can only hold true if both terms in the square brackets equal a *separation constant*, $-k_{rm}^2$.

The important contribution of this solution to the Helmholtz equation is the following development of the *modal equation* which is obtained from the term in the

³The source is expanded to this form from a transformation from Cartesian coordinates to cylindrical coordinates by means of a Jacobean matrix which, for brevity, will not be shown here: $(\delta(r - r_s) = \delta(x - x_s)\delta(y - y_s)\delta(z - z_s))$.

⁴If ρ and c depended on r then (2.11) is *not* separable.

second square bracket from (2.12),

$$\rho(z) \frac{d}{dz} \left[\frac{1}{\rho(z)} \frac{d\Psi(z)}{dz} \right] + \left[\frac{\omega^2}{c^2(z)} - k_{rm}^2 \right] \Psi_m(z) = 0 \quad (2.13)$$

with boundary conditions ⁵

$$\Psi(0) = 0, \quad \left. \frac{d\Psi}{dz} \right|_{z=h} = 0. \quad (2.14)$$

The modal equation (2.13) is known as a *Sturm-Liouville* eigenvalue problem of the general form

$$\frac{d}{dz} \left[p(z) \frac{dy}{dz} \right] + [s(z) + \lambda w(z)] y = 0. \quad (2.15)$$

The properties of this type of problem are well known and are summarized as they relate to the derived modal equation that pertain to this acoustic solution (Butkov 1968; Jensen *et al.* 1994):

- The modal equation has an infinite number of eigenfunction solutions $\Psi_m(z)$
- The modal *eigenfunctions* are characterized by a *horizontal propagation constant* k_{rm} which equate to *eigenvalues*. The eigenvalues are distinct, real, positive and are ordered as $k_{r1}^2 > k_{r2}^2 > \dots$
- $\Psi_m(z)$ has m zeros on the interval $[0, h]$, where h is the water depth
- The *eigenfunctions* are *orthonormal*.⁶

$$\int_0^h \frac{\Psi_m(z) \Psi_n(z)}{\rho(z)} dz = \begin{cases} 0 & n \neq m \\ 1 & n = m \end{cases} \quad (2.16)$$

⁵The boundary conditions represent a soft and hard boundary, respectively. $P(z=0) = 0$ is a pressure release boundary which is a good representation of the sea surface. This leads to perfect reflection with a 180° phase change. The hard boundary, $\left. \frac{dP(z=h)}{dz} \right| = 0$, leads to perfect reflection with no phase change. Note: h equates to the water depth.

⁶Note that the integral is over the water depth. If there is an extension to the region where $z > h$, then the modes will not be orthogonal unless the integration includes the entire waveguide depth.

- The eigenfunctions $\Psi_m(z)$ are known as normal modes and the acoustic pressure can be represented by an infinite series or a sum of these modes as

$$p(r, z) = \sum_{m=1}^{\infty} \Phi_m(r) \Psi_m(z). \quad (2.17)$$

In ocean acoustics, these modes represent a standing wave pattern defined by the acoustic pressure waves which propagate up and down within the acoustic wave-guide.

Substituting (2.17) into (2.11) will provide

$$\sum_{m=1}^{\infty} \left\{ \frac{1}{r} \frac{d}{dr} \left(r \frac{d\Phi_m(r)}{dr} \right) \Psi_m(z) + \Phi_m(r) \left[\rho(z) \frac{d}{dz} \left(\frac{1}{\rho(z)} \frac{d\Psi_m(z)}{dz} \right) + \frac{\omega^2}{c^2(z)} \Psi_m(z) \right] \right\} = -2 \frac{\delta(r)}{r} \delta(z - z_s). \quad (2.18)$$

Equation (2.13) can simplify the term in the above square brackets, yielding

$$\sum_{m=1}^{\infty} \left\{ \frac{1}{r} \frac{d}{dr} \left(r \frac{d\Phi_m(r)}{dr} \right) \Psi_m(z) + k_{rm}^2 \Phi_m(r) \Psi_m(z) \right\} = -2 \frac{\delta(r)}{r} \delta(z - z_s). \quad (2.19)$$

Now an operator, $\int_0^h (\cdot) \frac{\Psi_n(z)}{\rho(z)} dz$, is applied to (2.19) leading to

$$\sum_{m=1}^{\infty} \left\{ \frac{1}{r} \frac{d}{dr} \left(r \frac{d\Phi_m(r)}{dr} \right) \overbrace{\int_0^h \frac{\Psi_m(z) \Psi_n(z)}{\rho(z)} dz}^{\text{orthogonal}} + k_{rm}^2 \Phi_m(r) \overbrace{\int_0^h \frac{\Psi_m(z) \Psi_n(z)}{\rho(z)} dz}^{\text{orthogonal}} \right\} = -2 \frac{\delta(r)}{r} \int_0^h \frac{\delta(z - z_s) \Psi_n(z)}{\rho(z)} dz. \quad (2.20)$$

From this step in the process, the n th term in the sum survives ($m = n$) and reduces to the form of the Bessel equation,

$$\frac{1}{r} \frac{d}{dr} \left[r \frac{d\Phi_n(r)}{dr} \right] + k_{rn}^2 \Phi_n(r) = -2 \frac{\delta(r)}{r} \frac{\Psi_n(z_s)}{\rho(z_s)}. \quad (2.21)$$

In terms of the Hankel functions, the solution to (2.21) will have the form that relates to the acoustic development herein this thesis (Butkov 1968):

$$\Phi(r) = \begin{cases} H_0^{(1)}(kr) = J_0(kr) + iY_0(kr) \\ H_0^{(2)}(kr) = J_0(kr) - iY_0(kr) \end{cases} \quad (2.22)$$

Therefore, a standard solution to (2.21) becomes

$$\Phi_n(r) = \frac{i\pi}{\rho_s} \Psi_n(z_s) H_0^{(1,2)}(k_{rn}r) \quad (2.23)$$

where $H_0^{(1,2)}$ possess asymptotic diverging and converging complex solutions of cylindrical waves.⁷

$$H_0^{(1)}(kr) \simeq \sqrt{\frac{2}{\pi kr}} e^{i(kr - \frac{\pi}{4})}, \quad (2.24)$$

$$H_0^{(2)}(kr) \simeq \sqrt{\frac{2}{\pi kr}} e^{-i(kr - \frac{\pi}{4})}. \quad (2.25)$$

Finally, the choice of $H_0^{(1)}$ or $H_0^{(2)}$ is connected to the sign convention for the time function $e^{\pm i\omega t}$. In this case, the radiation of the energy emitted by the source is outward as $r \rightarrow \infty$ then (2.17) defined by (2.23) and (2.24) result in

$$p(r, z) = \frac{i\pi}{\rho(z_s)} \sum_{m=1}^{\infty} \Psi_m(z_s) \Psi_m(z) H_0^{(1)}(k_{rm}r) \quad (2.26)$$

or, expanding the asymptotic approximation to the Hankel function,⁸

$$p(r, z) \simeq \frac{\sqrt{2\pi}}{\rho(z_s)} e^{i\pi/4} \sum_{m=1}^{\infty} \Psi_m(z_s) \Psi_m(z) \frac{e^{ik_{rm}r}}{\sqrt{k_{rm}r}}. \quad (2.27)$$

⁷The Hankel function is an accurate far-field approximation ($k_{rn}r \gg 1$) which generally is good several wavelengths away from the source.

⁸Similarly, as defined in Jensen *et al.* (1994), the development of the normal mode complex pressure field may be defined as

$$p(r, z) \simeq \frac{e^{i\pi/4}}{\rho(z_s)\sqrt{8\pi r}} \sum_{m=1}^{\infty} \Psi_m(z_s) \Psi_m(z) \frac{e^{ik_{rm}r}}{\sqrt{k_{rm}r}}$$

which is derived from the initial definition of the forcing term as shown in section (2.1.1).

2.3 Multi-Layered Acousto-Elastic Ocean Environment Modelling

The term *model* in ocean-acoustics has been defined as “computer algorithms and codes that produce numerical results” (Chin-Bing *et al.* 1994). The choice of an appropriate research-level acoustic model will depend on whether the algorithms and codes can calculate and predict acoustic conditions in a manner that is suitable for the researcher. To accomplish the needs of this particular research project, two numerical models were available and were reputed as favourable research-level acoustic models.

2.3.3 ORCA - General Derivation

2.3.1 Parabolic Equation Method - Range-dependent Acoustic Model (RAM)

The first of these models considered was developed by Michael D. Collins (1992, 1993, 1995) called Range-dependent Acoustic Model (RAM). This is a parabolic equation (PE) method for solving range-dependent ocean acoustic problems. It is based on the *split-step Pade solution* (Collins 1993). The range dependence of this method is handled by approximating the medium as a sequence of range-independent regions. The user selects the range grid size to determine an appropriate number of range-independent regions that sufficiently approximates the entire range without compromising accuracy. According to Chin-Bing *et al.* (1994), the ocean variabilities, like those found at this project site, suggest the use of a PE model, such as RAM. Those conditions, which are discussed in Chapter 4, are: ocean sound speed variability, range-dependent interface between ocean and ocean-bottom; sharp discontinuities in sound speed between ocean and ocean-bottom, and computer efficiency of the parabolic approximation. However, RAM only applies to fluid waveguide environments.

2.3.2 Normal Mode Method - Range-independent Acoustic Model (ORCA)

For the shallow water, shelf and slope experimental site the sensitivity of the elastic properties of the bottom was not known. Consequently, it was expected that a

fully elastic model would be required to model the sound propagation. In these environments, the conversion from compressional waves to shear waves and subsequent attenuation of the shear waves represents a significant loss mechanism (Westwood *et al.* 1996). In addition, shear waves and bottom interface modes may dominate the acoustic field. For these reasons, a normal mode model for propagation in acousto-elastic ocean waveguides, ORCA, was selected for use.

2.3.3 ORCA - General Derivation

ORCA was formulated as a general approach that allows for density variations, different from the constant density assumed in an ideal fluid. To do so, the spectral integral representation of the solution is initially taken followed by a calculation of the sum of residues to this integral. In other words, instead of using $p(r, z) = \Phi(r)\Psi(z)$ as an operator to the *separation of variables*, the pressure field can be written as an integral over a range-separated Hankel function $H_0^{(1)}$ and a depth-separated variable function θ :

$$\begin{aligned} p(r, z) &= \int_{-\infty}^0 J_0(k_r r) \theta(z, k_r) k_r dk_r \\ &= \frac{1}{2} \int_{-\infty}^{\infty} H_0^{(1)}(k_r) \theta(z, k_r) k_r dk_r, \end{aligned} \quad (2.28)$$

where the relation between the horizontal wavenumber and the grazing angle of propagation θ for a homogeneous layer is defined as

$$k_r = k_n \cos \theta. \quad (2.29)$$

In the above expression, k_n is the medium wavenumber and corresponds only to real angles ($k_r \leq k_n$). This derivation is well developed in Chap 4 and Sec 5.5 of (Jensen *et al.* 1994), Appendix A (Propagation Equation) Bucker (1970) and Section I (Normal Mode Formulation) (Westwood *et al.* 1996).

¹Prime denotes differential with respect to depth.

As stated in the latter reference, an intermediate result to the above boundary-value problem is given in terms of upward- and downward-looking plane wave reflection coefficients, R_1 and R_2 . The eigenvalue algorithm in ORCA is formulated in terms of the product $R_1 R_2$, as shown in Figure 2.1. Once the mode eigenvalues k_n are found, the compressional mode functions and shear mode functions are solved from the wave equation solutions in each layer.

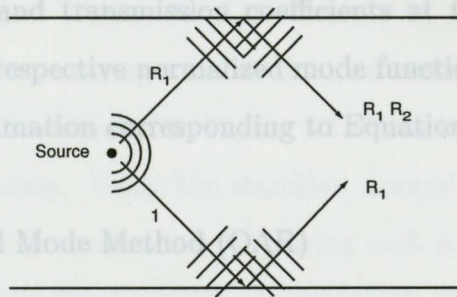


Figure 2.1 Upward-looking and downward-looking plane wave reflection coefficients, R_1 and R_2 .

To summarize the formulation in ORCA, an expression for θ in terms of two functions, $U(z)$ and $V(z)$, are used to satisfy the depth-separated wave equation, similar to the development leading to Equation (2.19). The residue theorem is used to solve the integral (2.28) in terms of normal modes that can be evaluated as follows:

$$p(r, z) = -2\pi i \sum_n \frac{U_n(z)V_n(z_s)k_n H_0^{(1)}(k_n r)}{[\partial W(k, z)/\partial k]_{k=k_n}}, \quad (2.30)$$

where k_n are the mode eigenvalues, defined as the horizontal wavenumbers k for which the Wronskian is evaluated at the source depth (Westwood *et al.* 1996):⁹

$$W(k, z) = U(k, z)V'(k, z) - U'(k, z)V(k, z) \quad (2.31)$$

The depth functions, $U(z)$ and $V(z)$, are expressed in terms of downward- and upward-looking plane wave coefficients and are computed in the process of evaluating

⁹Prime denotes differential with respect to depth.

R_1 and R_2 . Subsequently, the modal eigenvalues corresponding to plane wave angles for which constructive interference occurs between upgoing and down going plane waves are determined. Within the sediment, complex modal eigenvalues (complex k -plane) are computed that account for the loss of energy from the waveguide. These losses are attributed to attenuation in the media, partial reflection/partial transmission at the waveguide boundaries, or shear wave conversion at the boundaries.

From the reflection and transmission coefficients at the layer(s) interfaces the values corresponding to respective normalized mode functions are calculated, leading to the normal mode summation corresponding to Equations (2.26) and (2.27).

2.3.4 Adiabatic Normal Mode Method (OAR)

A significant limitation to the ORCA model is that it is *not* range dependent. In a sloping ocean region, such as the experimental site of this project, ORCA would not provide appropriate and accurate acoustic information. An *adiabatic normal mode* solution was needed to approximate the range-dependency.

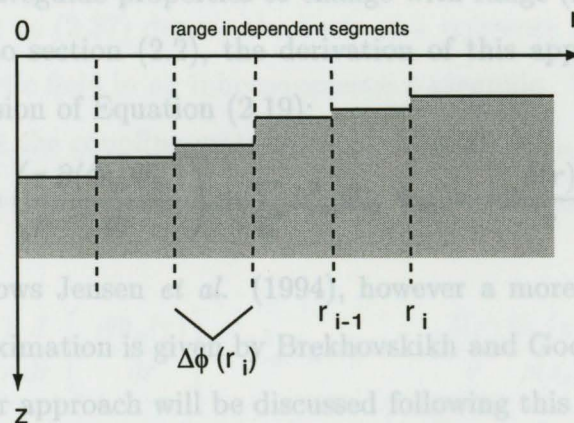


Figure 2.2 Range segmentation for adiabatic approximation. $\Delta\phi(r_i)$ is an equally spaced abscissa of the segmented range between two limits (0 to r).

The *adiabatic* approximation neglects the cross-coupling terms in the modes that

allow energy to transfer from one mode to another. In addition, this approximation requires that the range dependence of the acoustic medium is slowly varying (Chiu and Ehret 1994). Therefore, going from one range to the next the modes do not couple at all, or propagate *adiabatically* as the waveguide varies slowly with range. OAR is such an adiabatic approximation that uses the important multi-layered acoustic information produced by ORCA. IDL¹⁰ algorithms and codes for OAR were developed as part of this thesis project (Appendix A).

The model begins by segmenting a radial along an azimuth into a selected number of smaller range lengths, as depicted in Figure 2.2. Each segment is approximated as a *range independent* solution. Using the standard normal-mode solution, the entire range-dependent scenario is constructed by joining each respective segment. A complete solution would require cross-coupling terms which allow energy from one mode to transfer to other modes of neighboring segments. The adiabatic solution allows modes that are excited at the source to be cut-off and subsequently re-excited as they propagate along the segmented waveguide, depending on local acoustic properties. This also enables waveguide properties to change with range (Frisk 1994).

Referring back to section (2.2), the derivation of this approximation can begin with a modified version of Equation (2.19):

$$\sum_m \frac{\rho}{r} \frac{\partial}{\partial r} \left(\frac{r}{\rho} \frac{\partial(\Phi_m \Psi_m)}{\partial r} \right) + \sum_m k_{rm}^2 \Phi_m \Psi_m = -2 \frac{\delta(r)}{r} \delta(z - z_s). \quad (2.32)$$

This derivation follows Jensen *et al.* (1994), however a more rigorous approach to the adiabatic approximation is given by Brekhovskikh and Godin (1992). Comments relating to the latter approach will be discussed following this development.

Rearranging the terms in (2.32) leads to

$$\sum_m \left[\frac{\rho}{r} \frac{\partial}{\partial r} \left(\frac{r}{\rho} \frac{\partial(\Phi_m)}{\partial r} \right) \Psi_m + 2 \frac{\partial \Phi_m}{\partial r} \frac{\partial \Psi_m}{\partial r} + \frac{\rho}{r} \frac{\partial}{\partial r} \left(\frac{r}{\rho} \frac{\partial \Psi_m}{\partial r} \right) \Phi_m \right]$$

¹⁰IDL is an Interactive Data Language which is an alternative programming language to FORTRAN or MATLAB.

$$+ \sum_m k_{rm}^2 \Phi_m \Psi_m = -2 \frac{\delta(r)}{r} \delta(z - z_s). \quad (2.33)$$

Assuming that ρ is independent of r , by applying a similar operator previously seen in section (2.2), $\int (\cdot) \frac{\Psi_n(r,z)}{\rho(z)} dz$, and using the same *eigenfunction orthogonality* properties, Equation (2.33) will simplify to

$$\frac{1}{r} \frac{d}{dr} \left(r \frac{d\Phi_n}{dr} \right) + k_{rn}^2 \Phi_n + \sum_m \left[A_{nm} \Phi_m + (C_{nm} - 2B_{nm}) \frac{d\Phi_m}{dr} \right] = -2 \frac{\delta(r)}{r} \delta(z - z_s) \quad (2.34)$$

where, according to Brekhovskikh and Godin (1992),

$$A_{nm} = \int \frac{1}{r} \frac{\partial}{\partial r} \left(r \frac{\partial \Psi_m}{\partial r} \right) \frac{\Psi_n}{\rho} dz, \quad (2.35)$$

$$B_{nm} = \int \frac{\partial \Psi_m}{\partial r} \frac{\Psi_n}{\rho} dz, \quad (2.36)$$

2.3.5 Reciprocity of the Adiabatic Approximation

$$C_{nm} = \int \frac{\partial \rho}{\partial r} \frac{\Psi_n \Psi_m}{\rho^2} dz. \quad (2.37)$$

Equations (2.35) to (2.37) denote the basis of a *reference waveguide system* that represents the acoustic field in an inhomogeneous waveguide. The adiabatic approximation assumes that the coupling matrices A_{nm} , B_{nm} and C_{nm} are negligible (Jensen *et al.* 1994). As a result a *decoupled* equation is obtained from (2.34) that is similar to (2.21)

$$\frac{1}{r} \frac{d}{dr} \left[r \frac{d\Phi_n(r)}{dr} \right] + k_{rn}^2 \Phi_n(r) = -2 \frac{\delta(r)}{r} \frac{\Psi_n(z_s)}{\rho(z_s)}. \quad (2.38)$$

Equation (2.38) is an ordinary differential equation for which a solution in the WKB (Jensen *et al.* 1994) approximation is sought (without the source term) in the form of

$$\Phi_n(r) = A(r) e^{ik_r(r)}, \quad (2.39)$$

where $A(r)$ and $k_r(r)$ are real functions. This approximation is a representation in terms of local plane-wave solutions, propagating horizontally with wavenumber k_r (Frisk 1994; Jensen *et al.* 1994). With respect to (2.38), the approximation yields

$$\Phi_n(r) \simeq A \frac{e^{i \int_0^r k_{rn}(r') dr'}}{\sqrt{k_{rn}(r)}}. \quad (2.40)$$

Matching the solution (2.26) with the source term, the value of A is found as

$$A = \frac{\sqrt{2\pi}}{\rho(z_s)} e^{i\pi/4} \Phi_n(z_s). \quad (2.41)$$

Substituting this back into (2.17) will yield an *adiabatic approximation complex pressure field*

$$p(r, z) \simeq \frac{\sqrt{2\pi}}{\rho(z_s)} e^{i\pi/4} \sum_{m=1}^{\infty} \Psi_m(z_s) \Psi_m(r, z) \frac{e^{i \int_0^r k_{rm}(r') dr'}}{\sqrt{k_{rm}(r)r}}. \quad (2.42)$$

2.3.5 Reciprocity of the Adiabatic Approximation

Consider (2.42) to be defined in a cylindrical environment with the source positioned at the axis, azimuthally symmetric about the environment. Then the reciprocal exchange of the source and receiver will implicitly change the environment about the new source position. An unfortunate aspect of the adiabatic solution (2.42) is that it fails to satisfy reciprocity (Jensen *et al.* 1994). As a resolution to this problem Jensen *et al.* (1994) presented an *ad hoc* modification to (2.42) as

$$p(r, z) \simeq \frac{\sqrt{2\pi}}{\rho(z_s)} e^{i\pi/4} \sum_{m=1}^{\infty} \Psi_m(z_s) \Psi_m(r, z) \frac{e^{i \int_0^r k_{rm}(r') dr'}}{\sqrt{\int_0^r k_{rm}(r') dr'}}. \quad (2.43)$$

Although this is a good attempt at accommodating the inhomogeneities of the environment about the new source position, it remains an *ad hoc* solution that is not supported by any rigorous mathematical justification.

An important requirement of the OAR model is the ability to satisfy reciprocity in any general environment. A formal derivation that provides an expression of the adiabatic approximation that satisfies reciprocity is given by Brekhovskikh and Godin

(1992). The physical meaning of the approximation implies that (2.42) can be regarded as the leading term in a perturbation theory that can be applied to a more general three-dimensional case (Brekhovskikh and Godin 1992). The irregularities of the waveguide need to be smooth and small between the two points, r_s and r , with the following condition,¹¹

$$|k_{rm}(r) - k_{rm}(r_s)| \leq \varepsilon k_{rm}(r_s), \quad \varepsilon \ll 1. \quad (2.44)$$

Equation (2.42) describes a field in the adiabatic approximation to within a factor $[1 + O(\varepsilon)]$. However, a somewhat better result can be obtained if $k_{rm}(r)$ in the denominator of (2.42) is changed to, (Brekhovskikh and Godin 1992)

$$k_{rm}(r)k_{rm}(r_s) \int_0^r \frac{dr'}{k_{rm}(r')}. \quad (2.45)$$

This expression, (2.45), describes a modal amplitude correction to a general three-dimensional case that accounts for the out of plane propagation for horizontal rays. It stands to reason that such an expression can be reduced to a two-dimensional propagation case along a vertical plane. Therefore,

$$p(r, z) \simeq \frac{\sqrt{2\pi}}{\rho(z_s)} e^{i\pi/4} \sum_{m=1}^{\infty} \Psi_m(z_s) \Psi_m(r, z) \frac{e^{i \int_0^r k_{rm}(r') dr'}}{\sqrt{k_{rm}(r)k_{rm}(r_s) \int_0^r \frac{dr'}{k_{rm}(r')}}}. \quad (2.46)$$

As a result, validation of the reciprocity principle will be attained in a arbitrary slow varying almost layered medium. Finally, Brekhovskikh and Godin (1992) indicate that the mode amplitude relative error in (2.46) will be in the order of $O(\varepsilon^2)$.

¹¹This is physically a slow change between r_s and r .

¹²The gridded bathymetric data file was constructed using echo-soundings and data from various sources. This dataset was stored as a bathymetric database for the research area of this project. Greater detail of this compilation is described in Chapter 4 of this thesis.

2.4 OAR model Formulation

The focus of the OAR model was to implement the following expression, slightly modified from (2.46):

$$p(r, z) \simeq \frac{\sqrt{2\pi}}{\rho(z_s)} e^{i\pi/4} \sum_{m=1}^M \Psi_m(z_s) \Psi_m(r, z) \frac{e^{i \int_0^r k_{rm}(r') dr'}}{\sqrt{k_{rm}(r) k_{rm}(r_s) \int_0^r \frac{dr'}{k_{rm}(r')}}}} \quad (2.47)$$

where z and z_s are the hydrophones and source depths, respectively, r is the range and r' is the segmented range. The variable M represents the minimum number of modes excited between the source and receiver.

The following is a summary of the procedures used in the OAR IDL code to produce the adiabatic complex pressure field approximation. Samples of the OAR IDL code can be found in Appendix (A):

1. As described in section (2.3.4), the model begins by selecting a radial along an azimuth from the array to a point along the source track. The radial is segmented into a number of smaller range lengths.
2. Each segment along the radial corresponds to a specific latitude and longitude within the experimental region. The latitude and longitude coordinates are then converted to a corresponding ocean depth pre-determined from a gridded bathymetric data file (IDL code: A.2).¹²
3. Each corresponding ocean depth is associated with a specific sound speed profile (SSP) and geoacoustic properties that are used in the calculation of the mode functions Ψ_m and wave numbers k_{rm} . The latter variables are produced using ORCA for each range independent segment.

¹²The gridded bathymetric data file was constructed using echo-soundings and data from various sources. This dataset was stored as a bathymetric database for the research area of this project. Greater detail of this compilation is described in Chapter 4 of this thesis.

¹³Equation (2.47) has two integrals to process: $\int_0^r k_{rm}(r') dr'$ and $\int_0^r \frac{dr'}{k_{rm}(r')}$. Both are handled in the same fashion as described at item 5 (see IDL code: Appendix A.3).

4. For rapid repetitive computations of (2.47), the mode functions and wave numbers were pre-computed for a grid of values of the water depth and source depth and stored in “lookup” tables for fast reference. Dosso (1993) explained that within such an algorithm, the mode functions and wave numbers for a particular realization of water depth (or mode number m) can be calculated by linear interpolation between the stored values. If a sufficiently fine grid is chosen the linear approximation is accurate. In this case, the water depth ORCA calculations were gridded in 5 m steps (IDL code: Appendix A.1).
5. The integration in (2.47) was handled by a two-point *Trapezoidal rule* formula (Press *et al.* 1989),¹³

$$\int_0^r k_{rm}(r') dr' \cong \sum_i \Delta\phi(r_i) \quad (2.48)$$

$$\cong \sum_i \int_{r_{i-1}}^{r_i} k_{rm}(r') dr' \quad (2.49)$$

$$\cong \sum_i \Delta\phi(r_i) \left[\frac{1}{2} k_{rm}(r_{i-1}) + \frac{1}{2} k_{rm}(r_i) \right] \quad (2.50)$$

where $\Delta\phi(r_i)$ is the equally spaced abscissas of the integral between the two limits, 0 to r (see Figure 2.2 and IDL code: Appendix A.3).

6. As (2.47) allows for reciprocity, the 16-element hydrophone array configuration was substituted as a line of 16 sources in the expression and an *adiabatic* sum was produced combining all the segments of the radial to construct a complete complex pressure field (IDL code: Appendix A.5).

2.4.1 Wave Number and Mode Function Lookup Tables

Item (4) of the enumerated procedure in section (2.4) introduced the use of “lookup” tables as a fast reference to the wave number k_{rm} and mode function Ψ_m

¹³Equation (2.47) has two integrals to process: $\int_0^r k_{rm}(r') dr'$ and $\int_0^r \frac{dr'}{k_{rm}(r')}$. Both are handled in the same fashion as described at item 5 (see IDL code: Appendix A.3).

values. The construction of these tables proved to be a great deal more efficient than recomputing the modal values and integrating over the entire range of the radial each time the depth changed.

Lookup tables were pre-computed from the eigenfunction and eigenvalue files produced by ORCA for each respective depth and geoacoustic condition. The wave number tables included complex values of the eigenvalues for each respective depth in 5 m increments (2 dimensional matrix). Similarly, the mode function table included the complex form of the eigenfunction for each mode and water depth, incremented along the whole water column structure (3 dimensional matrix). A sample mode function from ORCA is shown in Figure 2.3.

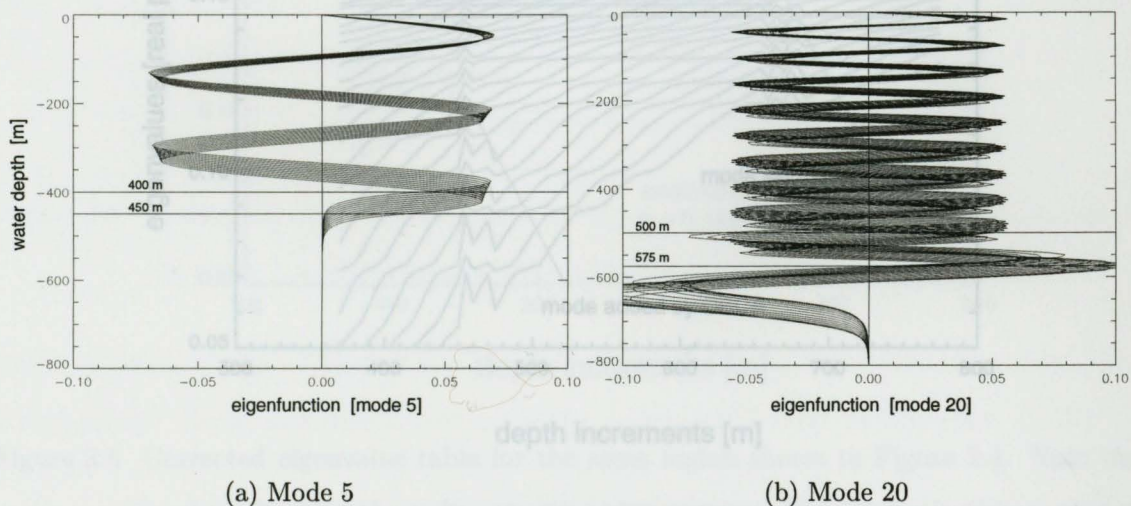


Figure 2.3 Samples of ORCA produced mode functions. (a) Mode 5 shown for water depths from 400 m to 450m, (b) Mode 20 shown for water depths from 500 m to 575m.

Figure 2.3(b) shows an *anti-resonant* pattern in the sediment layer, different than that seen in Figure 2.3(a). The existence of anti-resonance in a layered media is well described in Tolstoy (1956). It is a propagating pattern produced by the dramatic sound speed changes within a sediment/bottom layer. Such a behavior is *not* unexpected when working with inhomogeneous bottoms. According to Tolstoy (1956), the

anti-resonance in the layer is attributed to the nature of the boundary conditions and the acoustic impedances of both interfaces (ρc), which automatically match. The two wave guides of the water column and the bottom are then brought together, without violating boundary conditions, under the same eigenvalue k_m .

What is immediately noticeable when reviewing the wave number tables (Figure 2.4), is the inconsistencies in the modes as they progress from 370 m to 775 m of water depth.¹⁴

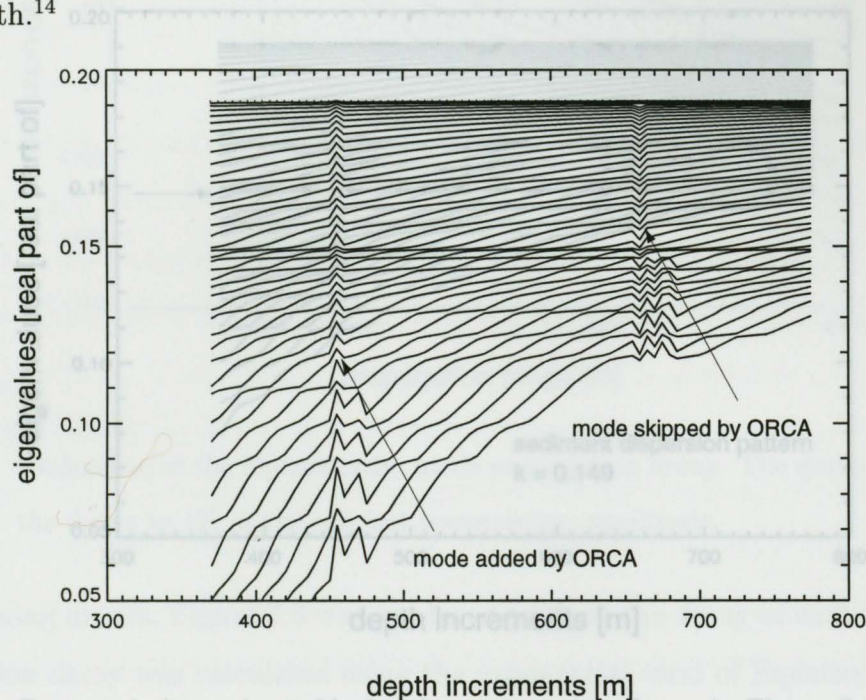


Figure 2.5 Corrected eigenvalue table for the same region shown in Figure 2.4. Note the

Figure 2.4 Lookup table for a region spanning 370 m to 775 m of water depth. The curves represent the real part of the eigenvalues associated with each mode number. One curve represents a specific mode number across the depth spectrum. Noticeable mode “jumps” are seen at different depths in the ORCA calculations. At some point in the calculations, the ORCA algorithm chose to add or skip a mode.

The reader will also observe from Figures 2.4 and 2.5 that the number of modes

Due to the adiabatic summation in Equation (2.47), such jumps or skips in mode

¹⁴This particular lookup table was constructed to accommodate the part of the source-receiver region that ranged in water depth from 370m to 775m.

number would result in an erroneous mode summation in the equation. A painstaking operation of manually removing each added mode (or adding a missing mode) was completed for each wave number table. By noting the mode added (or removed), the same manual procedure was applied to each respective mode function table. The results were “lookup” tables that contained matching mode numbers for each respective depth as shown in Figure 2.5.¹⁵

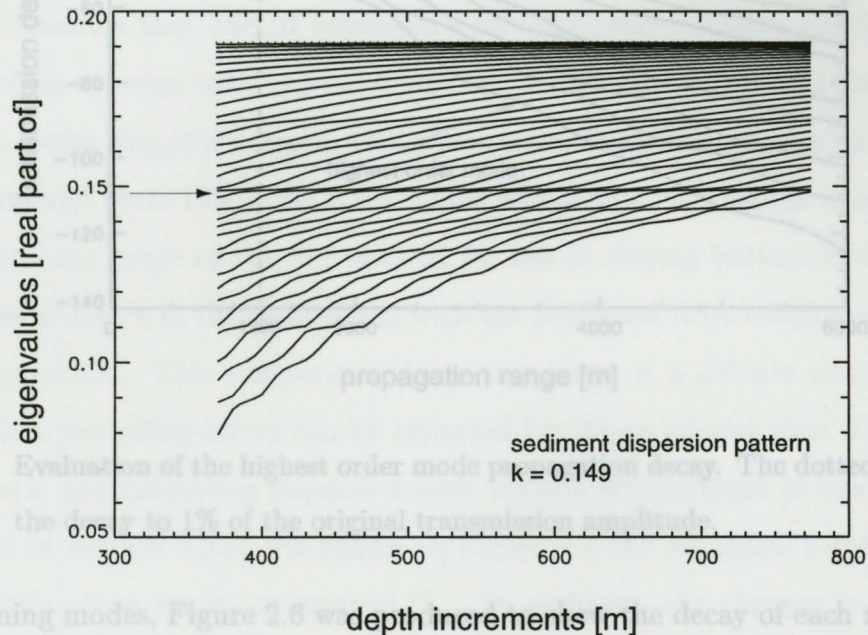


Figure 2.5 Corrected eigenvalue table for the same region shown in Figure 2.4. Note the arrow indicating the sediment dispersion pattern. The modes in this corrected table were reduced from 43 modes to 35 modes. This reduction is directly a result of the correction. The eight higher order modes were too corrupted to apply any corrections.

The reader will also observe from Figures 2.4 and 2.5 that the number of modes

¹⁵Examining the dispersion curves in Figure 2.5, a well defined pattern can be observed as denoted by the pointing arrow. A simple calculation, using Equation $k = 2\pi/c$ and $k = 0.149$ as the pattern wavenumber, yields a sediment sound speed of 1899 [m/s]. This correlates well with the bottom layer input of 1891 [m/s] used in the ORCA calculation. This value will be defined in greater detail in chapter 4 where geoaoustic parameters are found from model inversions or from published sources.

were reduced to 35 from 43 modes. The danger with the corrective procedure arises when too many modes may have been removed. To verify the *propagating power* of

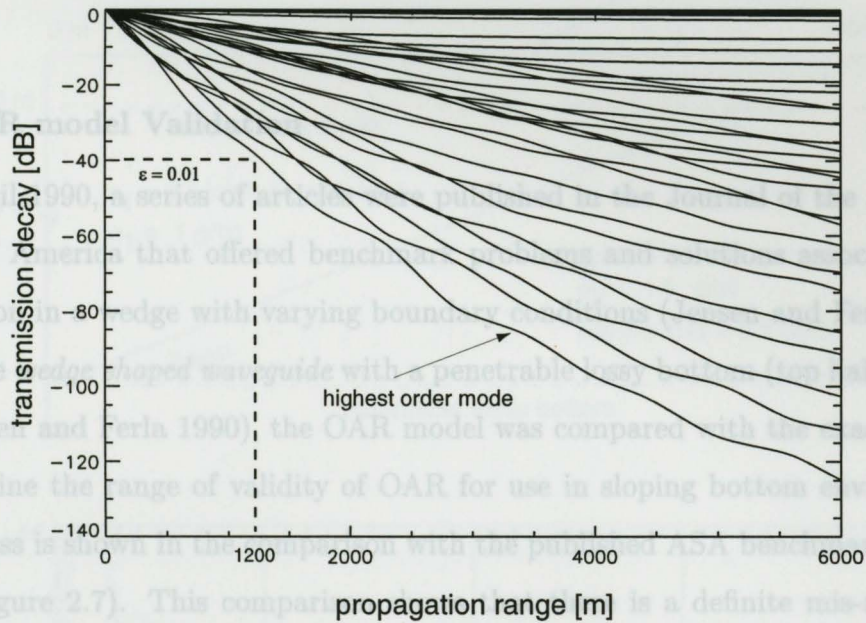


Figure 2.6 Evaluation of the highest order mode propagation decay. The dotted lines show the decay to 1% of the original transmission amplitude.

the remaining modes, Figure 2.6 was produced to show the decay of each mode. The transmission decay was calculated using the exponential term of Equation (2.47)

$$\text{decay} = 20 \log e^{k_{rm}r} \quad (2.51)$$

An arbitrary value of 1% of the original power was selected as a propagation threshold ($\epsilon = 0.01$). The reader can verify the mode table by looking at the highest order mode (35th) and determine the range at which it decays to 1% of the original power. All higher order modes will be more lossy at greater ranges, and therefore can be neglected. In the case seen in Figure 2.6, $20 \log \epsilon$ correspond to -40dB and a range of approximately 1200 m. It is reasonable to state that those higher order modes deleted from the “lookup” tables would have no significant contribution at

ranges greater than 1200 m. This assumption coincides with the *far-field* nature of adiabatic normal mode approximation.

2.5 OAR model Validation

In April 1990, a series of articles were published in the Journal of the Acoustical Society of America that offered benchmark problems and solutions associated with propagation in a wedge with varying boundary conditions (Jensen and Ferla 1990).

For the *wedge shaped waveguide* with a penetrable lossy bottom (top half of Figure 2.7) (Jensen and Ferla 1990), the OAR model was compared with the exact solution to determine the range of validity of OAR for use in sloping bottom environments. The process is shown in the comparison with the published ASA benchmark (bottom half of Figure 2.7). This comparison shows that there is a definite mis-match and suggests that modelling errors can be expected for slopes greater than 2.8° , or that the adiabatic approximation requires a slow varying environment of less than 2.8° , as denoted in section 2.3.5. As shown in Figure 2.7 the adiabatic solution breaks down for this slope angle (or greater).¹⁶ In addition, the changes in the water depths result in changes in mode numbers. As the energy is re-excited at each modal segment, errors in this adiabatic approximation are expected. The energy transfer cannot be expected to be the same as for coupled-modes models. Unfortunately, this comparison with the benchmark does not provide a direct test of the numerical implementation of the adiabatic approximation in OAR.

Since a reasonable comparison with published benchmarks could not be made, an independent analytic reference solution was required to validate the OAR model. An exact analytic solution to the adiabatic approximation was developed to validate the

¹⁶The irregularities in the waveguide need to be smooth and small between two points as shown by Equation (2.44) (Brekhovskikh and Godin 1992).

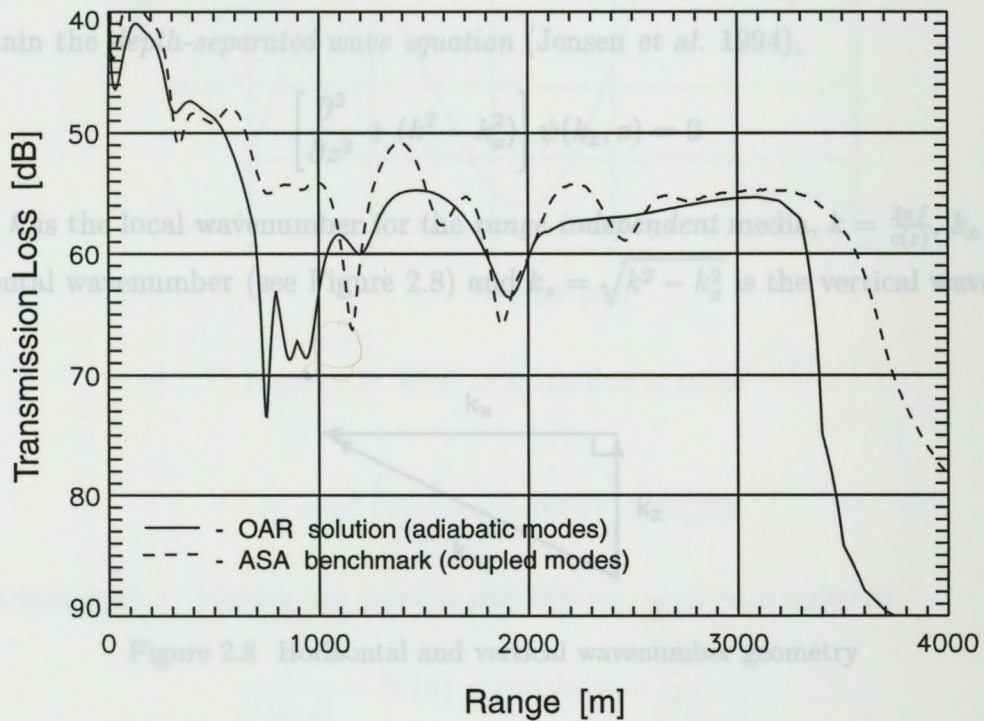
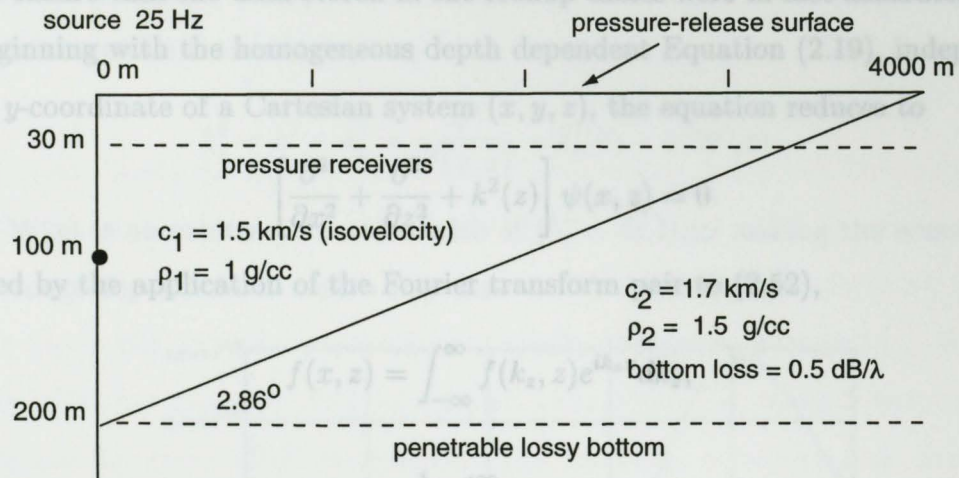


Figure 2.7 Coupled-mode solution for wedge with lossy penetrable bottom compared with OAR adiabatic approximation. Receiver at 30 m.

¹⁷The concept of the analytic solution was provided by Dr. Oleg Godin while the actual analytical product was produced independently by Dr. Ron Kessler that provided an "unbiased" comparison.

model's algorithm and codes.¹⁷ The critical importance of the following procedure was to ensure that the data stored in the lookup tables were in fact accurate.

Beginning with the homogeneous depth dependent Equation (2.19), independent of the y -coordinate of a Cartesian system (x, y, z) , the equation reduces to

$$\left[\frac{\partial^2}{\partial x^2} + \frac{\partial^2}{\partial z^2} + k^2(z) \right] \psi(x, z) = 0 \quad (2.52)$$

followed by the application of the Fourier transform pair to (2.52),

$$f(x, z) = \int_{-\infty}^{\infty} f(k_x, z) e^{ik_x x} dk_x, \quad (2.53)$$

$$f(k_x, z) = \frac{1}{2\pi} \int_{-\infty}^{\infty} f(x, z) e^{-ik_x x} dx, \quad (2.54)$$

to obtain the *depth-separated wave equation* (Jensen et al. 1994),

$$\left[\frac{\partial^2}{\partial z^2} + (k^2 - k_x^2) \right] \psi(k_x, z) = 0 \quad (2.55)$$

where k is the local wavenumber for the *range independent* media, $k = \frac{2\pi f}{c(z)}$, k_x is the horizontal wavenumber (see Figure 2.8) and $k_z = \sqrt{k^2 - k_x^2}$ is the vertical wavenumber.

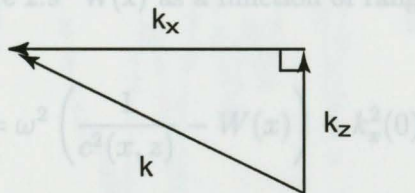


Figure 2.8 Horizontal and vertical wavenumber geometry

Therefore, (2.55) becomes

$$\frac{\partial^2 \psi(k_x, z)}{\partial z^2} + k_z^2 \psi(k_x, z) = 0. \quad (2.56)$$

¹⁷The concept of the analytic solution was provided by Dr. Oleg Godin while the actual analytical product was produced independently by Dr. Ron Kessel that provided an "unbiased" comparison.

Perfect adiabatic mode propagation is achieved when k_z and the mode function $\psi(k_x, z)$ are invariant (independent of x). We can construct a range dependent medium where this is true by setting

$$k_z^2 = k^2 - k_x^2 = \frac{\omega^2}{c^2(x, z)} - k_x^2(0) - \omega^2 W(x), \quad (2.57)$$

where $W(x)$ is an arbitrary function with $W(0) = 0$; then making the sound speed profile range dependent, in such a way that

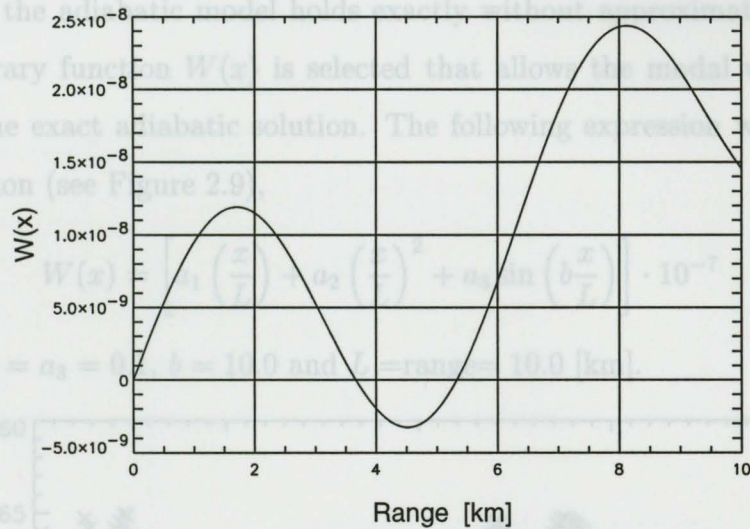


Figure 2.9 $W(x)$ as a function of range

$$k_z^2 = \omega^2 \left(\frac{1}{c^2(x, z)} - W(x) \right) - k_x^2(0) \quad (2.58)$$

is invariant with x . Making the term in parentheses equal to a constant,

$$\frac{1}{c^2(x, z)} - W(x) = \text{constant} = \frac{1}{c^2(0, z)} \quad (2.59)$$

then solving for $c(x, z)$, we find

$$c(x, z) = \sqrt{\frac{1}{\frac{1}{c^2(0, z)} + W(x)}}. \quad (2.60)$$

Using the same geometric principle employed earlier, we solve for the modal wavenumber,

$$k_x^2 = \frac{\omega^2}{c^2(x, z)} - k_z^2 = k_x^2(0) + \omega^2 W(x) \quad (2.61)$$

Equation (2.61) shows that the modal wavenumbers $k_x(x)$ can be computed at any range from the starting value at $x = 0$. The vertical mode functions remains the same at all ranges. Although the environment is artificially contrived, this is a case in which the adiabatic model holds exactly without approximation. Following this, an arbitrary function $W(x)$ is selected that allows the modal wavenumber to vary within the exact adiabatic solution. The following expression was chosen as a suitable function (see Figure 2.9),

$$W(x) = \left[a_1 \left(\frac{x}{L} \right) + a_2 \left(\frac{x}{L} \right)^2 + a_3 \sin \left(b \frac{x}{L} \right) \right] \cdot 10^{-7} \quad (2.62)$$

where $a_1 = a_2 = a_3 = 0.1$, $b = 10.0$ and $L = \text{range} = 10.0$ [km].

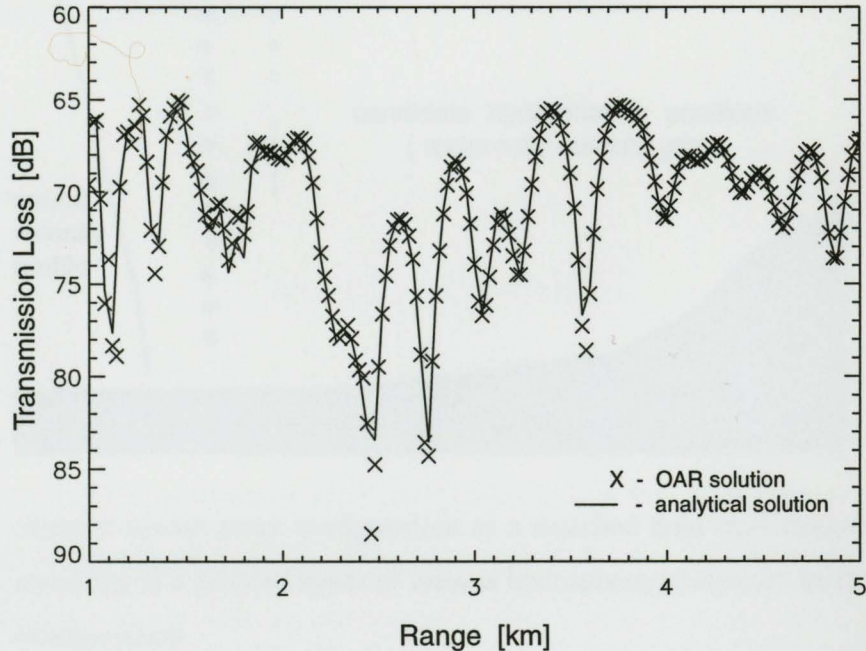


Figure 2.10 Analytic Vs. OAR solution.

Figure (2.10) shows the comparison with the exact analytic solution against that produced by the OAR model and lookup tables. As can be seen, a very good match is achieved proving through an exact and complete analytical method that the algorithms and codes of the OAR model produces accurate adiabatic results.¹⁸

3.1 Matched Field Processing

The technique of localization and tracking used in this project is a signal processing method referred to as *matched field processing* (Ducker 1976; Tolstoy 1993; Perkins *et al.* 1994; Jensen *et al.* 1994). It is a three-dimensional generalization of

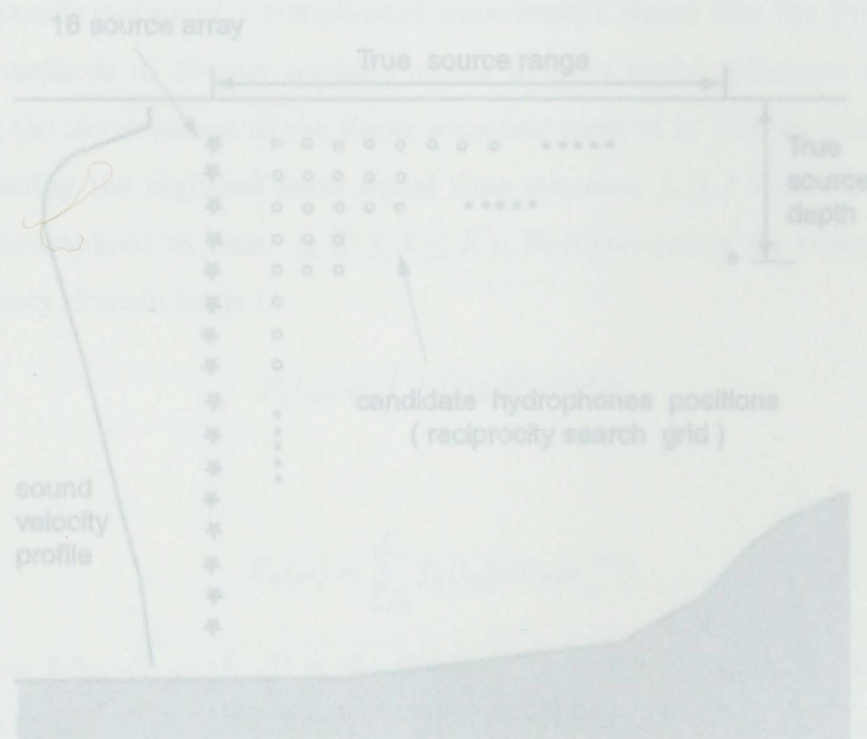


Figure 3.1 Vertical source array configuration in a matched field environment. Note the sampling of a gridded space of various hydrophone placement in this reciprocal configuration.

¹⁸Subsequent validation of the OAR model results were completed compared to ORCA and RAM produced results for range-independent conditions. In both cases OAR compared well and accurately with these proven models.

Chapter 3

Matched Field Source Localization

3.1 Matched Field Processing

The technique of localization and tracking used in this project is a signal processing method referred to as *matched field processing* (Bucker 1976; Tolstoy 1993; Perkins *et al.* 1994; Jensen *et al.* 1994). It is a three-dimensional generalization of

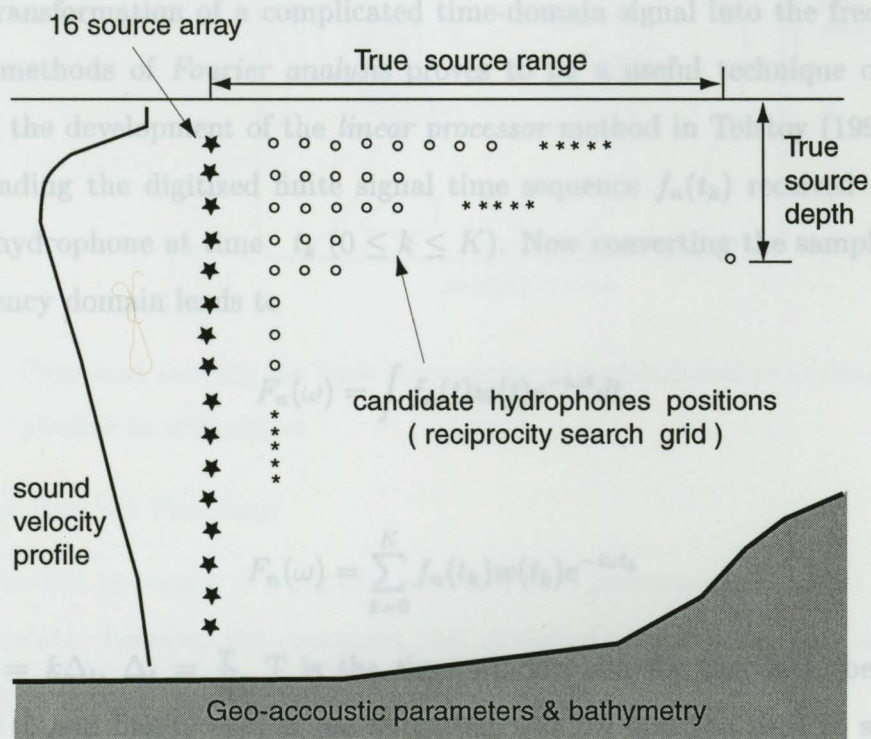


Figure 3.1 Vertical source array configuration in a matched field environment. Note the sampling of a gridded space of various hydrophone placement in this reciprocal configuration.

the conventional lower-dimensional plane-wave beamformer in which the plane wave

weighting vectors are replaced by solutions to the wave equation for the particular environment of interest (Perkins *et al.* 1994). Simply stated, the generalized matched field beamformer matches the measured field at the array with replicas of the expected field for all possible source locations (Jensen *et al.* 1994).¹ These replicas are derived from a propagation model, such as the adiabatic normal mode method discussed in chapter 2. To better illustrate this method, Figure 3.2 shows the basic components of MFP.

3.1.1 Measured Signal

The transformation of a complicated time-domain signal into the frequency domain by methods of *Fourier analysis* proves to be a useful technique of analysis. Following the development of the *linear processor* method in Tolstoy (1993), we begin by reading the digitized finite signal time sequence $f_n(t_k)$ received at the n th ($n \leq N$) hydrophone at time t_k ($0 \leq k \leq K$). Now converting the sampled data to the frequency domain leads to

$$F_n(\omega) = \int f_n(t)w(t)e^{-i\omega t}dt, \quad (3.1)$$

or

$$F_n(\omega) = \sum_{k=0}^K f_n(t_k)w(t_k)e^{-i\omega t_k} \quad (3.2)$$

where $t_k = k\Delta_t$, $\Delta_t = \frac{T}{K}$, T is the time window size for the data, beginning at time $t_1 = 0$, and finally $w(t)$ is the weighting/window function used to smooth out overshoots or ripples that result from the truncation in the time domain.

¹According to Tolstoy (1993), in the 1980s plane wave beamforming was the standard approach of acoustic signal processing. By the early 1990s, *matched field processing* began to attract attention as a valid method of source localization, geoacoustic inversion and model sensitivity evaluations. It is my opinion, that MFP will grow into the main component of signal processing for target acquisition within the next 10-15 years.

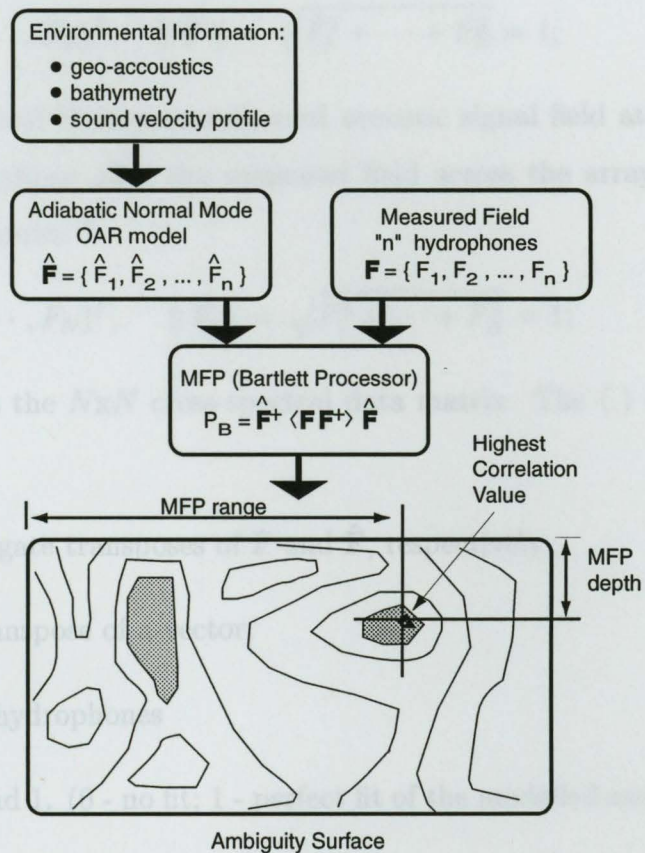


Figure 3.2 Flowchart showing the basic components of *matched-field processing* that is applicable to this project.

3.1.2 The Bartlett Processor

The Bartlett processor is a popular matched field processor which acts as a simple direct correlator between the measured and modelled fields. Its output value will be denoted as a “power” and is given by (Tolstoy 1993):

$$\mathcal{P}_B = \hat{\mathbf{F}}^* \underline{C} \hat{\mathbf{F}}. \quad (3.3)$$

The following itemization will define the attributes of Equation (3.3):

- \hat{F}_n is the modelled signal acoustic wave field at frequency ω on the n th hydrophone after the modelled field across the array has been sealed to have unit norm:

$$\hat{\mathbf{F}} = (\hat{F}_1, \hat{F}_2, \dots, \hat{F}_N)^T, \quad \|\hat{\mathbf{F}}\| = \sqrt{\hat{F}_1^2 + \dots + \hat{F}_N^2} = 1;$$

- F_n is the measured and Fourier transformed acoustic signal field at frequency ω on the n th hydrophone after the measured field across the array has been sealed to have unit norm:²

$$\mathbf{F} = (F_1, F_2, \dots, F_N)^T, \quad \|\mathbf{F}\| = \sqrt{F_1^2 + \dots + F_N^2} = 1;$$

- $\underline{\mathcal{C}} = \langle \mathbf{F}\mathbf{F}^* \rangle$. $\underline{\mathcal{C}}$ is the $N \times N$ cross-spectral data matrix. The $\langle \rangle$ denote the expected value;
- $\mathbf{F}^*, \hat{\mathbf{F}}^*$ are the conjugate transposes of \mathbf{F} and $\hat{\mathbf{F}}$, respectively;
- F^T describes the transpose of a vector;
- N is the number of hydrophones
- \mathcal{P}_B lies between 0 and 1. (0 - no fit; 1 - perfect fit of the modelled and measured field).

3.1.3 Cross-Spectral Matrix

The *cross spectral matrix* (CSM) in the MFP model is a necessary component that provides a means to measure the correlation between signal data measured at specific sensors in the array. The estimate of the CSM is obtained by averaging a number of data samples, measured at the array. When examining the measured acoustic fields, there will be variations in the amplitude and phase as a function of time that are attributed to a number of external variables. This is important, because the effects of these variabilities can be reduced by considering the matrix ($\underline{\mathcal{C}}$) which smoothes over the number of samples and reduces the effects of disturbances occurring *coherently* across the array to a negligible amount (Tolstoy 1993).

²The measured field contains both the signal and noise.

As seen in Figure 3.3, some factors that may affect phase disturbances are the “bobbing” up and down of the vertical array with the wave motion of the ocean and the non-vertical positioning of the hydrophones due to tidal/current activities. Also, by averaging the received data, the variance of the estimate is reduced and the signal contributions are emphasized by suppressing the uncorrelated noise.

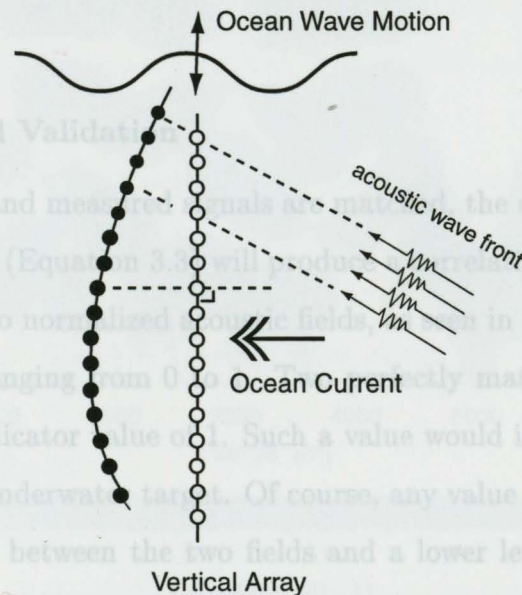


Figure 3.3 Factors such as up and down “bobbing” of the array and/or non-vertical layout of hydrophones due to current streams.

Considering a set of data collected over a period of time where the only appreciable change in conditions is the noise, then the entries of \underline{C} can be represented by:³

$$C_{nm} = \frac{1}{L} \sum_{l=1}^L F_{n,l}(\omega) F_{m,l}^*(\omega), \quad (3.4)$$

³A complete and precise derivation of a covariance matrix of smoothed cross spectral estimators can be found in Jenkins and Watts (1968), chapter 9 and Appendix 9.1 of the same text. Equation (3.4) is derived from an estimated covariance function based on the assumption that the time window is large enough to contain the entire transient response at each hydrophone receiver and as short as possible to determine a sampling frequency that will properly increment the frequency spectrum in order to delineate between noise and signal.

where (3.2) can be redefined as

$$F_{n,l}(\omega) = \sum_{k=0}^K f_{n,l}(t_k) w(t_k) e^{-i\omega t_k}. \quad (3.5)$$

The variable L denotes multiple, statistically independent, sets of data where $\{f_{n,l}(t_k)\}_{l=1}^L$ is collected over a period of time.

3.2 Matched Field Validation

When the replica and measured signals are matched, the output “power” value of the Bartlett processor (Equation 3.3) will produce a correlative indicator. The cross-spectral analysis of two normalized acoustic fields, as seen in section (3.1.2), provides a correlation gauge ranging from 0 to 1. Two perfectly matching fields will have a source localization indicator value of 1. Such a value would invoke a high confidence of the position of an underwater target. Of course, any value less than 1 would imply a mismatch condition between the two fields and a lower level of confidence to the target location.

Table 3.1 Match-Field Power Values (Validation case) for a source signal at 5000 m range and 45 m depth.

| Bartlett Power Value | range [m] | depth [m] |
|----------------------|-----------|-----------|
| 0.896574 | 5080 | 40 |
| 0.899150 | 4920 | 45 |
| 0.956487 | 4960 | 45 |
| * 0.999242 | 5000 | 45 |
| 0.987930 | 5040 | 45 |
| 0.934840 | 4080 | 45 |
| 0.923580 | 5000 | 50 |

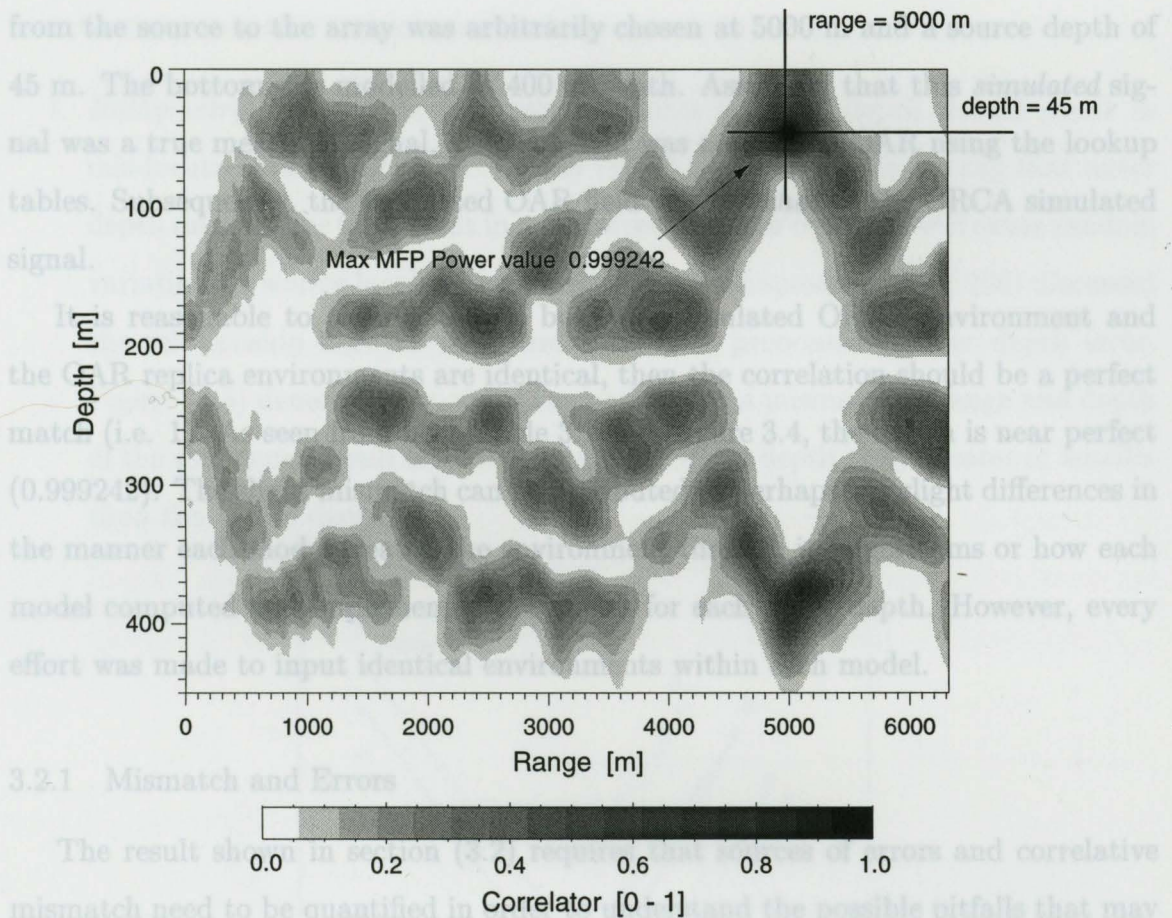


Figure 3.4 The ambiguity surface shows the result of the MFP using ORCA as the measured signal and OAR as the replica field. ORCA simulated a source at 45 m depth and 5000 m range within this particular vertical plane. The result shows a Bartlett Power output of 0.999242 at the same range and depth. A secondary “false-peak” or *side lobe* is seen in a non-source/undesirable location at range 5120 m and depth 375 m. The side lobe peak was calculated at 0.818399.

In an effort to validate the MFP algorithms and codes of the model, a *simulated* signal (at a given range and depth) was produced by ORCA and received at a *simulated* 16 hydrophone array. The scenario of this simulation was an attempt to approximate the geoacoustic environment of Pacific Shelf. A signal was gathered at 16 vertical positions similar in depth to the Pacific Shelf hydrophone array. A range

from the source to the array was arbitrarily chosen at 5000 m and a source depth of 45 m. The bottom was modelled at 400 m depth. Assuming that this *simulated* signal was a true measured signal, a replica field was created by OAR using the lookup tables. Subsequently, the replicated OAR field was *matched* to the ORCA simulated signal.

It is reasonable to assume that if both the simulated ORCA environment and the OAR replica environments are identical, then the correlation should be a perfect match (i.e. 1). As seen from both Table 3.1 and Figure 3.4, the match is near perfect (0.999242). The slight mismatch can be attributed to perhaps the slight differences in the manner each model treated the environment through its algorithms or how each model computed and implemented the modes for each water depth. However, every effort was made to input identical environments within each model.

3.2.1 Mismatch and Errors

The result shown in section (3.2) requires that sources of errors and correlative mismatch need to be quantified in order to understand the possible pitfalls that may result in matching a measured acoustic signal to an approximation of that signal via an acoustic model. Again, Tolstoy (1993) along with several other recent references (Feuillade *et al.* 1989; Gingras 1989; Hamson and Heitmeyer 1989; Tolstoy 1989) describe the mismatch factors of matched field processing.

Within the scope of this project, the mismatch effects were caused by propagation modelling errors and what are termed in section (3.1.3) as *external factors*, i.e. variables beyond the control of the researcher. These include variables such as noise, non-vertical or out of position hydrophones, and environmental parameters which are not known or incorrectly assessed.

In general, it is reasonable to state that no parameters, integral to the computation of MFP, can ever be known with precise accuracy. The following lists possible

contributions to errors and mismatch of true source location(s):

1. *Bathymetry.* Intuitively, incorrect estimates of water depth should result in mis-located source positions. Tolstoy (1993) confirms this by stating that water depth mismatches that result in an incorrect number of modes will cause random variations in source localization. Furthermore, Chapman *et al.* (1996) discussed the relationship between range estimates and pronounced water depth error. Figure (3.5) demonstrates, using ray paths, how a mismatch in range and depth of the source can result from estimating the water depth to be greater or smaller than the actual depth;

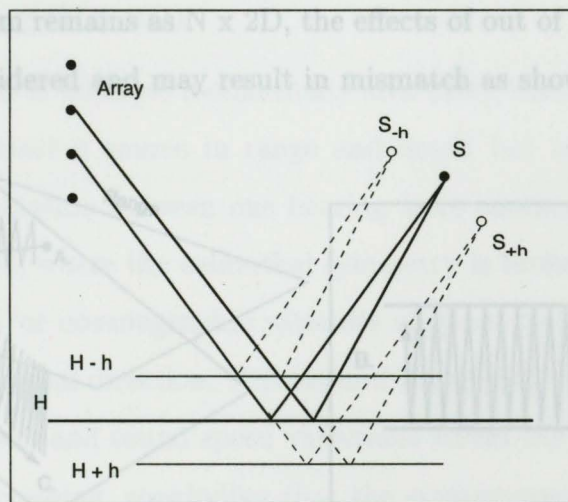
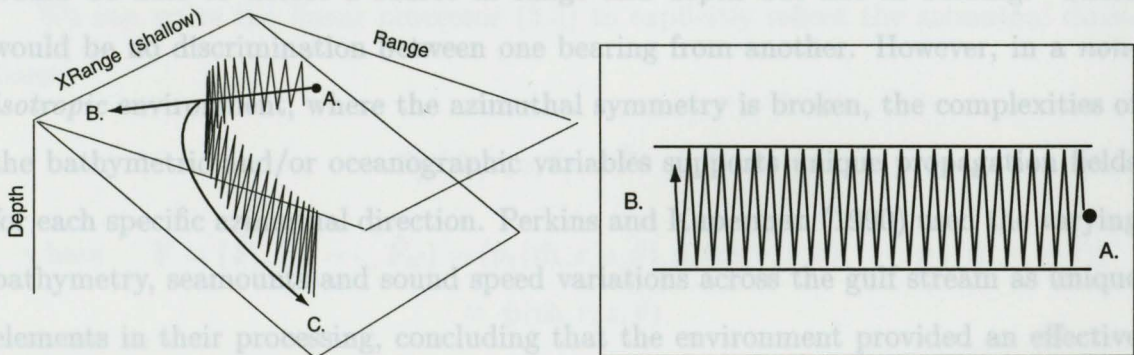


Figure 3.5 Selected eigenrays connecting the true source position S and two receivers (solid lines). If the modelled depth is assumed to be less or greater than the true depth, then by propagating the rays backward, the convergence occurs at mismatched source positions (dash lines).

2. *Geoacoustic parameters.* Particularly, in a shallow water environment, these parameters are important in acoustic propagation. Since shallow water sources excite bottom interacting modes (highest order modes - see section 2.4.1 and Figure 2.6) the source will be poorly localized if the bottom parameters are not

reliably known (Tolstoy 1993; Porter *et al.* 1991). In addition, Porter *et al.* (1987) examined effects of mismatch in bottom parameters that included sediment thickness, sediment compressional and shear wave speeds and gradients. They concluded that the largest effects of these bottom parameter mismatch was when the energy was not dominated by water-borne modes;

3. *Horizontal refraction.* Over an environment that is spatially varying in water depth, such as a continental slope, the effects of horizontally refracted propagation can affect the correct estimate of the source location, particularly when a modeller is analyzing the propagation along a 2-D vertical plane. As long as the model algorithm remains as $N \times 2D$, the effects of out of plane propagation are not being considered and may result in mismatch as shown in Figure 3.6(a);



(a) Horizontal Refraction

(b) Vertical plane propagation

Figure 3.6 (a) shows an exaggerated effect of refraction out of the vertical plane (A to C). When modelling in 2D, the propagation path will look like (b) and result in a sound path to point B, which is a mismatched propagation path.

4. *Sound speed profile, SSP.* The relatively small source ranges seen during this experiment ($\approx 5-6$ km) are not large enough to have significant changes in sound speed profile along a propagation path. However, sound speed mismatch

(i.e. if the current SSP is not known) is a considerable source of error that can result in a high probability of source mislocation (Bucker 1976; Tolstoy 1989; Gingras 1989).

There are numerous other sources of errors that cause source location mismatch. What has been described here are those that have the most apparent and pronounced effects. Truly, in an uncontrolled acoustic environment, these mismatches are ever present and can be a serious complication for the MF processor.

3.3 MFP Tracking (N x 2D)

If the environment is *isotropic* (azimuthally invariant), then a single vertical array would be able to detect a source in range and depth but not in bearing. There would be no discrimination between one bearing from another. However, in a *non-isotropic* environment, where the azimuthal symmetry is broken, the complexities of the bathymetric and/or oceanographic variables supports unique propagation fields for each specific azimuthal direction. Perkins and Kuperman (1990) used the varying bathymetry, seamounts and sound speed variations across the gulf stream as unique elements in their processing, concluding that the environment provided an effective horizontal aperture for bearing resolution using a fixed vertical array. For a moving target scenario, where the environment was not completely known, Ozard and Wilmut (1996) used a tilted array to create a horizontal aperture that artificially provided an environment asymmetry in a range independent bottom.

In this experimental region, the continental slope itself is a range-dependent environment that will provide the *non-isotropic* conditions that we require to track the target. From Equation (2.47), we can expand the expression to include azimuthal

$$P_B(\hat{m}, r, z, \theta, t) = \sum_{m=1}^{\infty} \Psi_m(\hat{m}, r, z, \theta) \Psi_m(\hat{m}, r, z, \theta) \quad (3.8)$$

³A similar approach has been applied to the adiabatic normal mode result shown in Perkins et al. (1994) that parameterize the adiabatic expression with azimuthal variability.

calculations and geoacoustic variability,⁴

$$p(\hat{\mathbf{m}}, r, z, \theta) \simeq \frac{\sqrt{2\pi}}{\rho(z_s)} e^{i\pi/4} \sum_{m=1}^{M(r,\theta)} \Psi_m(\hat{\mathbf{m}}, r=0, z_s, \theta) \Psi_m(\hat{\mathbf{m}}, r, z, \theta) \frac{e^{i \int_0^r k_{rm}(\hat{\mathbf{m}}, r', \theta) dr'}}{\sqrt{k_{rm}(\hat{\mathbf{m}}, r, \theta) k_{rm}(\hat{\mathbf{m}}, r_s, \theta) \int_0^r \frac{dr'}{k_{rm}(\hat{\mathbf{m}}, r', \theta)}}} \quad (3.6)$$

where θ is the azimuth bearing direction that spans an arc of investigation. $\hat{\mathbf{m}}$ is candidate modelled environmental parameter values where $\hat{\mathbf{m}} = \{m_i\}$ and m_i is the i th property within the spatially varying geoacoustic medium within a region of interest. Each medium is defined as $m_i = \{c_{p_i}(z), c_{s_i}(z), \rho_i(z), \alpha_{p_i}, \alpha_{s_i}, d(r)\}$ where c_p , c_s are sound speeds, ρ is density, α is attenuation and $d(r)$ is the changing bathymetry in range.

We can write the linear processor (3.3) to explicitly reflect the azimuthal directions:

$$\mathcal{P}_B(\hat{\mathbf{m}}, r, z, \theta) = \hat{\mathbf{F}}^* \underline{\mathcal{C}} \hat{\mathbf{F}}. \quad (3.7)$$

$$\text{where } \hat{\mathbf{F}} = (\hat{F}_1, \hat{F}_2, \dots, \hat{F}_N) = (\hat{p}_1(\hat{\mathbf{m}}, r, z, \theta), \hat{p}_2(\hat{\mathbf{m}}, r, z, \theta), \dots, \hat{p}_N(\hat{\mathbf{m}}, r, z, \theta)) \\ = \hat{\mathbf{p}}(\hat{\mathbf{m}}, r, z, \theta).$$

If a tracking element is introduced (i.e. a moving source), then (3.7) should reflect changes in the source signal in time t and any environmental changes such as diurnal or geographic variation in the sound speed profile. The reader would expect that the geoacoustic and bathymetric conditions would remain the same; however, in a case where the array position may be drifting freely, the modal values in r , z and θ also change. Therefore, to allow these variations in time we find,

$$\mathcal{P}_B(\hat{\mathbf{m}}, r, z, \theta, t) = \hat{\mathbf{p}}^*(\hat{\mathbf{m}}, r, z, \theta, t) \underline{\mathcal{C}}_t \hat{\mathbf{p}}(\hat{\mathbf{m}}, r, z, \theta, t). \quad (3.8)$$

⁴A similar approach has been applied to the adiabatic normal mode result shown in Perkins *et al.* (1994) that parameterize the adiabatic expression with azimuthal variability.

The expression $\mathcal{P}_B(\hat{\mathbf{m}}, r, z, \theta, t)$ in (3.8) now contains all the elements of a source transmitting a signal in *range*, *depth* and *bearing* from the array in a modelled environment, $\hat{\mathbf{m}}$. Ideally, in a perfect *non-isotropic* environment $\hat{\mathbf{m}}$ where each azimuthal direction is unique from all others, the maximum \mathcal{P}_B calculated in r and z for each θ would provide the target's location at time t . However, this is not always the case and as will be seen in later chapters, there are many variables that confuse the calculation of the matched field processes. Nonetheless, this attempt in compiling the best available environmental data to replicate the acoustic field will show interesting tracking results.

The analysis in this thesis covers the data collected during the MEVA 5 run. This trial run had a source towed along two arcs (as shown in Figure 1.5) over a 4 hour period from 1805 hrs to 2200hrs on the 15th Sept 1993.

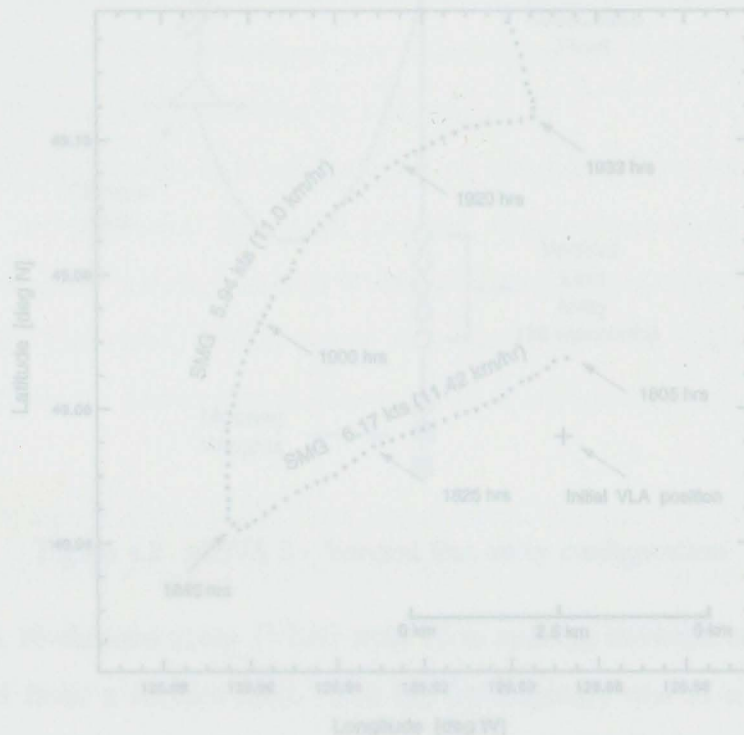


Figure 4.1 Towed track from 1805 hrs to 1930 hrs with indicated target *Speed Made Good* (SMG). The optimal SMG results using the matched field process are displayed by the solid lines. The SMG values are 8.64 kts (15.9 km/hr) and 6.17 kts (11.42 km/hr). Specifically, this thesis will look at the acoustic data emitted from the 45 Hz CW

Chapter 4

Ocean Acoustics Sea Trial - Pacific Shelf (MEVA 5)

Ten experiments with a Multi-Element Vertical Array (MEVA) were conducted by scientists from the Canadian Defence Research Establishment Pacific (DREP). Each MEVA run was designed to take advantage of the bathymetry of the particular Pacific shelf region. The analysis in this thesis covers the data collected during the MEVA 5 run. This trial run had a source towed along two arcs (as shown in Figure 1.5) over a 4 hour period from 1805 hrs to 2200hrs on the 15th Sept 1993.

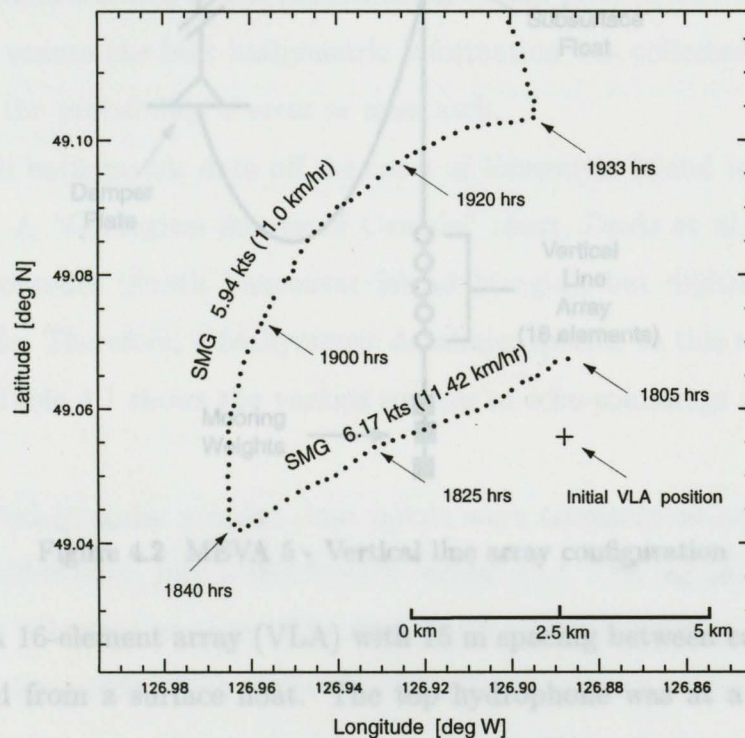


Figure 4.1 Towed track from 1805 hrs to 1930 hrs with indicated target *Speed Made Good* (SMG)

¹ Speed made good 6.17 kts (11.42 km/hr) along the linear track and 5.94 kts (11.0 km/hr) along the arc. Specifically, this thesis will look at the acoustic data emitted from the 45 Hz CW

tonal collected from 1805 hrs to approximately 1940 hrs, along the first towed arc (Figure 4.1). The source, a Marine Research Industries 219 Projector, was towed by CSS RICKER which recorded a *speed made good* of 6 kts (11.1 km/hr) from 1805 hrs to 1930 hrs.¹ Figure 4.2 shows the receiver system used in the MEVA 5

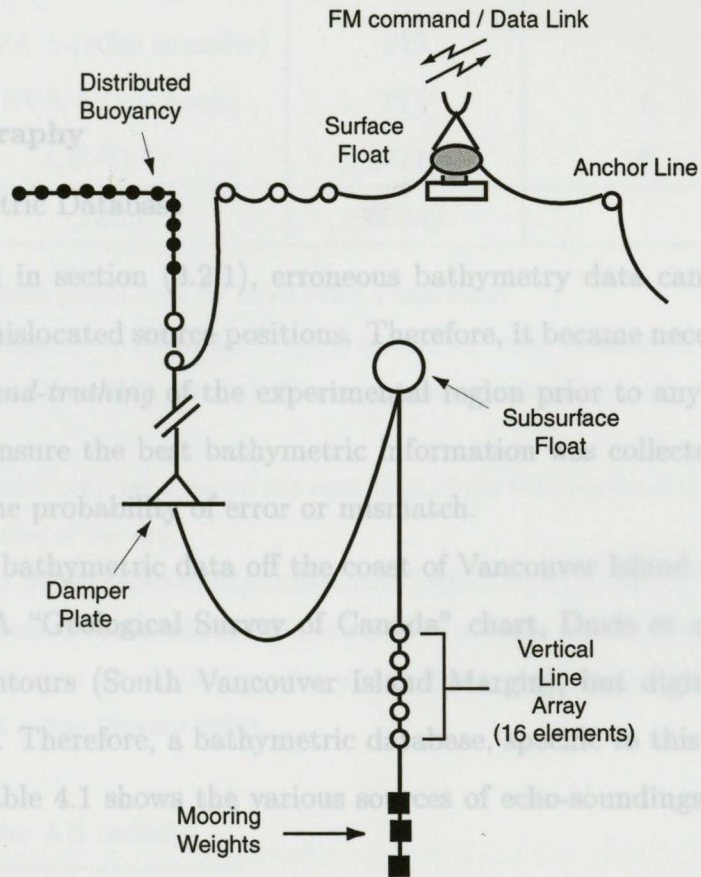


Figure 4.2 MEVA 5 - Vertical line array configuration

experiment. A 16-element array (VLA) with 15 m spacing between each hydrophone was suspended from a surface float. The top hydrophone was at a depth of 90 m and the bottom at 315 m, with a total aperture of 225 m. During this experiment, the array was positioned in water depth ranging from 383 m to 392 m. According to Tolstoy (1993), the optimal MFP results using a linear processor are obtained for

¹ *Speed made good* 6.17 kts (11.42 km/hr) along the linear track and 5.94 kts (11.0 km/hr) along the arc.

hydrophone spacing $\Delta_{hp} \leq \lambda$. In this case, the wavelength for a 45 Hz source is 33 m. In addition, optimal result will be observed when the array length spans as much of the water column as possible. This will allow the array to sample more of the changing acoustic field and thus to improve the MFP localization (Tolstoy 1993).

4.1 Oceanography

4.1.1 Bathymetric Database

As discussed in section (3.2.1), erroneous bathymetry data can be a significant contributor to mislocated source positions. Therefore, it became necessary to conduct a complete *ground-truthing* of the experimental region prior to any MF localization or tracking to ensure the best bathymetric information was collected and compiled, thus reducing the probability of error or mismatch.

Pacific shelf bathymetric data off the coast of Vancouver Island were found to be quite limited. A "Geological Survey of Canada" chart, Davis *et al.* (1987), shows well defined contours (South Vancouver Island Margin), but digitized information was unavailable. Therefore, a bathymetric database, specific to this experiment, was constructed. Table 4.1 shows the various sources of echo-soundings used to compile the database.

The collected irregular gridded data points were triangulated and interpolated, using an IDL subroutine, into a 40000-point regular grid. The regular depth grid was *smoothed* with a boxcar average. The final result, shown in Figure 4.4, represents contoured regular-gridded data of the original 60942 bathymetric data points. Using the regular-gridded data file as a bathymetric lookup table, an interpolation routine was coded that selected the bottom depths corresponding to a latitude and longitude along any arbitrary radial (i.e. point A to point B), including any desired interval

Table 4.1 Bathymetric database sources.

| <i>Source</i> | <i>Data points</i> | <i>* remarks</i> |
|-----------------------|--------------------|------------------|
| DREP | 331 | 1. |
| GSC Chart # 7 | 98 | 2. |
| MEVA 5 (echo sounder) | 219 | 3. |
| MEVA 5 (log book) | 175 | 4. |
| J.P. Tully | 60119 | 5. |
| <i>Total</i> | 60942 | |

1. Gridded data points used for other MEVA trial runs;
2. Specific data points manually collected around the outer parameters of the experimental region from GSC chart # 7 using a parallel ruler to identify latitudes and longitudes;
3. Echo sounder print out from on site recordings. Data were read at 5 minute interval for the duration of the run;
4. Tabulated results collected from experiment (MEVA 5) log book;
5. Sept 96 research cruise aboard DFO vessel J.P. Tully that collected seismic/acoustic data. A meticulous set of echo-sounding measurements was collected for an area near the MEVA 5 region (Spence 1996).

4.1.2 Geoacoustic data

segment along the AB radial.²

²The scaling and axes of the bathymetric and position charts were constructed using a *cylindrical projection* method that maps the globe to a cylinder which is formed by wrapping the UV plane around the globe with the U-axis coinciding with a great circle. A *pseudo-cylindrical projection* is specifically used here where global lines of latitude and longitude are parallel and straight while the meridians are curved lines. In this sinusoidal projection, the central meridian is a straight line and all others are equally spaced sinusoidal curves. Thus the scaling is true along the central meridian as well as along all parallels. The formulae given below give the relationship between latitude ϕ and the longitude λ of a point on the globe and its image on the UV plane:

$$u = \lambda \cos \phi$$

$$v = \phi$$

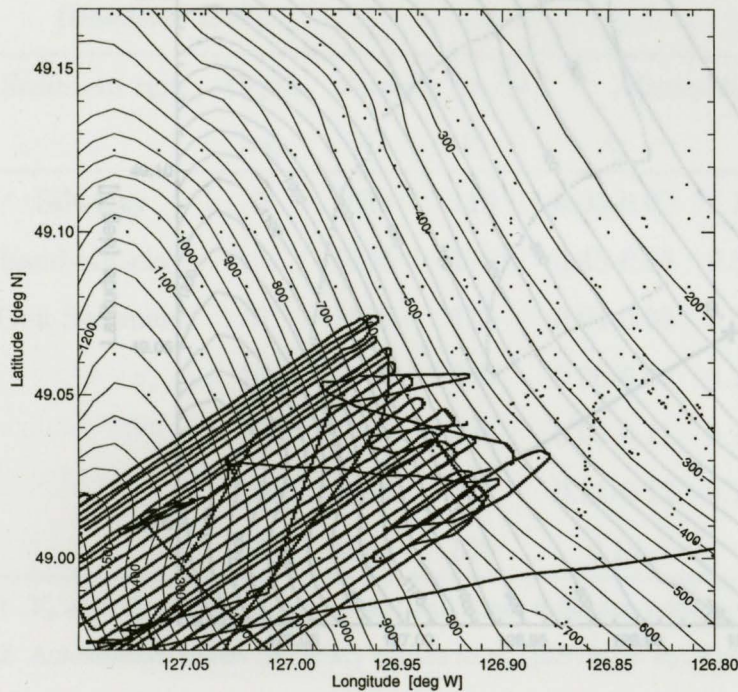


Figure 4.3 MEVA 5 experiment region showing location of all irregular gridded bathymetric points used in database. The tightly knit echo soundings was the J.P. Tully survey. The result of the 40000 point regular grid is shown as a contour overplot.

4.1.2 Geoacoustic data

The determination of the geoacoustic properties of the experimental region that relate directly to the analysis of this thesis was accomplished through several means. In a recent report by Hannay (1996), a broadband MFP estimation of geoacoustic parameters was completed in an area near this project site at the 400 m water depth contour line (see Figure 4.4). The report concluded that the top sediment layer was composed of *sand and sandy silt and a medium to fine-grained sand*. In a seismic/acoustic research cruise aboard the DFO vessel J.P. Tully in Sept 96, core

²Unpublished results - the information was gained through on site analysis of the core samples while I was aboard.

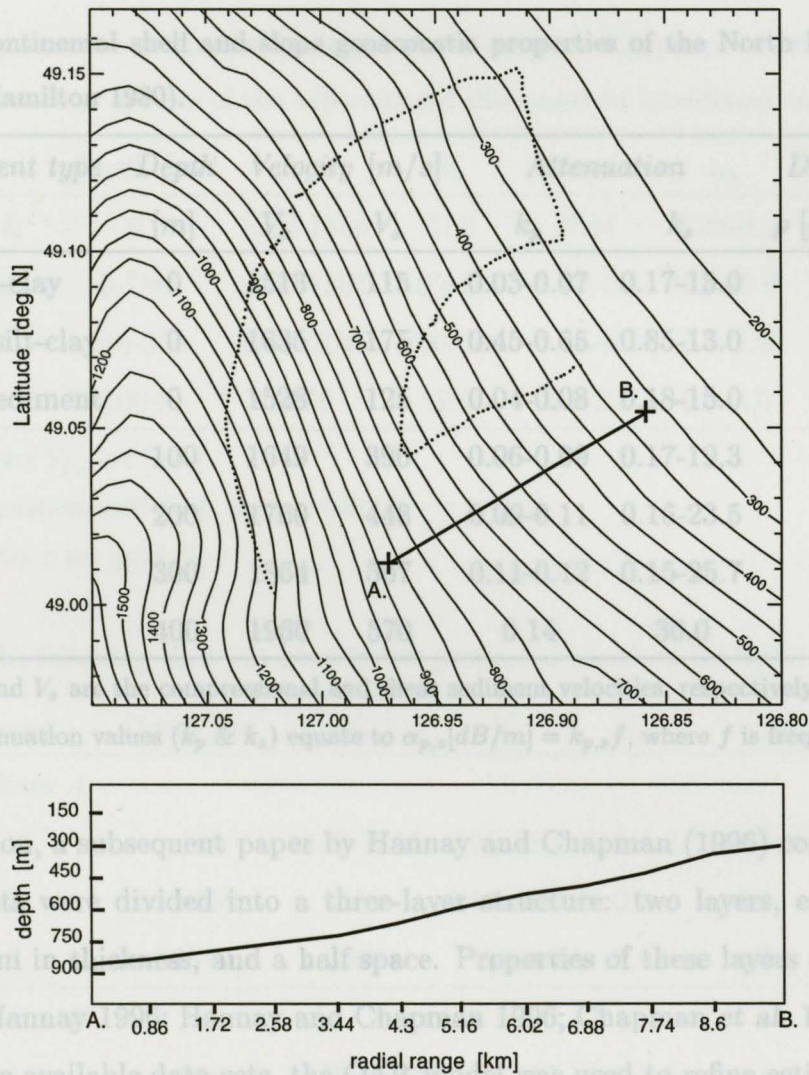


Figure 4.4 Contour chart for experimental region. The Figure shows two arbitrary selected points (A,B) and the interpolated depths along the AB radial. Each interpolated depth is associated with a latitude and longitude coordinate.

samples from the region shown in Figure 4.3 indicated a *silt and sand-silt-clay* composition.³ According to Hamilton (1980), these sediment types have average property values detailed in Table 4.2.

³Unpublished results - the information was gained through on site analysis of the core samples while I was aboard.

Table 4.2 Continental shelf and slope geoacoustic properties of the North Pacific region (Hamilton 1980).

| Sediment type | Depth [m] | Velocity [m/s] | | Attenuation α | | Density ρ [g/cm ³] |
|----------------|-----------|----------------|-------|----------------------|-----------|-------------------------------------|
| | | V_p | V_s | k_p | k_s | |
| Silt-clay | 0 | 1513 | 115 | 0.03-0.07 | 0.17-15.0 | 1.39 |
| Sand-silt-clay | 0 | 1635 | 175 | 0.45-0.65 | 0.85-13.0 | 1.78 |
| Gen Sediment | 0 | 1528 | 125 | 0.04-0.08 | 0.18-15.0 | 1.42 |
| | 100 | 1649 | 390 | 0.06-0.09 | 0.17-19.3 | 1.68 |
| | 200 | 1760 | 448 | 0.09-0.11 | 0.16-23.5 | 1.81 |
| | 300 | 1864 | 507 | 0.11-0.12 | 0.15-25.7 | 1.93 |
| | 400 | 1960 | 570 | 0.14 | 30.0 | 2.03 |

1. V_p and V_s are the compressional and shear sediment velocities, respectively;
2. Attenuation values (k_p & k_s) equate to $\alpha_{p,s}[\text{dB}/\text{m}] = k_{p,s}f$, where f is freq in kHz.

In addition, a subsequent paper by Hannay and Chapman (1996) concluded that the sediments were divided into a three-layer structure: two layers, each approximately 180 m in thickness, and a half space. Properties of these layers are shown in Table 4.3 (Hannay 1996; Hannay and Chapman 1996; Chapman *et al.* 1996).⁴

Using the available data sets, the OAR model was used to refine estimates of the geoacoustic parameters in the experimental region through a simple grid-search MFP inversion. The inversion was accomplished by fixing the source at a known range and depth. The grid-search inversion produced a set of geoacoustic parameters that correlated well with the known source position. Two separate data sets were found as shown in Table 4.4.⁵

Both data sets were subsequently used to construct two sets of lookup tables that

⁴Some of the parameters shown in Table 4.3 were also taken from model values input provided by Dr. N.R. Chapman

⁵Along range-independent grid-searches \mathcal{P}_B values were as high as 0.88.

Table 4.3 Geoacoustic properties based on the Hannay & Chapman (1996) report of a three-layer system of the experimental site based on broadband analysis

| <i>Sediment</i> | <i>Depth [m]</i> | V_p | V_s | α_p | α_s | ρ |
|-----------------|------------------|-----------|---------|------------|------------|---------|
| Sand & | 0 | 1500-1550 | 100 | 0.04 | 0.25-0.3 | 1.5 |
| Sand-silt | 0-180 | 1600-1891 | 100-200 | 0.09-0.8 | 0.25-2.0 | 1.5-1.6 |
| | 180-360 | 1891-2040 | 200-350 | 0.16-0.6 | 0.5-1.5 | 1.6-1.8 |
| | (360+) | 2066 | 550 | 0.2-3.0 | 0.5-4.0 | 2.1 |

1. Velocity $V_{p,s}$ are [m/s];

2. Attenuation coefficients $\alpha_{p,s}$ are [dB/ λ];

3. Density ρ are [g/cm^3].

Table 4.4 The following show the geoacoustic properties based on OAR/MFP inversions.

| <i>Layer</i> | <i>Depth [m]</i> | V_p | V_s | α_p | α_s | ρ |
|-----------------|------------------|-----------|---------|------------|------------|--------|
| <i>Medium A</i> | | | | | | |
| 1. | 0-150 | 1550-1800 | 125-350 | 0.3-0.5 | 0.3-0.3 | 1.6 |
| 2. | 150-350 | 1891 | 350-450 | 0.5 | 0.3 | 1.8 |
| 3. | 350+ | 2066 | 550 | 0.5 | 0.3 | 2.1 |
| <i>Medium B</i> | | | | | | |
| 1. | 0-200 | 1550-1800 | 125-350 | 0.3-0.5 | 0.3-0.3 | 1.6 |
| 2. | 200-400 | 1891 | 350-450 | 0.5 | 0.3 | 1.8 |
| 3. | 400+ | 2066 | 550 | 0.5 | 0.3 | 2.1 |

Medium A: parameters required to model when source in shallower water depths (i.e. from 250 m to 550-600 m).

Medium B: parameters required to model when source in deeper water depths (i.e. from 600 m to 850 m).

are easily called to model a specific area of the experimental area depending on the source location. Furthermore, the OAR-inversion results correlate well with those

found in Hamilton (1980) and Hannay and Chapman (1996).

4.1.3 Sound Speed Profile

Diurnal changes in sound speed profile can have a profound effect on sound transmission, particularly with the changes that occur within the surface layer. The speed is susceptible to daily and local changes such as solar heating, wind and currents. Urick (1975) showed that the diurnal changes of temperature over a 24 hour period can range up to 5° Celcius. Such a variation can contribute up to 10 m/s variability in the sound speed profile (Pickard and Emery 1990).

Over the entire period of the experiment (from 10 Sep to 18 Sep 93) 19 sound speed profiles were collected. During the MEVA 5 trial run, a profile was collected 2.5 hours prior to the start time and at the very end of the run at 2216hrs. However, no profiles were collected *during* the trial run.

Table 4.5 Sequential sound speed profile information, collected near MEVA 5 trial run.

| <i>Date</i> | <i>Time</i> | <i>Exp. File number</i> |
|-------------|-------------|-------------------------|
| 12 Sep 93 | 1328 hrs | # 24 |
| 14 Sep 93 | 1933 hrs | # 25 |
| 14 Sep 93 | 2238 hrs | # 26 |
| 15 Sep 93 | 1104 hrs | # 27 |
| 15 Sep 93 | 1532 hrs | # 28 |
| | 1800 hrs | <i>start MEVA 5</i> |
| | 2200 hrs | <i>end MEVA 5</i> |
| 15 Sep 93 | 2216 hrs | # 29 |
| 16 Sep 93 | 2042 hrs | # 30 |

Examination of SVPs #25 and #26 indicates an expected cooling effect, similar to that observed in SVPs #28 & #29 Figures 4.5 and 4.6. In addition, #26 to #27

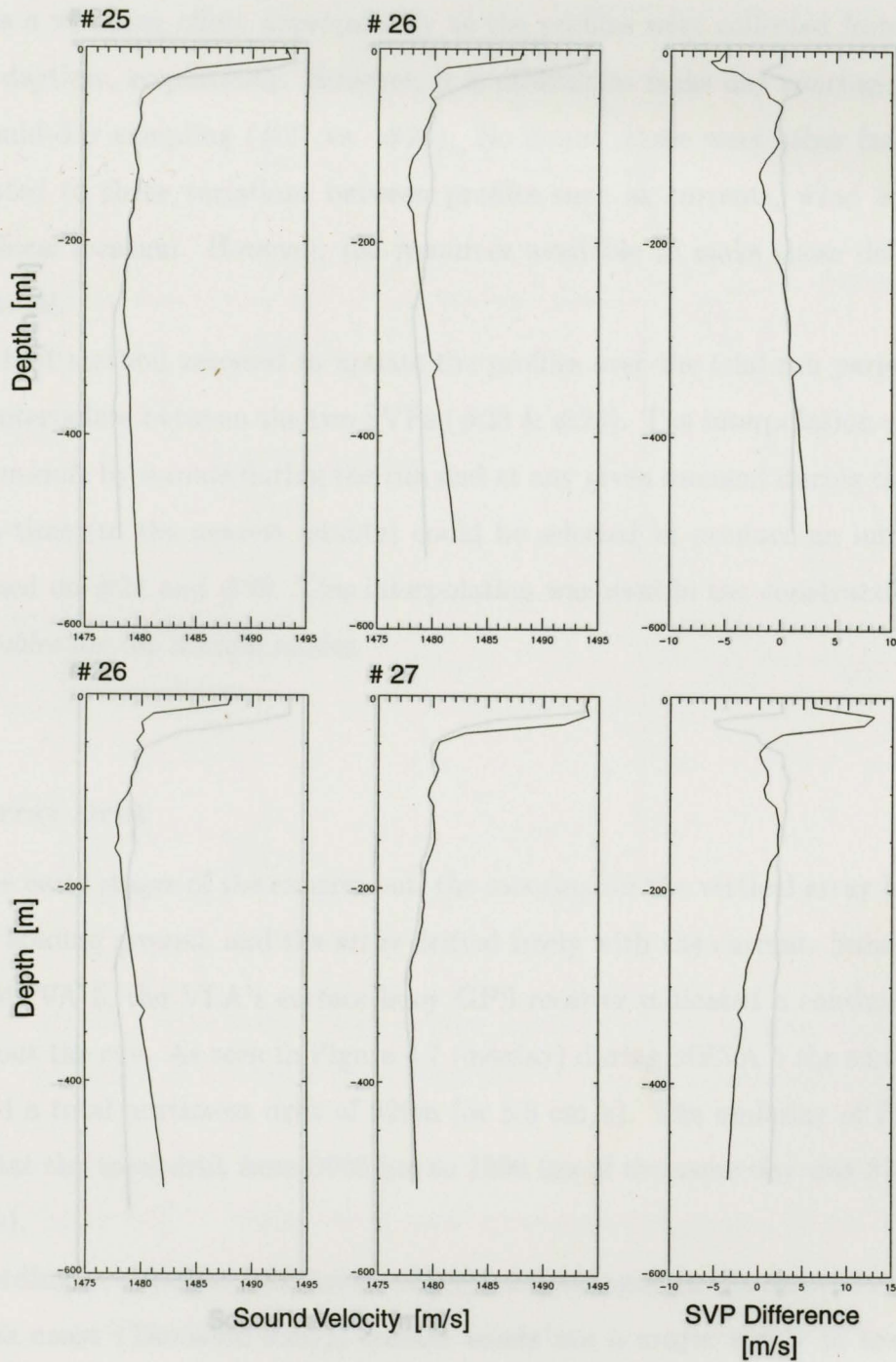


Figure 4.5 Diurnal variability of temperature: SVP #25, 26, 27.

SVP#25: 14 Sep - 1933hrs;

SVP#26: 14 Sep - 2238hrs;

SVP#27: 15 Sep - 1104hrs.

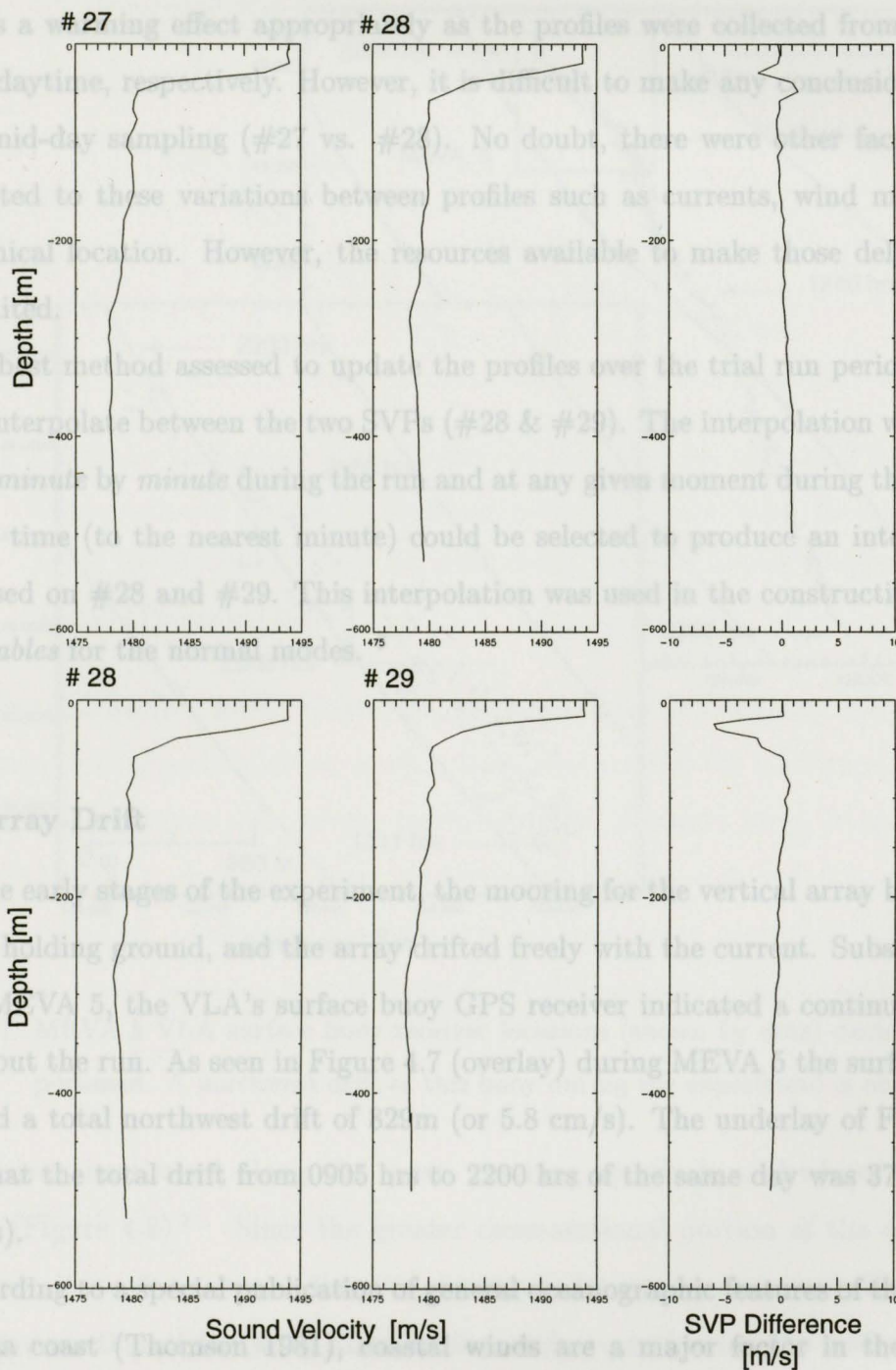


Figure 4.6 Diurnal variability of temperature: SVP #27, 28, 29.

SVP#27: 15 Sep - 1104hrs;

SVP#28: 15 Sep - 1532hrs;

SVP#29: 15 Sep - 2216hrs.

indicates a warming effect appropriately as the profiles were collected from evening time to daytime, respectively. However, it is difficult to make any conclusions based on the mid-day sampling (#27 vs. #28). No doubt, there were other factors that contributed to these variations between profiles such as currents, wind mixing, or geographical location. However, the resources available to make those delineations were limited.

The best method assessed to update the profiles over the trial run period was to simply interpolate between the two SVPs (#28 & #29). The interpolation was incremented *minute by minute* during the run and at any given moment during the MEVA 5 run, a time (to the nearest minute) could be selected to produce an interpolated SVP based on #28 and #29. This interpolation was used in the construction of the *lookup tables* for the normal modes.⁶

4.2 Array Drift

In the early stages of the experiment, the mooring for the vertical array broke free from its holding ground, and the array drifted freely with the current. Subsequently, during MEVA 5, the VLA's surface buoy GPS receiver indicated a continuous drift throughout the run. As seen in Figure 4.7 (overlay) during MEVA 5 the surface buoy exhibited a total northwest drift of 829m (or 5.8 cm/s). The underlay of Figure 4.7 shows that the total drift from 0905 hrs to 2200 hrs of the same day was 3755 m (or 6.9 cm/s).⁷ Since the greater cross-sectional portion of the array was

According to a special publication of general oceanographic features of the British Columbia coast (Thomson 1981), coastal winds are a major factor in the driving mechanisms of the non tidal circulation over the continental shelf and slope. Another distinguishable current is one that flows from the entrance of Juan de Fuca Strait

⁶The interpolated sound speed profiles were plotted and verified to ensure that the interpolated results were realistic.

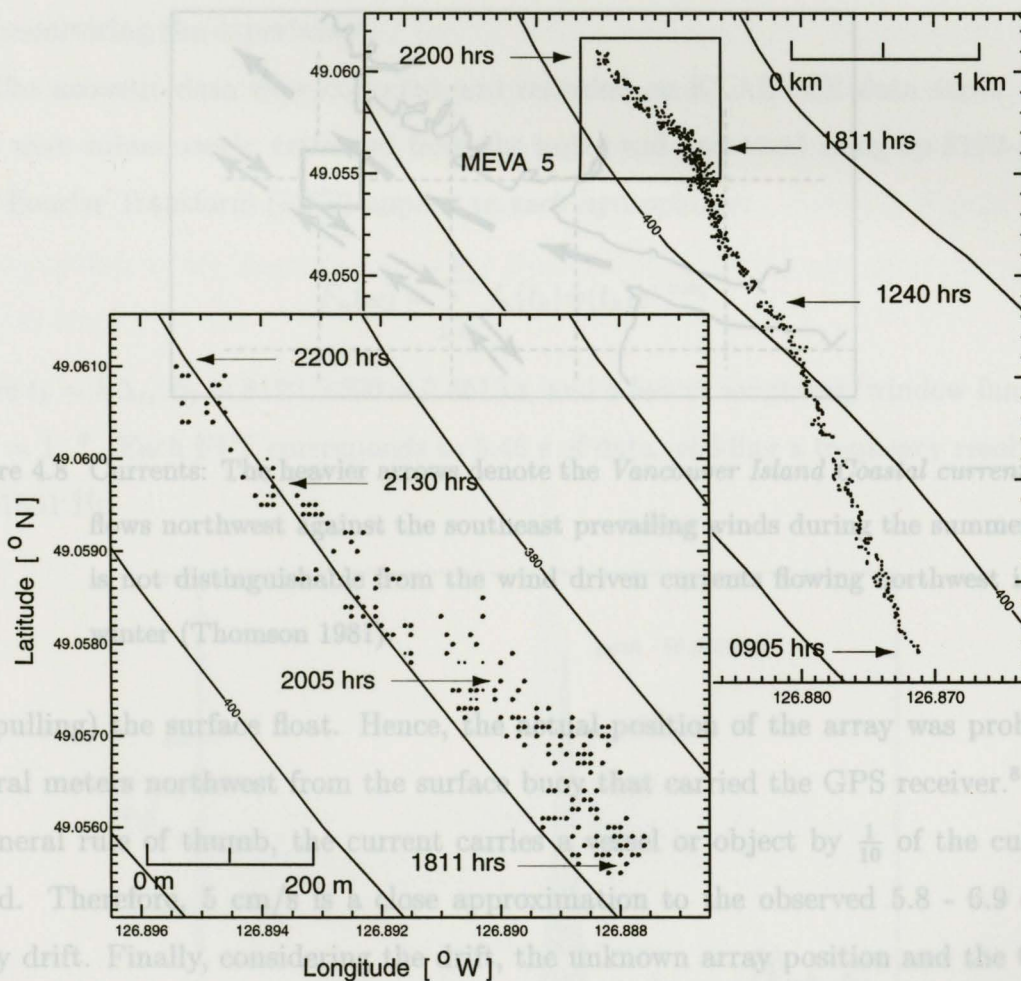


Figure 4.7 MEVA 5 VLA surface buoy receiver locations (shown by dots) during the experiment. A northwest drift of this buoy during the experiment is observed.

and is driven northward along the coast, reaching speeds in mid-winter of up to 50 cm/s (Figure 4.8).⁷ Since the greater cross-sectional portion of the array was underwater, it is safe to assume that the currents had a more pronounced effect on the underwater portion of the array than on the surface portion (or the surface buoy). The underwater portion, drifting freely with the currents, was most likely leading

⁷The marine synopsis for 15 Sep 93 for the region indicated a high pressure ridge slowly building to the south giving light to moderate winds (10-20kts). A log entry for the experiment stated "... [near] perfect conditions, almost a flat calm [sea]."

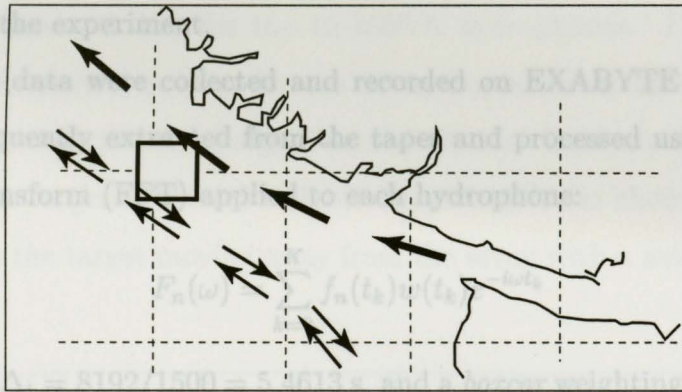


Figure 4.8 Currents: The heavier arrows denote the *Vancouver Island Coastal current* that flows northwest against the southeast prevailing winds during the summer and is not distinguishable from the wind driven currents flowing northwest in the winter (Thomson 1981).

(or pulling) the surface float. Hence, the actual position of the array was probably several meters northwest from the surface buoy that carried the GPS receiver.⁸ As a general rule of thumb, the current carries a vessel or object by $\frac{1}{10}$ of the current speed. Therefore, 5 cm/s is a close approximation to the observed 5.8 - 6.9 cm/s array drift. Finally, considering the drift, the unknown array position and the GPS, the error associated with the known position of the array was in the order of 100-200 m.

4.3 Received Signal Processing

The signals received at the VLA were recorded digitally at a rate of 1500 Hz at an underwater electronics unit. This signal was transmitted over a RF data link from the surface float to CFAV ENDEAVOUR, that was maintaining station to the VLA

⁸The Global Positioning System used in 1993 did not have the availability of differential positioning. At the time of this experiment the error of the GPS position indicator fell within 100 m.

and monitoring the experiment.

The acoustic data were collected and recorded on EXABYTE data tapes. The data were subsequently extracted from the tapes and processed using an 8192-point Fast Fourier Transform (FFT) applied to each hydrophone:

$$F_n(\omega) = \sum_{k=0}^K f_n(t_k)w(t_k)e^{-i\omega t_k} \quad (4.1)$$

where $t_k = k\Delta_t$, $\Delta_t = 8192/1500 = 5.4613$ s, and a *boxcar* weighting/window function $w(t) = 1$.⁹ Each FFT corresponds to 5.46 s of data, yielding a frequency resolution of 0.1831 Hz.

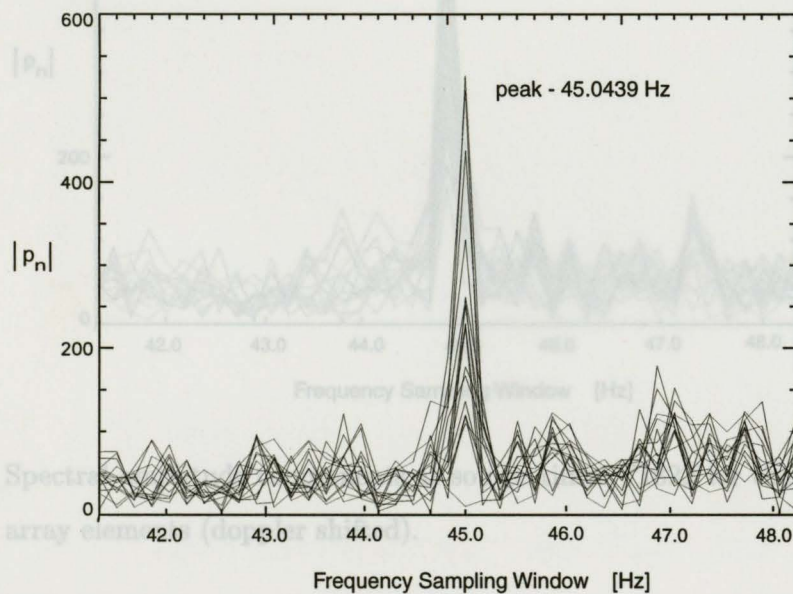


Figure 4.9 Spectral amplitude components at source time: T1920 for the 16 hydrophone array elements.

An algorithm was written to save 41 FFT frequency samples about the center

⁹The *boxcar* weighting function was used as the fourier truncation did not produce large overshoots or ripples that required smoothing. As will be seen in Figures 4.9 and 4.10, the source strength from the towed body was very strong. In addition an evaluation was made of the weighting functions to conclude that with a strong and distinct signal (such as the ones seen in Figures 4.9 and 4.10) the choice of a Hanning versus Boxcar or other windows made no apparent difference in the signal peak amplitudes.

frequency of interest (45 Hz) for the 16 MEVA hydrophones. Figure (4.9) shows the 41 measured spectral powers for the 16 hydrophones at an arbitrary selected time of 1920 hrs, with the tonal signal at 45.0439 Hz. Between 1810 hrs and 1940 hrs, however, the target exhibited a down doppler shift (as shown in Figure 4.10) corresponding to the target moving away from the array with a new spectral peak at 44.8608 Hz.

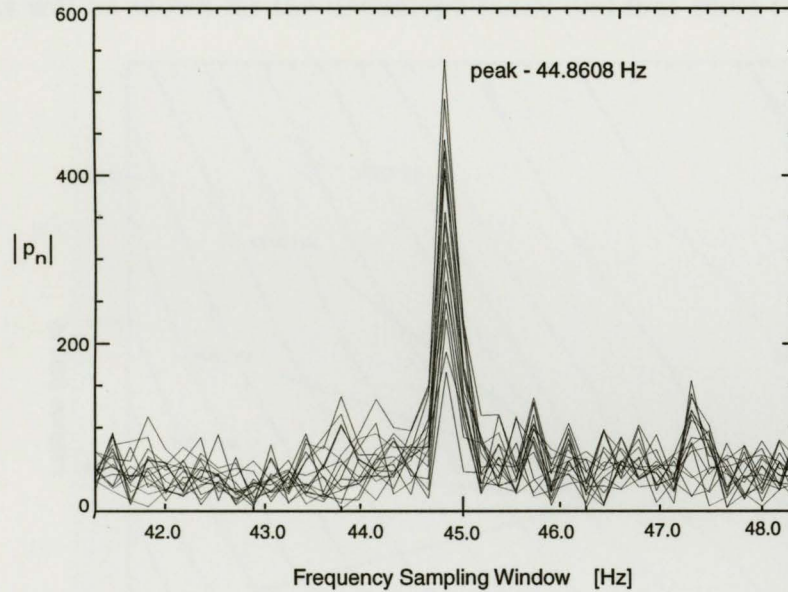


Figure 4.10 Spectral amplitude components at source time: T1822 for the 16 hydrophone array elements (doppler shifted).

Using Equation (3.4), the cross spectral matrix was computed for each spectral component that was projected at the source,

$$C_{nm} = \frac{1}{L} \sum_{l=1}^L F_{n,l}(\omega) F_{m,l}^*(\omega), \quad (4.2)$$

where

$$F_{n,l}(\omega) = \sum_{k=0}^K f_{n,l}(t_k) w(t_k) e^{-i\omega t_k} \quad (4.3)$$

The process was repeated for successive data segments and the cross spectral matrices for seven integration periods ($L = 7$ or 38.22 s seconds) were averaged. The choice

of FFT length (5.4613 s) and FFT average (38.22 s) is a trade off between improving signal-to-noise ratio (SNR) with a longer FFT and improving signal stability with a shorter FFT due to the source moving over a range dependent environment. This averaged result was used in the MF algorithm.

In this chapter, the *Matched-Field Localization and Ambiguity Surface Tracking (MFL-AST)* results will be shown for the downslope radial and first short-range arc of the

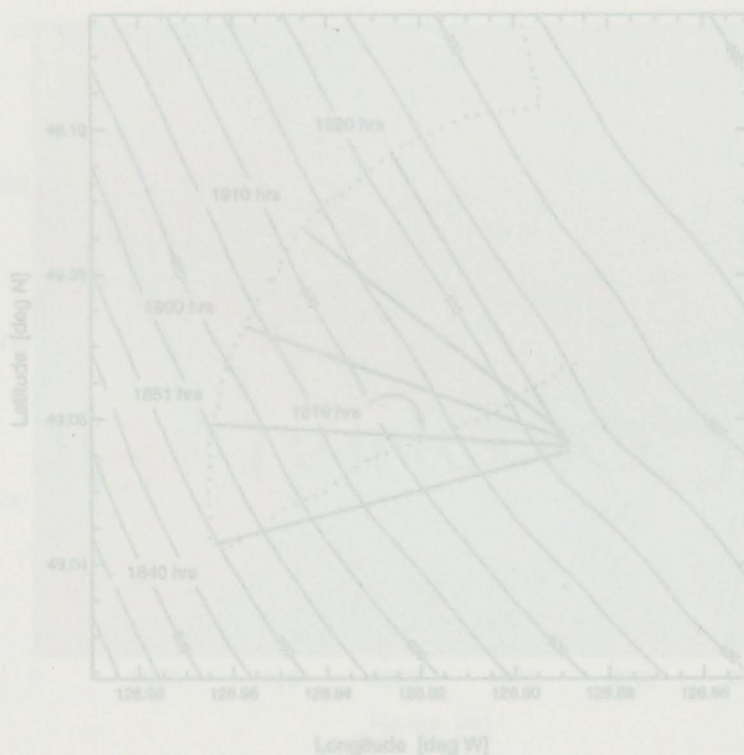


Figure 5.1 Target tracking (1805-1937 hrs). Six radials of interest at 1819 hrs, 1840 hrs, 1851 hrs, 1900 hrs, 1910 hrs and 1920 hrs, that describe the different features of the bottom contour and bathymetric symmetry

MEVA 5 tracking run, from 1 nm to 6 nm (1805 hrs to 1937 hrs) for a source transmitting a CW tonal at 45 Hz (Figure 5.1). As mentioned earlier, the source depth indicator was unserviceable and therefore only the GPS positions for the VLA and

Chapter 5

Matched-Field Localization and Surface to Surface Tracking

In this chapter, the *Matched-Field Localization and Ambiguity Surface Tracking* (MFL-AST) results will be shown for the downslope radial and first short-range arc of the

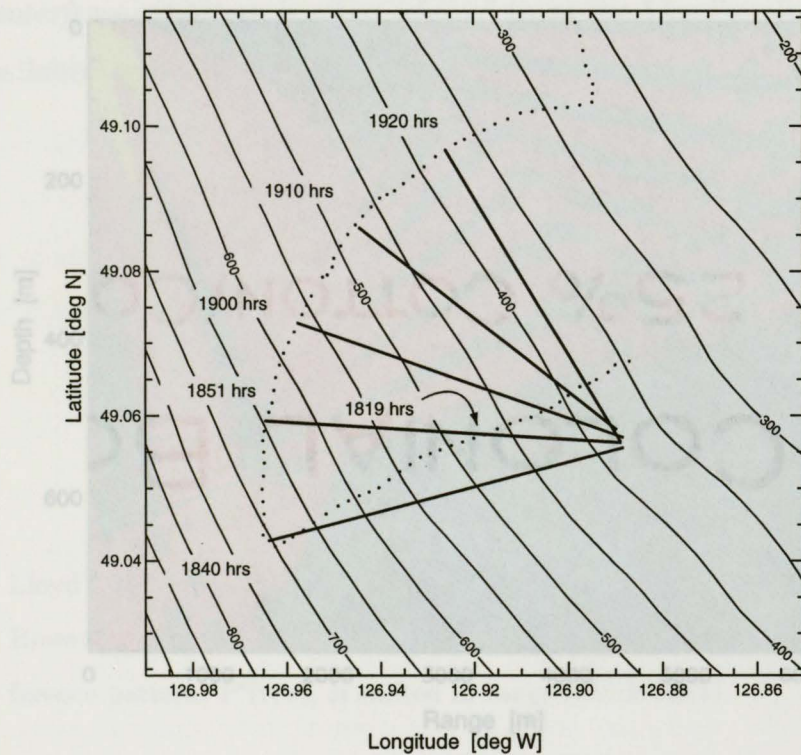


Figure 5.1 Target tracking (1805-1937 hrs). Six radials of interest at 1819 hrs, 1840 hrs, 1851 hrs, 1900 hrs, 1910 hrs and 1920 hrs, that describe the different features of the bottom contour and bathymetric symmetry

MEVA 5 tracking run, from 1 nm to 6 nm (1805 hrs to 1937 hrs) for a source transmitting a CW tonal at 45 Hz (Figure 5.1). As mentioned earlier, the source depth indicator was unserviceable and therefore only the GPS positions for the VLA and

the source tow-vessel, CSS RICKER, were available to verify any localization and tracking results. From a log entry (0900 hrs 15 Sep 93), 292 ft of tow-cable was payed out and an “eye-ball” estimation of the tow-cable angle to the water surface produced an estimation of the source depth to be 35-45 m.

An examination of the field reveals some distinctive features such as the lobing pattern from the source that is attributed to an interference pattern produced from

5.1 Observation 1: OAR model propagation results

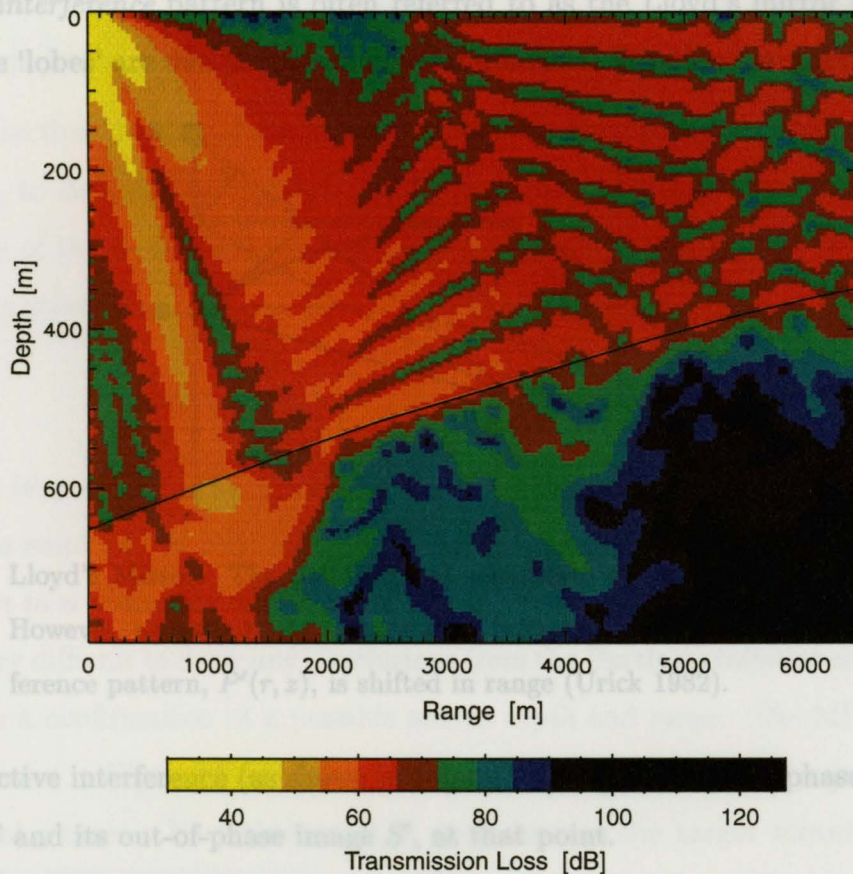


Figure 5.2 OAR-produced acoustic propagation field along T1851 Radial. For this geometry, the propagation is upslope from the target. The thin dark line represents the seafloor. Source at 0 m range and 45 m depth.

¹Each range bin is 100 m wide. The magnitude GPS fix from the drifting array.

17. For each desired radial from the 16-element VLA an OAR-produced propagation field was calculated.¹ Selected from Figure 5.1, the 1851 hrs radial was arbitrarily chosen as an example of the modelled field representing sound propagation upslope from the source (Figure 5.2).

An examination of the field reveals some distinctive features such as the *lobing* pattern from the source that is attributed to an interference pattern produced from the dipole configuration of the source S and its out-of-phase image S' . This *surface reflection interference* pattern is often referred to as the Lloyd's mirror field (Urick 1982). The 'lobes' are due to constructive interference. Whether the point P is a site

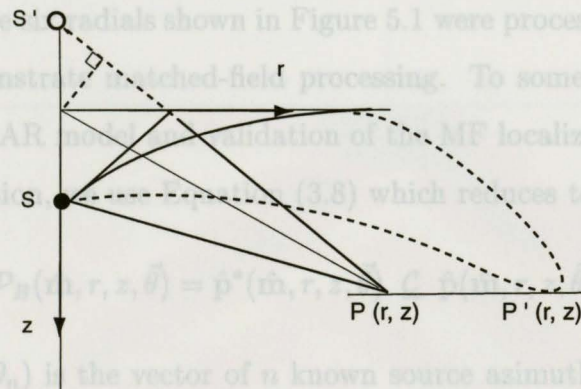


Figure 5.3 Lloyd's Mirror. The point $P(r, z)$ assumes a straight line propagation path. However, acoustic paths are generally refracted by the SV profile and the interference pattern, $P'(r, z)$, is shifted in range (Urick 1982).

of constructive interference (as shown in Figure 5.3) depends on the phase difference, between S and its out-of-phase image S' , at that point.

Observation of the acoustic field at the sloping bottom shows that at an approximate range of 2000 m the sound paths are reflected back with little propagation into the sediment. Using Equation (1.2) to calculate the *critical grazing angle*, a value of

¹Each radial had to be calculated from an updated latitude-longitude GPS fix from the drifting array.

17.4° is obtained.² At 1000 m the incident angle is estimated to be 29.75° and at 2000 m the incident angle is 17.0°. Hence, as seen in Figure 5.2, all angles incident at greater ranges than 2000 m will be reflected, losing some energy to the visco-elastic properties of the bottom. Other familiar characteristics along the slope can be examined such as modal leakage and the steepening of the sound paths as they interact with the upslope bottom (see section 1.2.1).

5.2 Observation 2: Matched-field localization - azimuth assumed known

In this section the six radials shown in Figure 5.1 were processed, assuming known azimuths, to demonstrate matched-field processing. To some degree, this allowed verification of the OAR model and validation of the MF localization algorithms.

For this observation, we use Equation (3.8) which reduces to:

$$\mathcal{P}_B(\hat{\mathbf{m}}, r, z, \vec{\theta}) = \hat{\mathbf{p}}^*(\hat{\mathbf{m}}, r, z, \vec{\theta}) \mathcal{C} \hat{\mathbf{p}}(\hat{\mathbf{m}}, r, z, \vec{\theta}), \quad (5.1)$$

where $\vec{\theta} = (\theta_1, \dots, \theta_n)$ is the vector of n known source azimuthal radials. A similar process was employed by Fawcett *et al.* (1996) in their analysis of *Matched-field source localization in a range-dependent environment*.³

It is very difficult to draw any conclusions from the Bartlett statistics along a radial other than a confirmation of a possible source *depth* and *range*. The MF ambiguity surfaces shown in Figures 5.4 to 5.7 represent only a small segment of a greater three-dimensional picture. Nevertheless, it is clear that as the target moves downslope

² $\theta_c = \arccos(c_1/c_2)$; where $c_1 \simeq 1479$ m/s and $c_2 \simeq 1550$ m/s.

³The latter experiment was situated in a deeper water environment (2000 - 2700 m). In their observations of the target at a 5.5 km arc (minor depth changes were encountered) and a known azimuth, they estimated their ranges to be in very good agreement with the true source range. Considering what has been observed in this experiment, such agreements is *not unexpected*. However, if the bathymetry and geoacoustics are inaccurate, the error in MFP calculations will enhance as the sound will travel larger distances. Still, I believe that the error would be less than that in a shallower environment where boundary interactions are more numerous and the sensitivity to geoacoustic properties is also greater.

Table 5.1 Summary of MFP from selected radials.

| Radial | \mathcal{P}_B | True Range [m] | MFP Range [m] | MFP Depth [m] | Range error [m] | Fig. * |
|--------|-----------------|-------------------|------------------|------------------|--------------------|---------------|
| T1819 | 0.868 | 2187 | 2120 | 30 | - 67 | 5.4 |
| T1840 | 0.578 | 5679 | 5520 | 55 | - 159 | 5.5 |
| T1851 | 0.652 | 5522 | 5640 | 70 | + 118 | <i>no Fig</i> |
| T1900 | 0.713 | 5330 | 5440 | 55 | + 110 | 5.6 |
| T1920 | 0.805 | 5226 | 5000 | 40 | - 226 | 5.7 |

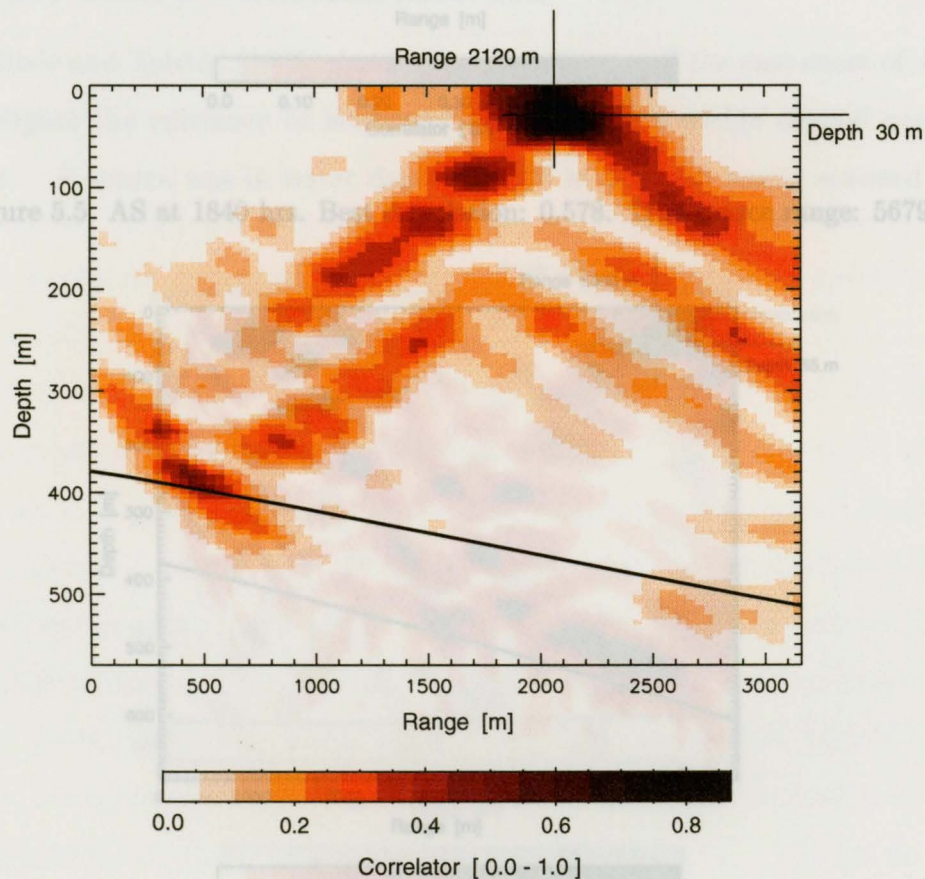


Figure 5.4 Ambiguity Surface (AS) for the data sampled at 1819 hrs. Best correlation: 0.868. True source range: 2187 m.

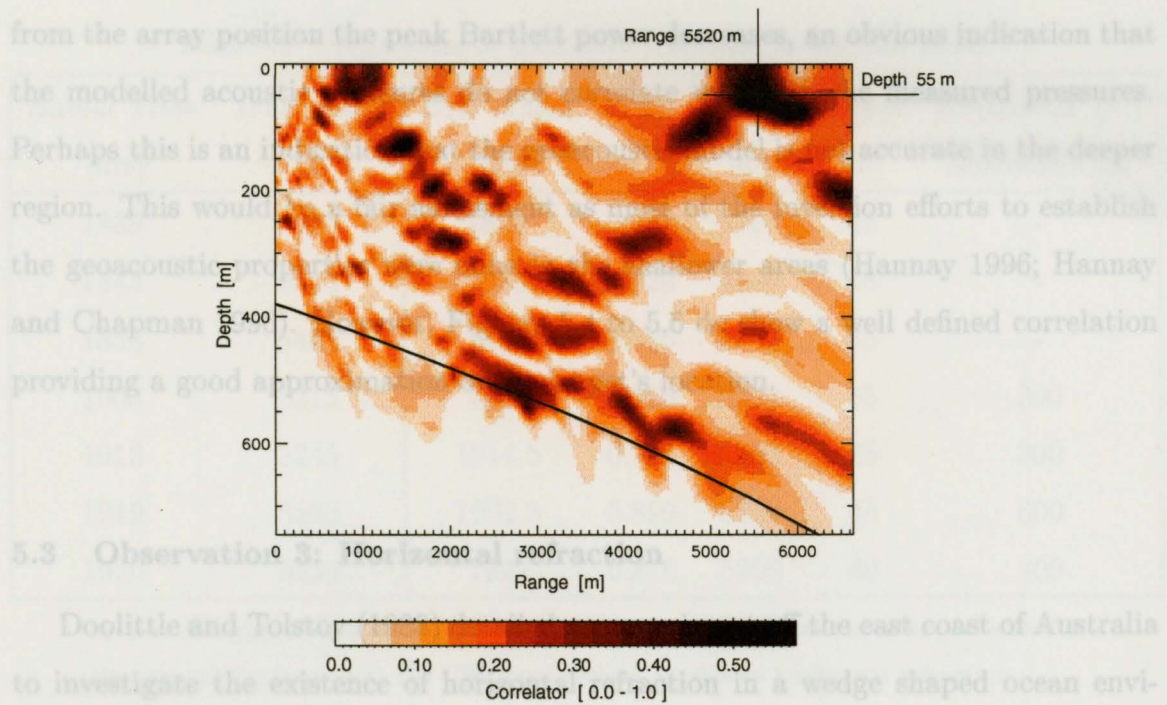


Figure 5.5 AS at 1840 hrs. Best correlation: 0.578. True source range: 5679 m.

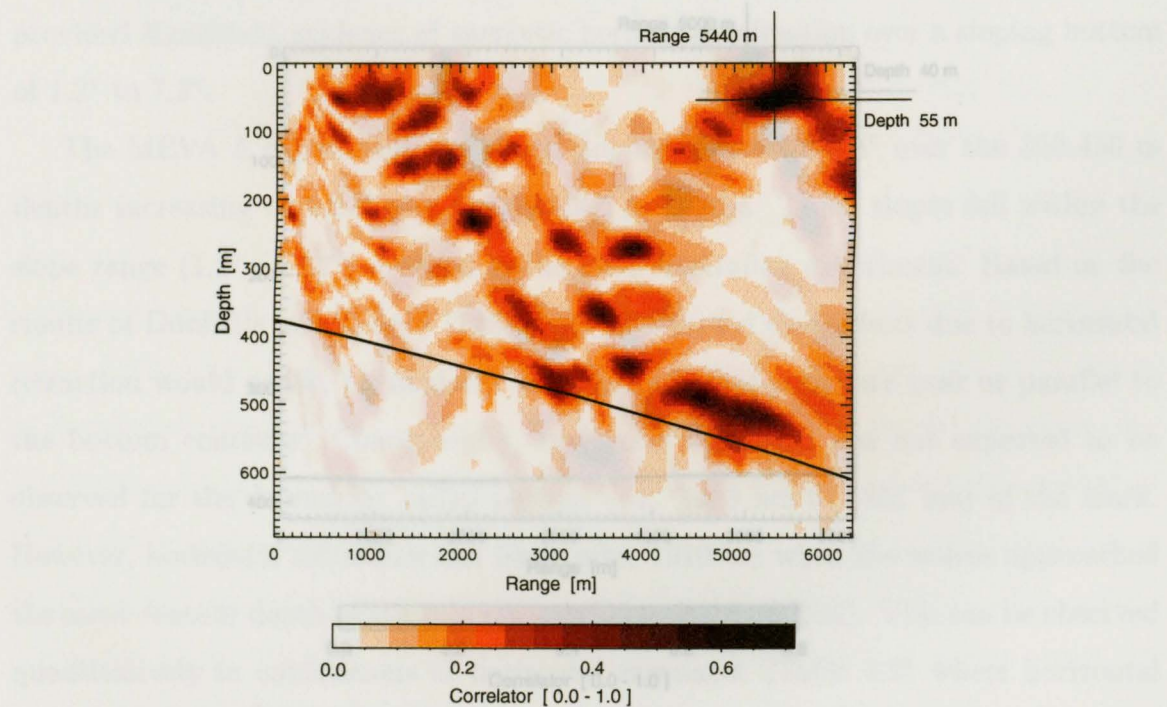


Figure 5.6 AS at 1900 hrs. Best correlation: 0.713. True source range: 5330 m.

from the array position the peak Bartlett power decreases, an obvious indication that the modelled acoustic pressures do not correlate well with the measured pressures. Perhaps this is an indication that the geoacoustic model is not accurate in the deeper region. This would be a fair assessment as most of the inversion efforts to establish the geoacoustic properties were done in the shallower areas (Hannay 1996; Hannay and Chapman 1996). However, Figures 5.4 to 5.6 do show a well defined correlation providing a good approximation of the target's location.

5.3 Observation 3: Horizontal refraction

Doolittle and Tolstoy (1988) detailed an experiment off the east coast of Australia to investigate the existence of horizontal refraction in a wedge shaped ocean environment. A source was in water depths of 500 m and was towed seaward towards

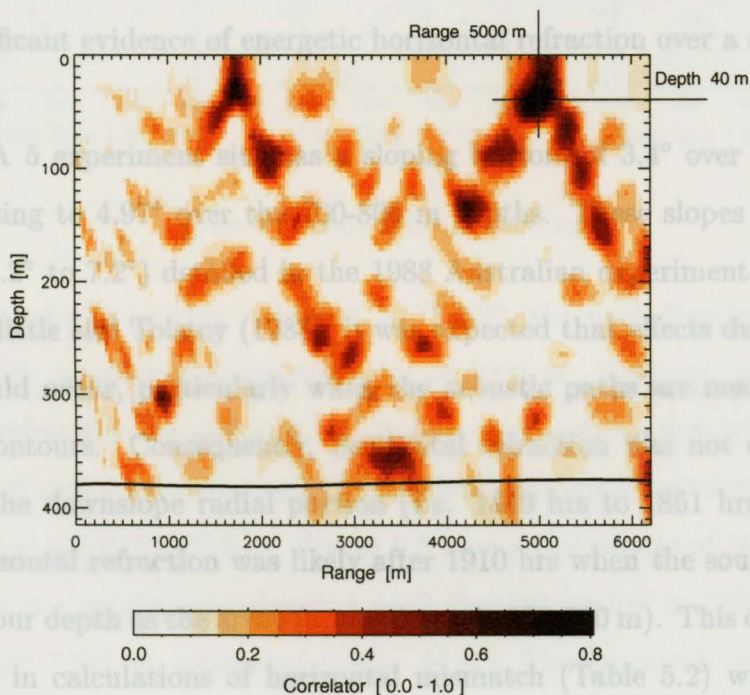


Figure 5.7 MFP at 1920 hrs. Best correlation: 0.805. True source range: 5226 m.

Table 5.2 Occurrences of horizontal refraction at selected times.

| <i>Radial Time</i> [hrs] | <i>True Range</i> [m] | <i>Best Match</i> [hrs] | \mathcal{P}_B | <i>Range</i> [m] | <i>Depth</i> [m] | <i>Horizontal (1.)</i> <i>Mismatch</i> [m] |
|-----------------------------|--------------------------|----------------------------|-----------------|---------------------|---------------------|---|
| 1839 | 5584 | 1839 | 0.637 | 5760 | 45 | - |
| 1843 | 5693 | 1843 | 0.626 | 5880 | 35 | - |
| 1853 | 5444 | 1853 | 0.655 | 5960 | 65 | - |
| 1903 | 5315 | 1904 | 0.750 | 5520 | 55 | 200 |
| 1913 | 5245 | 1914.5 | 0.724 | 5200 | 45 | 300 |
| 1919 | 5233 | 1922.5 | 0.899 | 5320 | 45 | 600 |
| 1920 | 5226 | 1922 | 0.876 | 5200 | 40 | 400 |

1. The *Horizontal Mismatch* is the estimated range away from the expected position (horizontal displacement) the CW tonal arrived at, due to horizontal refraction.

greater depths. The conditions were similar to the present experiment and the results provided significant evidence of energetic horizontal refraction over a sloping bottom of 1.2° to 7.2° .

The MEVA 5 experiment site has a sloping bottom of 3.4° over the 350-450 m depths increasing to 4.97° over the 700-800 m depths. These slopes fall within the slope range (1.2° to 7.2°) detailed in the 1988 Australian experiment. Based on the results of Doolittle and Tolstoy (1988), it was expected that effects due to horizontal refraction would occur, particularly when the acoustic paths are near or parallel to the bottom contours. Consequently, horizontal refraction was not expected to be observed for the downslope radial portion (*i.e.* 1819 hrs to 1851 hrs) of the track. However, horizontal refraction was likely after 1910 hrs when the source approached the same contour depth as the array (approximately 380-390 m). This can be observed quantitatively in calculations of horizontal mismatch (Table 5.2) where horizontal refraction begins to occur at approximately 1900 hrs. The mis-location occurs, each time, several hundred yards to the right of the expected location of the target.

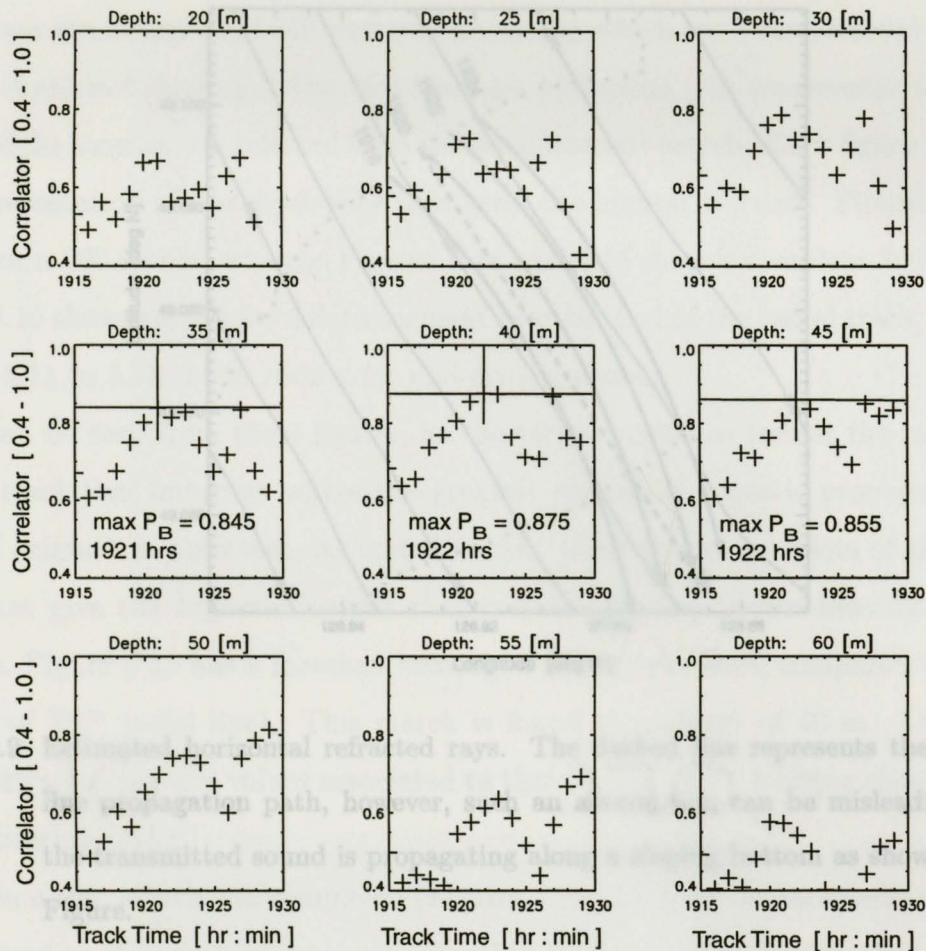


Figure 5.8 Multi-plot at 1920 hrs.

Assuming that the bearing is known, at T1920, the peak Bartlett is calculated to be 0.805 with an estimated source range of 5000 m. However, since the effects of horizontal refraction are strongest for the source positions around this time, the T1920 modelled radial was subsequently matched with measured signals received at times before and after T1920 hrs. Figure 5.8 shows the results of this examination for different source depths, and clearly a peak Bartlett occurs at 1922 (P_B : 0.876; estimated range: 5200 m; estimated depth: 40 m). The mismatch occurs about 400 m toward the shallower depths, as expected for horizontal refraction.⁴

⁴To ensure that the mismatch was not due to an error in clock discrepancy, synchronization in

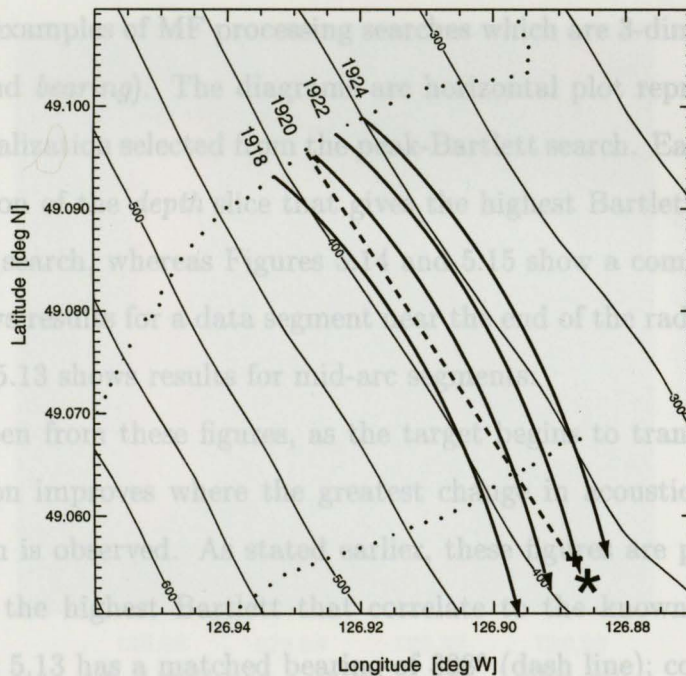


Figure 5.9 Estimated horizontal refracted rays. The dashed line represents the straight line propagation path, however, such an assumption can be misleading when the transmitted sound is propagating along a sloping bottom as shown in this Figure.

Figure 5.9 shows qualitatively possible refracted rays that may account for the mis-match observed at T1920. In addition, Table 5.2 provides a summary of MF localization that accounts for occurrences of horizontal refraction.

5.4 Observation 4: Matched-field localization - source azimuth unknown

The following figures show a complete search of the matched-field parameters, computed in accordance with Equation (5.2),

$$\mathcal{P}_B(\hat{\mathbf{m}}, r, z, \theta |_{360}^0) = \hat{\mathbf{p}}^*(\hat{\mathbf{m}}, r, z, \theta |_{360}^0) \subseteq \hat{\mathbf{p}}(\hat{\mathbf{m}}, r, z, \theta |_{360}^0). \quad (5.2)$$

timing was checked between all units, GPS beacons and recorders, log books, data sheets and tapes.

The figures are examples of MF processing searches which are 3-dimensional searches (*range, depth and bearing*). The diagrams are horizontal plot representations (map views) of the localization selected from the peak-Bartlett search. Each figure (or plot) is a representation of the *depth* slice that gives the highest Bartlett. Figures 5.10 to 5.13 show a 20° search, whereas Figures 5.14 and 5.15 show a complete 360° search. Figure 5.10 shows results for a data segment near the end of the radial track, whereas Figures 5.11 to 5.13 shows results for mid-arc segments.

As can be seen from these figures, as the target begins to transit the region the *bearing* resolution improves where the greatest change in acoustic propagation per angle of azimuth is observed. As stated earlier, these figures are plots of the depth slices that give the highest Bartlett that correlate to the known bearing.⁵ For example, Figure 5.13 has a matched bearing of 328° (dash line); compared to a true bearing of 327° (solid line). This match is found at a depth of 40 m. The range and depth estimates are values associated to that highest MFP bearing closest to the known bearing (MFB).

When a 360° search was completed (Figures 5.14 and 5.15), a characteristic feature was noticed to the south of the array. Another strong Bartlett localization occurred in an ambiguous *mirrored* position from the one along the target track. Of course, after a close examination of the entire bathymetric region this feature would be expected as the bottom contours do continue for some distance symmetrically about the array position (north-south contours). However, the matched-field algorithm selected the bearing that correlated best with the actual target position, accounting for the bathymetry and geoacoustics.

Another feature seen in the localizations, particularly those from 1900 hrs on, are the long peak-Bartlett *streaks*. Much like the bathymetric mismatch described in section 3.2.1 (item 1. & Figure 3.5), the relationship between the range estimates

⁵In the following figures (5.10 to 5.15) the dash line indicates the estimated bearing and the solid line indicates the true known bearing.

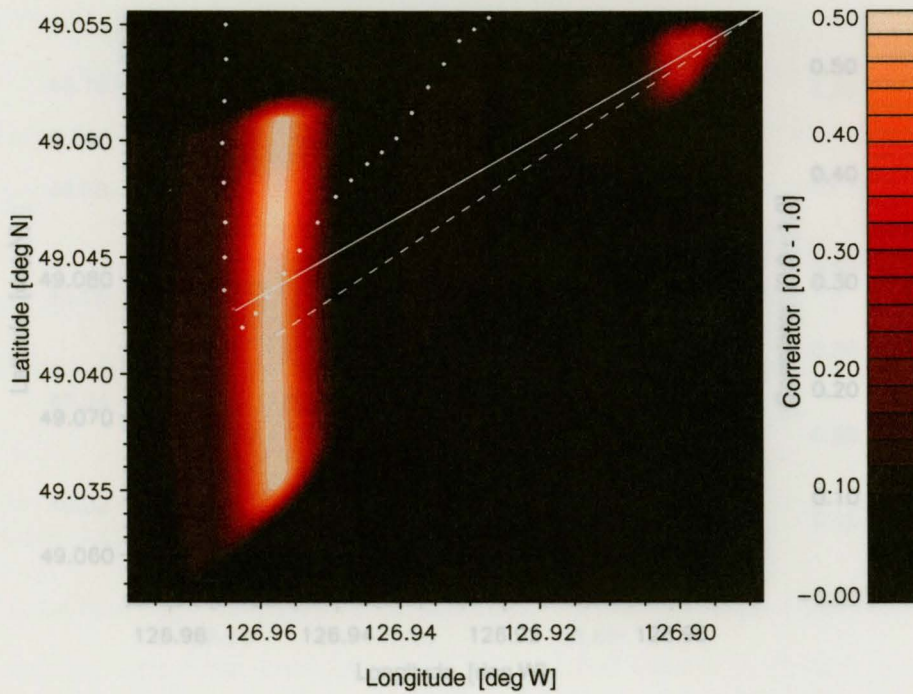


Figure 5.10 T1840 hrs (20° search arc). Best depth: 45 m. True: 255° ; MFB: 253° .

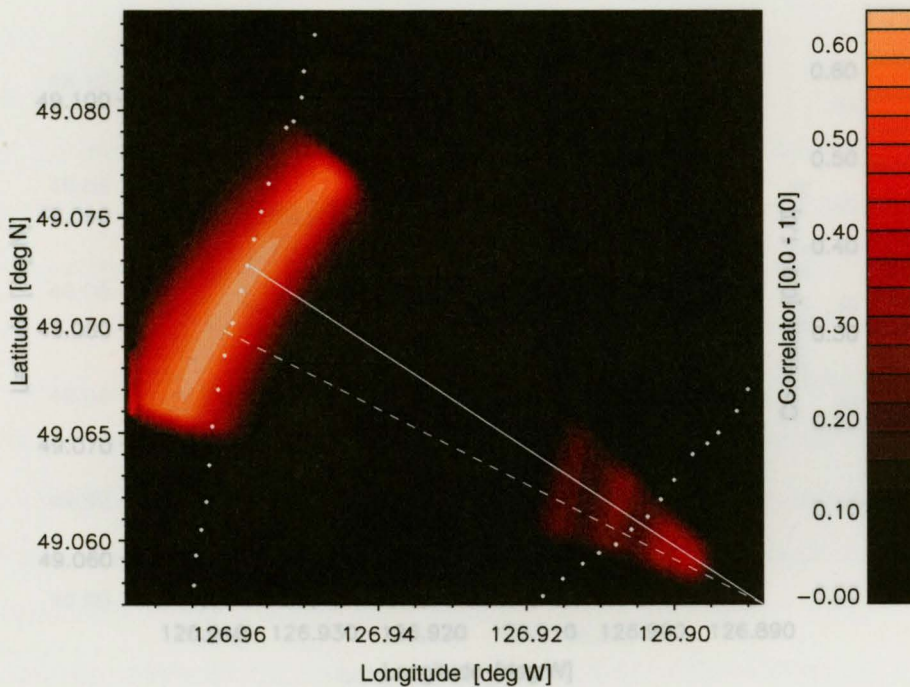


Figure 5.11 T1900 hrs (20° search arc). Best depth: 55 m. True: 289° ; MFB: 285° .

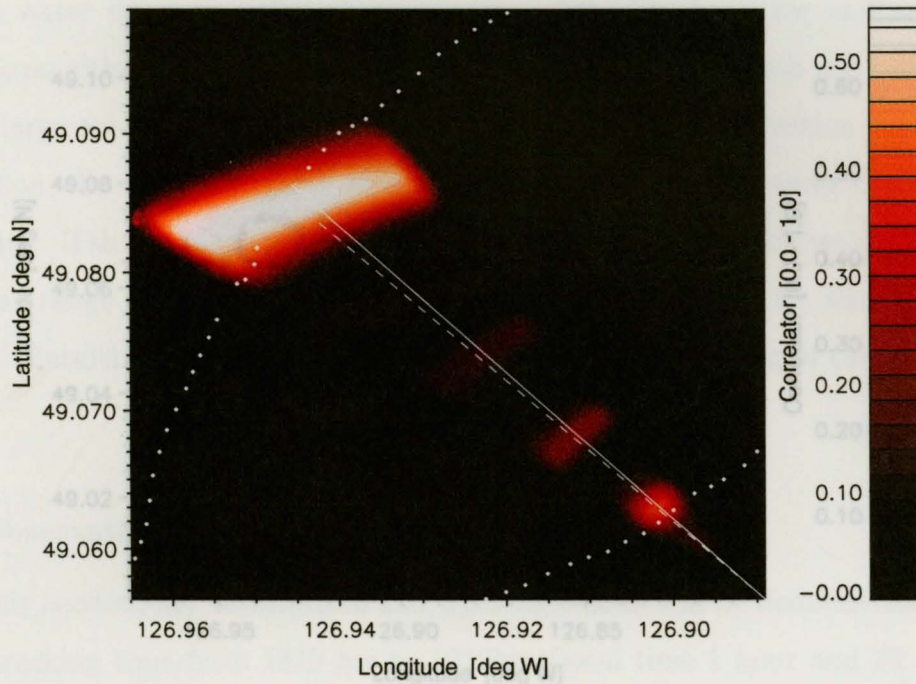


Figure 5.12 T1910 hrs (20° search arc). Best depth: 50 m. True: 309° ; MFB: 308° .

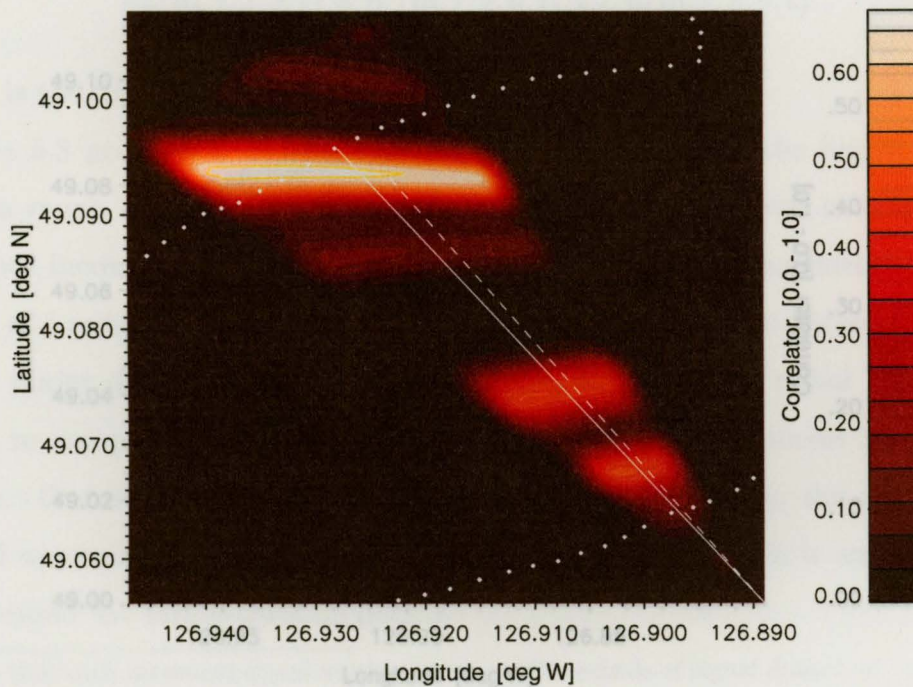


Figure 5.13 T1920 hrs (20° search arc). Best depth: 40 m. True: 327° ; MFB: 328° .

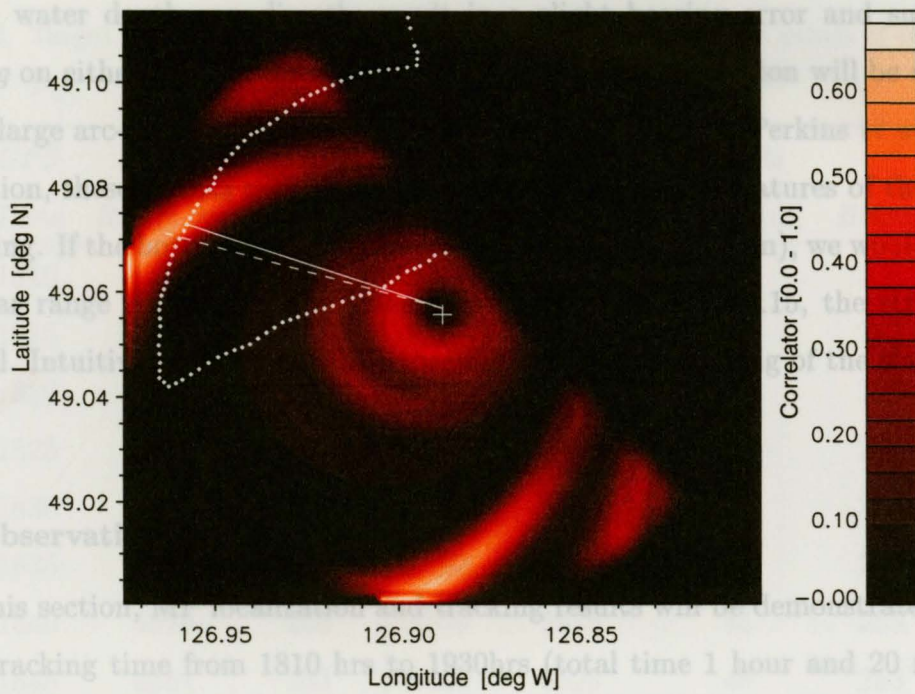


Figure 5.14 T1900 hrs (360° search arc). Best depth: 55 m. True: 289°; MFB: 285°.

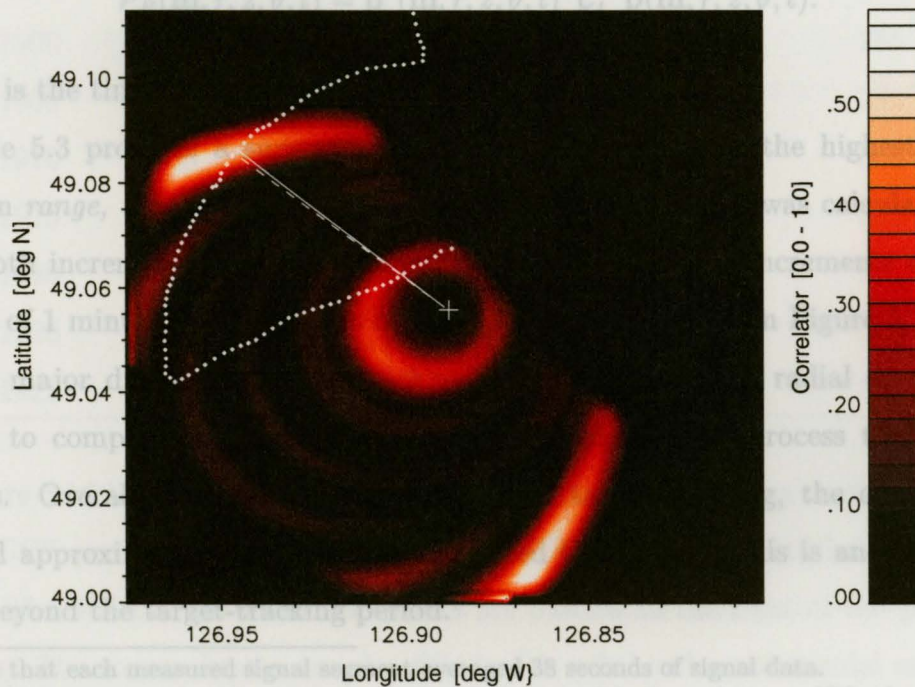


Figure 5.15 T1910 hrs (360° search arc). Best depth: 50 m. True: 309°; MFB: 308°.

and the water depth can directly result in a slight bearing error and subsequent *streaking* on either bearing directions from the true source position will be observed. Similar large arc-shaped ambiguities were observed by John S. Perkins *et al.* (1996). In addition, these *streaks* may be explained by the geometric features of the bottom contouring. If the bottom was range-independent (i.e., flat bottom), we would observe a circular range ring. However, as seen in Figures 5.14 and 5.15, the streaking is elliptical. Intuitively, this would be expected from the contouring of the slope.

5.5 Observation 5: Tracking results

In this section, MF localization and tracking results will be demonstrated for the target tracking time from 1810 hrs to 1930hrs (total time 1 hour and 20 minutes). The following expression was used for this portion of the tracking (Equation 3.8):

$$\mathcal{P}_B(\hat{\mathbf{m}}, r, z, \theta, t) = \hat{\mathbf{p}}^*(\hat{\mathbf{m}}, r, z, \theta, t) \mathcal{C}_t \hat{\mathbf{p}}(\hat{\mathbf{m}}, r, z, \theta, t).$$

where t is the time of the measured signals from the target.

Table 5.3 provides a summary of the tracking results for the highest Bartlett values in *range*, *depth* and *bearing* for each time t . The search was calculated using 5 m depth increments, 40 m range increments; 1 deg bearing increments and at an interval of 1 minute.⁶ The results of Table 5.3 are also shown in Figure 5.18.

The major drawback to this tracking is that it took each radial direction 20-30 secs to compute. In an arc of investigation of 20°, the process took 6 to 13 minutes. Overall, for the entire 80 minutes of target tracking, the computations required approximately 13.5 hours of dedicated CPU time. This is an excess of 12 hours beyond the target-tracking period.⁷

⁶Note that each measured signal segment averaged 38 seconds of signal data.

⁷I was not concerned with the computational time, as I believe that my IDL algorithms are not coded *efficiently* to compute the large matrices and mathematical expressions. In addition, within the last 5 years CPU capabilities have enhanced the abilities to accomplish these very large

Table 5.3 Target Tracking Summary - 1810 hrs to 1930 hrs (selected values of the highest \mathcal{P}_B).

| <i>GPS</i> | | <i>Locater</i> | | <i>MFP</i> | | <i>Results</i> | |
|-------------|------------------|----------------|-----------------|------------------|------------------|----------------|--|
| <i>Time</i> | <i>Range [m]</i> | <i>Bearing</i> | \mathcal{P}_B | <i>Range [m]</i> | <i>Depth [m]</i> | <i>Bearing</i> | |
| 1810 | 1230 | 330° | 0.882 | 1175 | 45 | 336° | |
| 1815 | 1470 | 288° | 0.821 | 1900 | 69 | 283° | |
| 1820 | 2354 | 273° | 0.859 | 2050 | 30 | 280° | |
| 1825 | 3137 | 267° | 0.798 | 2925 | 41 | 276° | |
| 1830 | 4033 | 260° | 0.781 | 4100 | 33 | 252° | |
| 1835 | 4983 | 256° | 0.772 | 5025 | 30 | 247° | |
| 1840 | 5679 | 255° | 0.529 | 5375 | 45 | 253° | |
| 1845 | 5651 | 263° | 0.459 | 5525 | 40 | 253° | |
| 1850 | 5540 | 272° | 0.585 | 5700 | 70 | 266° | |
| 1855 | 5459 | 281° | 0.716 | 5850 | 55 | 279° | |
| 1900 | 5330 | 289° | 0.674 | 5550 | 55 | 285° | |
| 1905 | 5238 | 299° | 0.687 | 5775 | 51 | 293° | |
| 1910 | 5303 | 309° | 0.575 | 5175 | 50 | 308° | |
| 1915 | 5139 | 317° | 0.665 | 5200 | 40 | 312° | |
| 1920 | 5226 | 327° | 0.784 | 5425 | 39 | 328° | |
| 1925 | 5245 | 338° | 0.725 | 5525 | 32 | 333° | |
| 1929 | 5196 | 346° | 0.886 | 5000 | 35 | 346° | |

Figure 5.16 is a representation in greater detail of the tracking results in relation to the GPS position of the tow vessel, CSS RICKER, from 1810 hrs to 1930 hrs (dots). The MF calculated source depths are plotted to the right of the geographic tracking. The source depths are also fitted with a 3rd order polynomial as a means

computations in less time than ever before. I anticipate that the CPU excesses seen here will decrease as even greater computer capabilities and technologies are progressed.

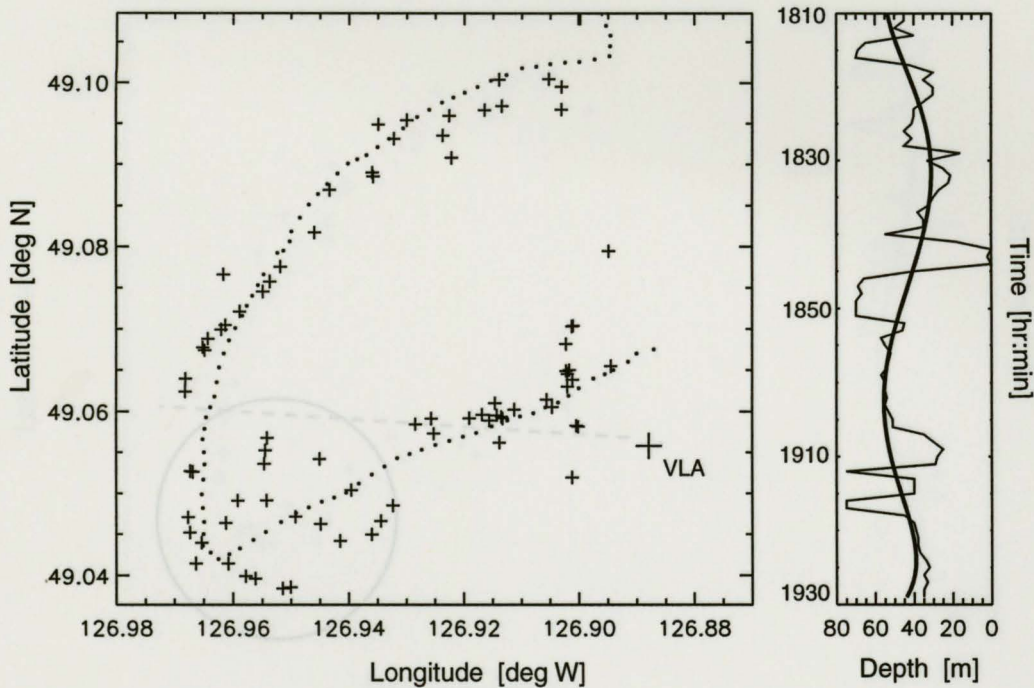


Figure 5.16 Geographic and source depth tracking from highest *Bartlett correlator* results.

crepancies. Area below the dash lines are slope regions of $3-5^\circ$ and above the to assess the probable source depths during the tracking period. As seen from the depth variations, the target estimates fell deeper between 1840 hrs and 1850 hrs. This can be attributed to the decrease in speed from the tow vessel as it altered course to starboard and also due to the northwest currents that may have pushed the towed source deeper. (section 2.5).

Poor performance near the course alteration ($\sim 1830-1850$ hrs) may be due to modelling errors in the use of OAR (see circled area of Figure 5.17); for these times the slopes along the propagation paths are $3-5^\circ$, shown in the area below the dash line. For other times, i.e. before 1820 hrs and after 1850 hrs, the effective slopes are less than 2° . The gentler slopes show that the adiabatic approximation is producing reasonable results. Another explanation can be argued that due to the steep, or nearly direct, upslope propagation at times near the course alteration (~ 1840 hrs) the OAR model was not able to discriminate between different propagation bearings

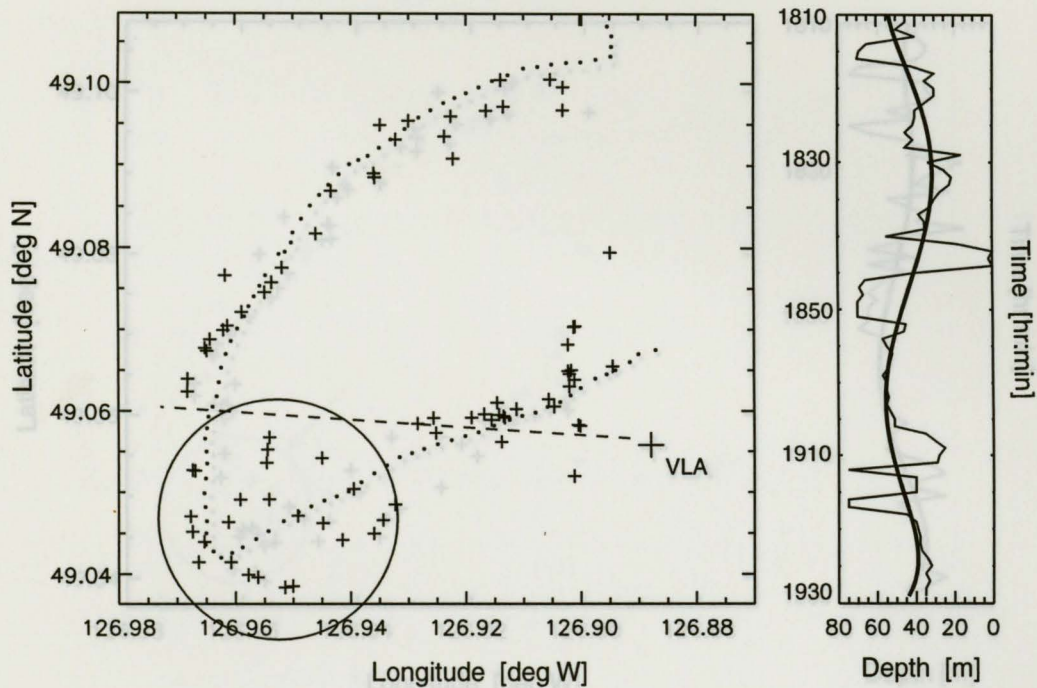


Figure 5.17 Target tracking from highest *Bartlett correlator* results showing areas of discrepancies. Area below the dash lines are slope regions of $3 - 5^\circ$ and above the dash lines are slope regions of 2°

Finally, the tracking of the highest correlation (peak-Bartlett) along the true bearing. This representation serves three purposes: First, as the model produced wildly varying bearing results. This can be validated by the poor results of slopes greater than 3° shown in the validation ASA benchmark comparison (section 2.5).

As a means to investigate further the tracking potential of the \mathcal{P}_B -resultant matrix, Figure 5.18 shows tracking results that were selected, for a particular time, as the best estimates of the true source position (these values are shown in Table 5.3). The criterion used was a localization of highest best Bartlett power (\mathcal{P}_B) which was closest in depth and bearing to the true source position. A similar polynomial fit to the source depths was computed, again showing a similar source depth movement over the tracking period.

Figure 5.20 shows peak-Bartlett fluctuations of the results. A Gaussian fitted

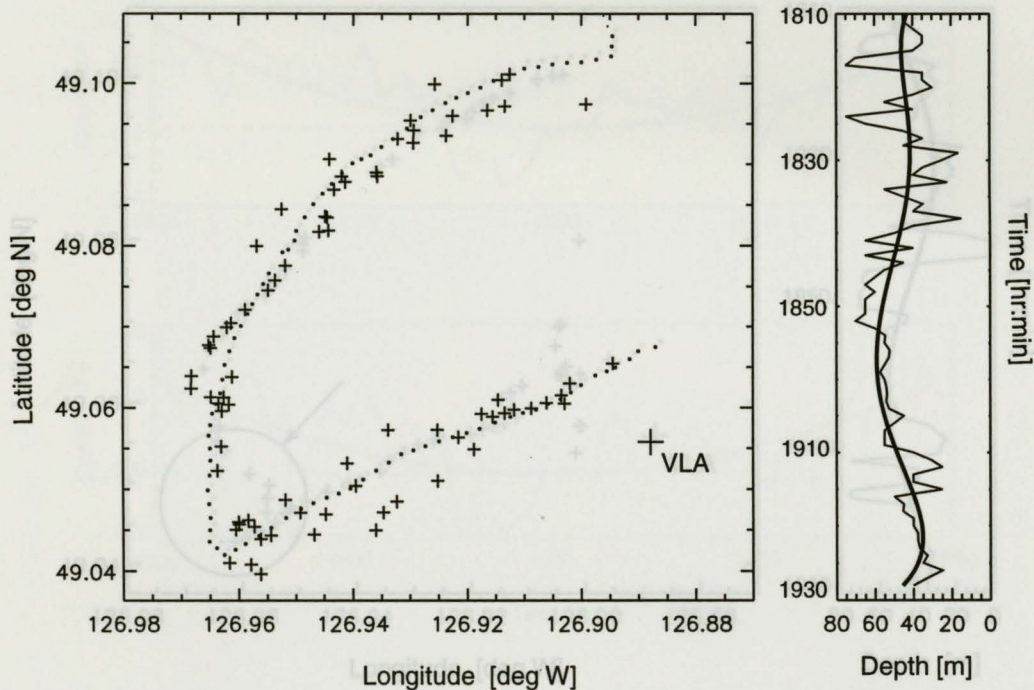


Figure 5.18 Geographic and source depth tracking from best *depth and bearing* results.

Finally, Figure 5.19 demonstrates target tracking of the highest correlation (peak-Bartlett) along the true bearing. This representation serves three purposes: First, it shows that within the \mathcal{P}_B -resultant matrix there exists a solution that can track the target with a small measure of error; Second, within this matrix, there exists a well-defined range estimate for each line of bearing (or bearing streak); Third, at the alteration (1840 hrs) the reader can see a definite mismatch in range for about 5-8 minutes. The range mismatch would suggest that perhaps the geoacoustic parameters and/or bathymetric data are incorrect for that small area (see circled area in Figure 5.19). There may be a significant local change in the geoacoustic properties that may result in poor MFP estimations. Alternately, the signal from the altering target (and the tow vessel) may have created a confusing propagating wave that cannot be accommodated using this form of matched-field processing.

Figure 5.20 shows peak-Bartlett fluctuations of the results. A Gaussian fitted

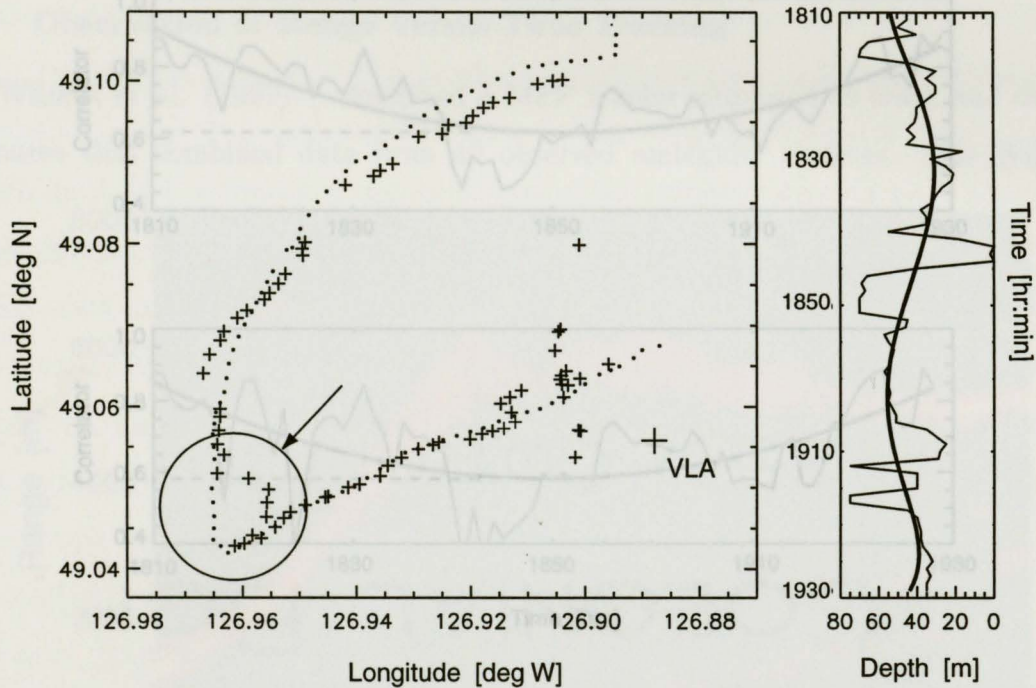


Figure 5.19 Geographic and source depth tracking from peak-Bartlett with known bearing. The circled area is a region of mismatch most likely produced by poorly constrained geoacoustic Bartlett correlation along the true bearing plotted as Range Vs Time properties.

curve allows the reader to see the MF trend over the tracking period. In general, the Bartlett peak values obtained for the data in Figure 5.19 were approximately 0.02 - 0.05 lower than the peak values of Figure 5.16. These are Peak-Bartlett fluctuation as a function of time. The top Figure shows the MF values corresponding to Figure 5.16 and the bottom Figure shows the MF values corresponding to Figure 5.19. The standard deviation is 0.073 for the top chart and 0.103 for the bottom chart.

The importance of this diagram is to show that there is little compromise in Bartlett powers by choosing estimated target position values that are close the actual target position. Furthermore, in an experiment similar to MEVA 5, Fawcett *et al.* (1996) qualified that generally the poor estimates in range correspond to power values

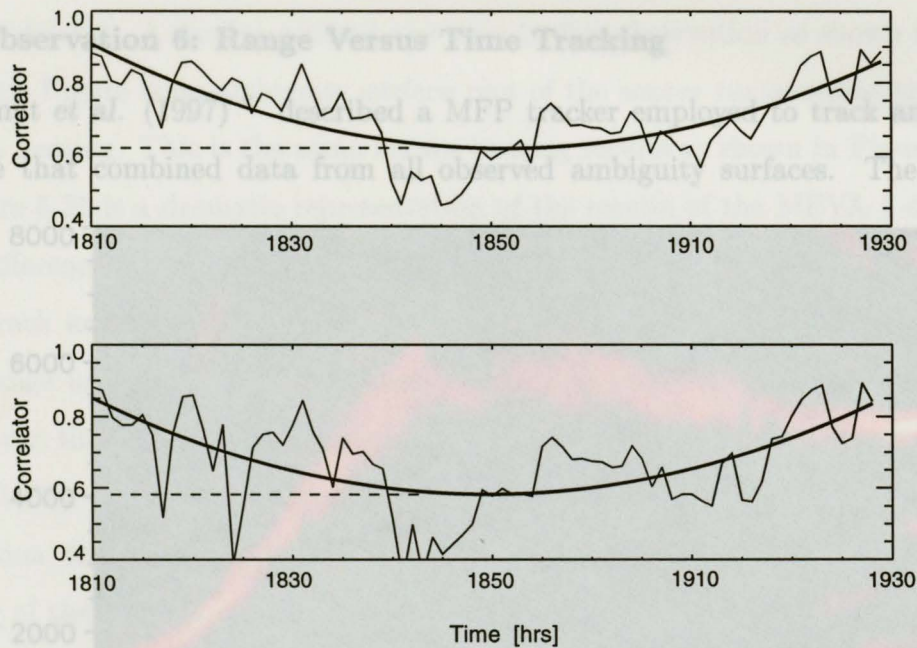


Figure 5.20 Peak-Bartlett fluctuation as a function of time. Top fig: MF corresponding to fig. 5.16. Bottom fig: MF corresponding to fig. 5.19

below 0.5 which relate directly to poor signal-to-noise ratios (SNR). In addition, they indicated that this mismatch is likely associated in part to the geoacoustic parameters used and other factors as array depth, tilt and signal time averaging.

With respect to this experiment, it is reasonable to conclude that all of these factors, in spite of the processor's robustness, could very well contribute to the lower Bartlett value, particularly at the alteration of course (T1840 hrs) when the actual position of the source did not follow the exact course of the tow vessel. The source (target) would have a tendency to sink as the tow vessel slowed at the alteration. This resulted in aspect changes and incorrect positioning of the target which transmitted an unexpected confused signal and subsequent MF mismatch. The trough seen in Figure 5.20 (approximately T1840-T1850 hrs) coincides with the poor range and bearing resolution seen in the previous Figures (5.16 to 5.19).

*Similar papers were published that dealt with Matched-Field Linear Trackers such as Wilmut et al. (1993), Wilmut et al. (1995) and Ozard et al. (1996).

5.6 Observation 6: Range Versus Time Tracking

Wilmut *et al.* (1997)⁸ described a MFP tracker employed to track and detect a source that combined data from all observed ambiguity surfaces. The Wilmut

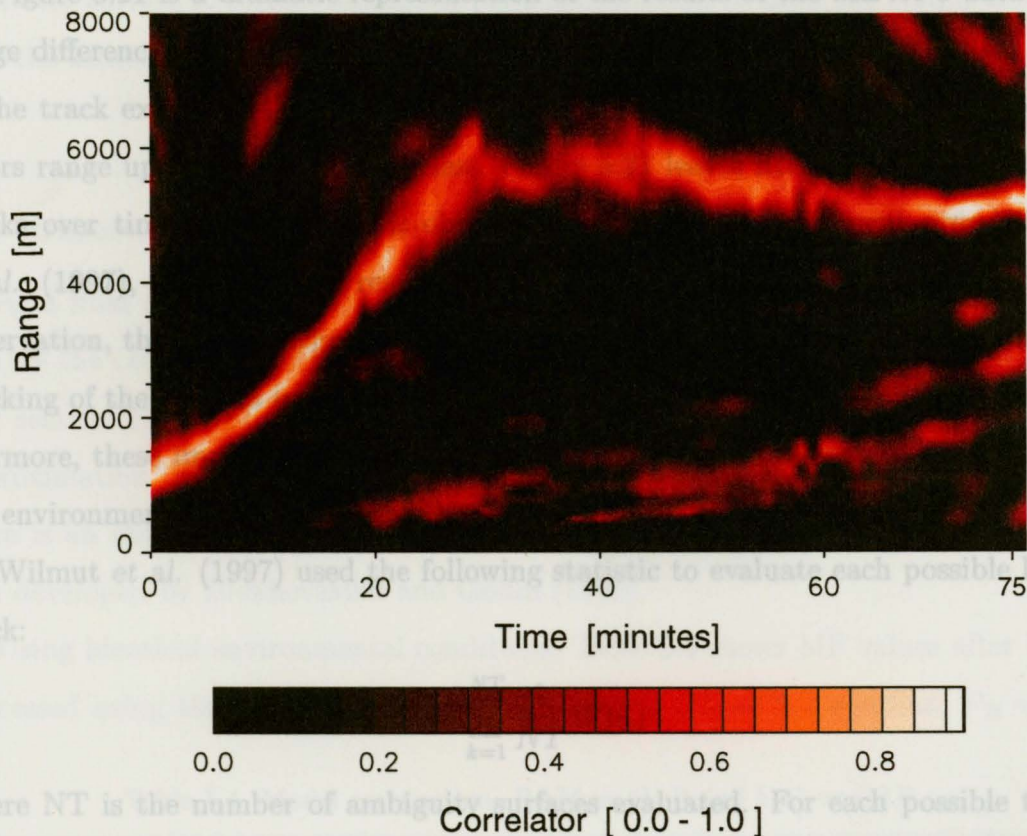


Figure 5.21 Highest Bartlett correlation along the true bearing plotted as Range Vs Time.

Time 0 minutes equates to T1810 hrs. This Figure shows surface to surface tracking. The range differences between GPS and tracking estimates were less than 100 m. Errors range up to 250 m at the course alteration T1840-T1850 (30 to 40 min on the plot).

philosophy was to detect the target after the tracking algorithm was used while the target moved linearly at a constant speed, and in an environment of higher SNR and

⁸Similar papers were published that dealt with *Matched-Field Linear Trackers* such as Wilmut *et al.* (1993), Wilmut *et al.* (1995) and Ozard *et al.* (1996).

greater sidelobes. A similar method was used in this observation as shown in Figure 5.21. This Figure is an ambiguity surface plot of the source range versus time along a known bearing. This is the same known bearing results as shown in Figure 5.19.

Figure 5.21 is a dramatic representation of the results of the MEVA 5 data with range differences between the GPS and tracking estimates less than 100 m for most of the track except at the course alteration (T1840-T1850 or 30-40 min) where the errors range up to 250 m. Nonetheless, Figure 5.21 leaves little doubt of the target tracks over time. Although, this observation shows an improvement over Wilmut *et al.* (1997), these tracking results reflect a different tracking philosophy. In this observation, the strong target SNR (Figures 4.9 and 4.10) allowed surface-to-surface tracking of the changes in target course headings and changes in source depths. Furthermore, these improvements come as a direct result of the symmetry breaking for the environment of the VLA in MEVA 5.

Wilmut *et al.* (1997) used the following statistic to evaluate each possible linear track:

$$T = \sum_{k=1}^{NT} \frac{1}{NT} B(p_k) \quad (5.3)$$

where NT is the number of ambiguity surfaces evaluated. For each possible track, statistic T from Equation (5.3) sums the Bartlett output power over the NT times. The $B(p_k)$ is the Bartlett statistic at position p_k nearest to the track at time k that is constrained to realistic speeds of the source. Furthermore, Wilmut *et al.* (1997) estimated the track signal-to-noise output as follows:

$$SNR = \frac{T - \bar{x}}{s} \sqrt{NT} \quad (5.4)$$

where \bar{x} is the average value of the Bartlett statistic for all points on all ambiguity surfaces, and s is the standard deviation of the Bartlett statistic for all points on all ambiguity surfaces.

The breaking symmetry of the MEVA 5 data acted as the SNR evaluator reducing

(5.3) to $NT = 1$ and

$$T(k) = B(p_k) \quad (5.5)$$

where the surface to surface ambiguity plots are sufficient to show the unique tracking over the azimuthally dependent environment.

5.7 Observation 7: Model Comparisons

As a final observation, this section demonstrates the improvements (or degradation) of the OAR model compared to another suitable candidate model such as RAM (see section 2.3.1). In addition, the amplitude correction applied to the adiabatic approximation from the *ad hoc* solution is also demonstrated to show that in fact there is an improvement in the replicated environment as calculated by the correction developed by Brekhovskikh and Godin (1993).

Using identical environmental conditions, Table 5.4 shows MF values after being processed using the different models: Compared to the *ad hoc* solution, \mathcal{P}_B values

Table 5.4 Model comparison. RAM vs OAR (*ad hoc*) vs OAR

| Time | Range | RAM | | | <i>ad hoc</i> | | | OAR | | |
|------|-------|-----------------|-------|-----|-----------------|-------|-----|-----------------|-------|-----|
| | | \mathcal{P}_B | R_g | Dep | \mathcal{P}_B | R_g | Dep | \mathcal{P}_B | R_g | Dep |
| 1813 | 1289 | 0.857 | 1194 | 35 | 0.789 | 1350 | 40 | 0.808 | 1320 | 40 |
| 1823 | 2846 | 0.877 | 2697 | 45 | 0.805 | 2760 | 45 | 0.810 | 2760 | 40 |
| 1827 | 3510 | 0.821 | 3335 | 40 | 0.762 | 3575 | 45 | 0.792 | 3480 | 40 |
| 1833 | 3137 | 0.790 | 4468 | 40 | 0.704 | 4760 | 30 | 0.680 | 4760 | 30 |
| 1835 | 4560 | 0.745 | 4986 | 60 | 0.730 | 5175 | 45 | 0.772 | 5025 | 30 |
| 1839 | 5584 | 0.637 | 5760 | 45 | 0.626 | 6050 | 35 | 0.720 | 5880 | 50 |
| 1843 | 5693 | 0.593 | 5594 | 45 | 0.616 | 5880 | 35 | 0.693 | 6040 | 40 |

for the OAR model are approximately 0.05 larger along the short propagation radials and up to 0.1 along the longer radials. This is evidence that the *ad hoc* solution does not accommodate well any accumulated amplitude errors. The RAM model shows better results, again along the shorter radials but the MF values are degraded as the radial propagation gets longer and perhaps confused with the target course alteration at 1840 hrs. One major advantage of the OAR relative to the RAM model was that it took RAM an extra 10-12 seconds of CPU time to compute the MF value for each ambiguity surface. This equates to an additional 6 hours longer than OAR for the entire tracking of the source (in *range, depth and bearing*).

large errors would occur in target localization and tracking.

However, in this *littoral* environment, a complete knowledge and understanding of the bathymetry, geoacoustic and water column properties provided a powerful tool that exploited all the parameters needed to produce accurate and reliable target localization. Small errors and inaccuracies had minor effects on the very robust linear Bartlett processor. The robustness of the processor is at the expense of resolution, poor source depth localization and the presence of sidelobes (Tolstoy 1993), as seen in the observations of chapter 5.

6.1 Acoustic Modelling

Echoing the sentiments expressed by Fawcett, Jeremy and Chapman (1996), the implementation of the *adiabatic* normal mode model (OAR) proved to be painstaking and labourious when producing the lookup tables. Careful analysis of the propagation modes required wavenumber corrections within each lookup table. Once collected, the tables (including eigen-function, eigen-values and bathymetric tables) provided a set of environmental data that described well the target region and allowed fast and efficient calculations (i.e. approximately 10 secs to calculate a 2-D field along a known

Chapter 6

Conclusion

The most prominent result of this thesis, serving as a note of caution, is the great dependence on a thorough knowledge of the environment required to produce the desired tracking. In the absence of a complete knowledge of this environment, particularly in a *non isotropic* setting such as a continental slope, large errors would occur in target localization and tracking.

However, in this *littoral* environment, a complete knowledge and understanding of the bathymetry, geoacoustic and water column properties provided a powerful tool that exploited all the parameters needed to produce accurate and reliable target localization. Small errors and inaccuracies had minor effects on the very robust linear Bartlett processor. The robustness of the processor is at the expense of resolution, poor source depth localization and the presence of sidelobes (Tolstoy 1993), as seen in the observations of chapter 5.

6.1 Acoustic Modelling

Echoing the sentiments expressed by Fawcett, Jeremy and Chapman (1996), the implementation of the *adiabatic* normal mode model (OAR) proved to be painstaking and labourious when producing the lookup tables. Careful analysis of the propagation modes required wavenumber corrections within each lookup table. Once collected, the tables (including eigen-function, eigen-values and bathymetric tables) provided a set of environmental data that described well the target region and allowed fast and efficient calculations (i.e. approximately 10 secs to calculate a 2-D field along a known

line of bearing). However, the model comparisons (Observation 7: RAM model versus OAR model) showed that a parabolic equation code (i.e., RAM) could also be used to compile data directly at the latitudinal and longitudinal measured fields. The RAM model (non-elastic parabolic equation) provided reliable and comparatively similar MF values to the OAR model. No doubt, a parabolic equation that included elastic properties could perform the rigorous calculations without having to include modal lookup tables.

6.1.1 Adiabatic Reciprocity

An important implementation in the modelling was the complex pressure field equation for reciprocity of an adiabatic approximation,

$$p(r, z) \simeq \frac{\sqrt{2\pi}}{\rho(z_s)} e^{i\pi/4} \sum_{m=1}^{\infty} \Psi_m(z_s) \Psi_m(r, z) \frac{e^{i \int_0^r k_{rm}(r') dr'}}{\sqrt{k_{rm}(r) k_{rm}(r_s) \int_0^r \frac{dr'}{k_{rm}(r')}}}. \quad (6.1)$$

This expression is an improvement over the *ad hoc* solution (Jensen *et al.* 1994). Equation (6.1) incorporates an amplitude-corrected solution by Brekhovskikh and Godin (1993) that is supported by rigorous mathematical justification. Many publications and papers use the *ad hoc* expression that is appropriately derived as a solution in the WKB approximation, but, the Brekhovskikh-Godin expression is correct and requires minimal effort to code without increasing CPU time when compiled. Furthermore, this thesis demonstrates that the Brekhovskikh-Godin expression is supported by the localization results and show improved \mathcal{P}_B values by as much as 0.1 for longer propagation ranges (Table 5.4).

6.1.2 Horizontal Refraction

In a range dependent waveguide, particularly on a steep slope, the problem of modelling the environment correctly is a measured difficulty. In 1965, Pierce acknowledged

horizontal ray path propagation and more recently, discussions and evaluations of horizontal ray theory were extensively explained in Brekhovskikh and Godin (1992). Only in the 1988 Australian experiment by Doolittle and Tolstoy was horizontal refraction quantifiably shown to be a significant contributor to the calculation of continental slope acoustic propagation. The MEVA 5 data, described in this thesis, showed the measured direction of propagation of a normal-mode wave was different from the direction expected from the source to the receiver. The MF mismatch can be explained in the context of horizontal ray paths.

6.2 Matched-Field Localization

Observations of matched-field localization (azimuth assumed known) confirmed MF-OAR model validation by demonstrating reasonable ambiguity surfaces with range errors from 70 m to 220 m. Depth errors ranged from 0-20 m. Geoacoustic estimations also proved to be reliable.

The tracking results of matched-field localization (azimuth assumed unknown) provided striking evidence that the symmetry breaking of the continental slope allows the means for bearing resolution with the VLA. As expected, the greatest bearing resolution was found for the cross slope propagation paths, from about 1910 hrs to 1930 hrs. The range-bearing discrimination is very good for these later times along the arc where the change in the field (or transmission loss) per unit angle is greatest. The performance was not as good near the end of the linear radial; this result may also indicate mismatch in the geoacoustic model at the deeper portion of the slope; or an accumulation of error due to the bathymetry. The range versus time tracking plot of the source is dramatic. This plot leaves little doubt of the target position and tracking over time.

The importance of these results comes as a product of the many years and published works from the acoustic community in pursuing matched-field processing. Bucker (1976) assessed early that a more general processing scheme may be more effective in detecting and localizing a target than by conventional plane wave beamformers. Source localization using matched-field processing for a moving source has been very limited over the years (e.g., Perkins and Kuperman 1990; Daugherty and Lynch 1990; Tran and Hodgkiss 1991). Limitations of a moving source introduces inaccuracies of an ever changing environment and the propagating effects subsequently varies significantly in the signal-to-noise ratio (SNR) (Perkins, Fialkowski *et al.* 1996). Only during the past two years have efforts been realized to track and detect a moving target (Wilmot *et al.* 1993; Perkins, Fialkowski *et al.* 1996; Wilmot *et al.* 1996; Wilmot *et al.* 1997). However, the results of the latter references show localizations and trackings that are estimated by reducing environmental parameters and focusing on limited data.

Overall, the results presented in this thesis demonstrate remarkably good tracking performance using linear MFP with a vertical line array over a sloping bottom in a very realistic set of environmental conditions. The very fact that the moored VLA was drifting at a rate of 0.15 kts (or 0.25 km/hr) shows the difficulty in fixing a frame of reference. Comparatively, the results show that environmental databases allow for quick and efficient access to spatially varying parameters to fully exploit the acoustic environment. The goal, as stated in the introduction, was to produce viable MF tracking in a littoral, shallow water region. The results demonstrated in this thesis met this aim. These results are in fact unique and present a process by which future target localizations and tracking can progress.

6.3 Concepts and Scope of Matched-Field Tracking

The effects of a sloping bottom in a shallow water environment is clear; the breaking symmetry of the bottom allowed a vertical aperture to effectively detect precise target *bearings*, along with accurate *range* and *depth*. However, not all littoral regions will have a sloping bottom with a gradient sufficient to produce distinct MF bearings. In such a case, either a combination of two vertical arrays (VLA) to cross-fix ranges (Wilmot *et al.* 1996) or a tilted VLA to create the much needed horizontal aperture could effectively cover an area or region for underwater surveillance.

The 13 hours of CPU processing in excess of the "real-time" 80 minutes target tracking (section 5.5) can be rectified by introducing parallel MF processing. The CPU used in this research was a standard Pentium type CPU architecture. Each bearing radial of investigation took approximately 20-30 secs to process with this CPU. In an effort to reproduce "real-time" localization, a system of parallel CPU processors could be implemented to allow real-time detection, where each bearing radial within an arc of investigation could be processed in parallel, simultaneously, by an independent CPU. Based on the localization times found in this experiment, the parallel processing may perhaps produce results 30 to 60 seconds delayed time after the raw signal has been received.

6.3.1 Defence Needs for Progress in Matched-Field Processing Localization and Tracking Techniques

Chapter 1 of this thesis summarized the developments of *passive* acoustic systems and developments since WWI and WWII. As stated earlier, efforts to maintain readiness with respect to underwater warfare often fluctuates with public awareness and perceived underwater threats. Defence cutbacks are a reality and maintaining a combat ready fleet is an even greater challenge. The submarine proliferation to

every corner of the world raises a problem not ever seen in modern underwater warfare. Submarines are in fact getting quieter and the conventional submarine detection and surveillance capability in shallow and littoral waters has been noted as a major operational deficiency. Methods combined with tactical environmental assessments and data. Matched-field processing, localization and tracking techniques are *non-conventional* beamforming methods that are still being treated, in Canada, as a purely scientific initiative without devoting serious consideration to further integrate these techniques into modern underwater warfare. The results and processes demonstrated in the previous chapters of this thesis present the case that matched-field is a logical progression from conventional beamforming (Goldsberry 1996) and requires serious consideration to further this area of signal processing. This is particularly true if passive sensors are to provide useful operational capability against the quiet modern diesel-electric submarine. tracking that is required to further our capabilities in underwater target detection.

6.3.2 Rapid Environmental Assessment (REA)

Rapid Environmental Assessment is becoming an area of operational concern with many of the world's navies that are increasing their involvement in international peacekeeping efforts. These efforts are often in littoral environments and have become more frequent in recent times. Therefore, detailed route survey and environmental databases must be completed in advance of any deployment or any short fused operations.

Operational matched-field tracking with either a deployed mobile VLA or a towed horizontal array system would be an effective tool to analyse and make use of the data collected from any REA. Canada has begun to receive new Maritime Coastal Defence Vessels (MCDVs) that are fitted with advanced and powerful side-scan sonars and have the ability to collect acoustic, environmental and bottom data. Once again, the data collected from these vessels, either along our home shores or abroad, is essential

and can be effectively used in matched-field databases.

This method of advanced beamforming techniques may make passive arrays operationally useful against quiet targets in littoral warfare. With these underwater signal processing methods combined with tactical environmental assessments and data gathering, the surface naval fleet may have gained a tactical acoustic advantage over underwater targets, perhaps for the first time since the arrival of the submarine 50 years ago. The potential applicability of fixed coastal surveillance arrays, when combined with rapid environmental assessment methods and matched-field processing, to deployed systems (e.g., sonobuoys, fields of distributed sensors, towed arrays and horizontal arrays, etc.) in forward operating areas demonstrates this possible advantage.

In conclusion, this is the progression, as shown in this thesis, of matched field processing and tracking that is required to further our capabilities in underwater target detection.

Chapman, N. R., Syck, J. M. and Carlow, G. R.

Vertical directionality of acoustic signals propagating downslope to a deep ocean receiver, in *Progress in Underwater Acoustics*, edited by H. M. Merklinger, pp. 573-579, Plenum Publishing Corporation, 1987.

Chapman, N. R., Jeremy, M. L., Ozard, J. M. and Wilmut, M. J.

Range dependence of matched-field source localization in shallow water, in *Symposium on Shallow Water Undersea Warfare - From Staging to Sustainment, Proceedings, Subgroup G - Undersea Warfare*, edited by Canadian Forces Maritime Centre, pp. 227-236, TTCP Halifax, NS 1996.

Canadian Navy

Chiu, C. and Ehret, L.

The effects of ocean environmental variability on underwater acoustic propagation forecasting, in *Oceanography and Acoustics - Prediction and Propagation Models*, edited by R. T. Beyer, pp. 7-49, AIP New York, Modern Acoustics and Signal Processing, New York 1994.

Chiu, C. and Ehret, L.

Three-dimensional acoustic normal mode propagation in the gulf stream, in *Oceanography and Acoustics - Prediction and Propagation Models*, edited by R. T. Beyer, pp. 179-197, AIP New York, Modern Acoustics and Signal Processing 1994.

References

- Collins, M. D.
A self-starter for the parabolic equation method, *J. Acous. Soc. Am.*, **92**, 2069-2074 (1992).
- Bell, T. G.
Sonar and Submarine Detection, U.S. Navy Underwater Sound Lab. Rep., 1962.
- Brekhovskikh, L. M. and Godin, O. A.
Acoustics of Layered Media II, Spinger-Verlag, Berlin 1992.
- Bucker, H. P.
Sound propagation in a channel with lossy boundaries, *J. Acous. Soc. Am.*, **48**, 1187-1194 (1970).
- Bucker, H. P.
Use of calculated sound fields and matched field detection to locate sound sources in shallow water, *J. Acous. Soc. Am.*, **59**, 368-373 (1976).
- Butkov, E.
Mathematical Physics, Addison-Wesley Publishing Company, Reading Massachusetts 1968.
- Chapman, N. R., Syck, J. M. and Carlow, G. R.
Vertical directionality of acoustic signals propagating downslope to a deep ocean receiver, in *Progress in Underwater Acoustics*, edited by H. M. Merklinger, pp. 573-579, Plenum Publishing Corporation, 1987.
- Chapman, N. R., Yeremy, M. L., Ozard, J. M. and Wilmut, M. J.
Range dependence of matched-field source localization in shallow water, in *Symposium on Shallow Water Undersea Warfare - From Staging to Sustainment, Proceedings, Subgroup G - Undersea Warfare*, edited by Canadian Forces Maritime Warfare Centre, pp. 227-236, TTCP Halifax, NS 1996.
- Chin-Bing, S. A. King, D. B. and Boyd, J. D.
The effects of ocean environmental variability on underwater acoustic propagation forecasting, in *Oceanography and Acoustics - Prediction and Propagation Models*, edited by R. T. Beyer, pp. 7-49, AIP New York, Modern Acoustics and Signal Processing, New York 1994.
- Chiu, C. and Ehret, L.
Three-dimensional acoustic normal mode propagation in the gulf stream, in *Oceanography and Acoustics - Prediction and Propagation Models*, edited by R. T. Beyer, pp. 179-197, AIP New York, Modern Acoustics and Signal Processing 1994.

- Collins, M. D.
A self-starter for the parabolic equation method, *J. Acous. Soc. Am.*, **92**, 2069–2074 (1992).
- Collins, M. D.
A split-step pade solution for parabolic equation method, *J. Acous. Soc. Am.*, **93**, 1736–1742 (1993).
- Collins, M. D.
User's Guide for RAM Versions 1.0 and 1.0p, 1995.
- Daugherty, J. R. and Lynch, J. F.
Surface wave, internal wave and source motion effects on matched-field processing in a shallow water waveguide, *J. Acous. Soc. Am.*, **87**, 2503–2526 (1990).
- Davis, E., Currie, R. and Sawyer, B.
Southern Vancouver Island Margin Bathymetry Chart, Map 7, Geological Survey of Canada, Pacific Geoscience Centre, Sidney, B.C. 1987.
- Doolittle, R. and Tolstoy, A.
Experimental confirmation of horizontal refraction of cw acoustic radiation from a point source in a wedge-shaped ocean environment, *J. Acous. Soc. Am.*, **83**, 2117–2125 (1988).
- Dosso, S. E.
Acoustic propagation in a continental slope ocean environment, Master's thesis, University of Victoria, Apr., 1982.
- Dosso, S. E., Jeremy, M. L., Ozard, J. M. and Chapman, N. R.
Estimation of ocean-bottom properties by matched-field inversion of acoustic field data, *IEEE J. Oc. Eng.*, **18**, 232–239 (1993).
- Fawcett, J. A., Jeremy, M. L. and Chapman, N. R.
Matched-field source localization in a range-dependent environment, *J. Acous. Soc. Am.*, **99**, 272–282 (1996).
- Felsen, L.
Benchmarks: An option for quality assessment, *J. Acous. Soc. Am.*, **87**, 1497–1498 (1990).
- Feuillade, C., Delbalzo, D. R. and Rowe, M.
Environmental mismatch in shallow water matched field processing: Geoacoustic parameter variability, *J. Acous. Soc. Am.*, **85**, 2354–2364 (1989).
- Frisk, G. V.
Ocean and Seabed Acoustics, PTR Prentice-Hall, Englewood Cliffs, New Jersey 1994.

- Gingras, D.
Methods for predicting the sensitivity of matched-field processing, *J. Acous. Soc. Am.*, **86**, 1940–1949 (1989).
- Goldsberry, T. G.
Introductory comments, in *Symposium on Shallow Water Undersea Warfare - From Staging to Sustainment, Proceedings, Subgroup G - Undersea Warfare*, edited by Canadian Forces Maritime Warfare Centre, pp. 5–9, TTCP Halifax, NS 1996.
- Hadley, M. L.
U-Boats against Canada, McGill-Queen's University Press, Kingston and Montreal, 1985.
- Hamilton, E. L.
Geoacoustic modeling of the sea floor, *J. Acous. Soc. Am.*, **68**, 1313–1340 (1980a).
- Hamson, R. and Heitmeyer, R.
Environmental and system effects on source localization in shallow water by the matched-field processing of a vertical array, *J. Acous. Soc. Am.*, **86**, 1951–1959 (1989).
- Hannay, D.
Broadband matched field processing for geacoustic parameter estimation, *Contractor Report 96/402SPK W7707-5-3243/01-HAL*, JASCO Research Ltd., July (1996).
- Hannay, D. and Chapman, N.R.
Coherent broadband matched field processing for geacoustic parameter estimation, *Proceedings of the 8th matched-field processing workshop*, pp. 163–169, Esquimalt Defence Research Detachment (EDRD) and Naval Command, Control and Surveillance Centre (NCCOSC), June (1996).
- Jensen, F. B. and Ferla, C. M.
Numerical solutions of range-dependent benchmark problems in ocean acoustics, *J. Acous. Soc. Am.*, **87**, 1499–1510 (1990).
- Jensen, F. B., Kuperman, W. A., Porter, M. B. and Schmidt, H.
Computational Ocean Acoustics, American Institute of Physics, New York 1994.
- Ozard, J. M., Jeremy, M. L., Chapman, N. R., Wilmut, M. J. and Musil, M.
Three-dimensional matched-field processing and tracking in a range-dependent shallow water environment in the north-east pacific ocean, in *Symposium on Shallow Water Undersea Warfare - From Staging to Sustainment, Proceedings, Subgroup G - Undersea Warfare*, edited by Canadian Forces Maritime Warfare Centre, pp. 105–114, TTCP Halifax, NS 1996.

- Ozard, J. M., Jeremy, M. L., Chapman, N. R. and Wilmut, M. J.
Matched-field processing in a range-dependent shallow water environment in the north-east pacific ocean, *IEEE J. Oc. Eng.*, **21**, 377-383 (1996).
- Perkins, J. S. and Kuperman, W. A.
Three-dimensional matched-field processing with a vertical array, *J. Acous. Soc. Am.*, **87**, 1553-1556 (1990).
- Perkins, J. S., Kuperman, W. A., and Evans, R. B.
Three-dimensional oceanographic acoustics: Propagation, noise and array processing, in *Oceanography and Acoustics - Prediction and Propagation Models*, edited by R. T. Beyer, pp. 161-178, AIP New York, Modern Acoustics and Signal Processing, 1994.
- Perkins, J. S., Fialkowski, L. T., Fawcett, J. A. and Kelly, L. J.
Matched-field source tracking using TESPEX 2 data, in *Symposium on Shallow Water Undersea Warfare - From Staging to Sustainment, Proceedings, Subgroup G - Undersea Warfare*, edited by Canadian Forces Maritime Warfare Centre, pp. 105-114, TTCP Halifax, NS 1996.
- Pickard, G. L. and Emery, W. J.
Descriptive Physical Oceanography - An Introduction, Pergamon Press, Oxford 1990.
- Pierce, A. D.
Extension of the method of normal modes to sound propagation in an almost-stratified medium, *J. Acous. Soc. Am.*, **37**, 19-27 (1965).
- Porter, M. B., Dicus, R. L. and Fizell, R. G.
Simulations of matched-field processing in a deep-water pacific environment, *IEEE J. Oceanic Eng*, **12**, 2280-2284 (1991).
- Press, W. H., Flannery, B. P., Teukolsky, S. A. and Vetterling, W. T.
Numerical Recipes - The Art of Scientific Computing, pp. 103-105, Cambridge University Press, 1989.
- Robinson, A. R., and D. Lee
Introduction: Ocean variability, acoustic propagation and coupled modes, in *Oceanography and Acoustics - Prediction and Propagation Models*, edited by R. T. Beyer, pp. 2-3, AIP New York, Modern Acoustics and Signal Processing, New York 1994.
- Spence, .
Cruise Report, University of Victoria, Victoria 1996.

- Thomson, R. E.
Oceanography of the British Columbia Coast, pp. 233–234, Department of Fisheries and Oceans, Vancouver 1981.
- Tolstoy, A.
Sensitivity of matched field processing to sound speed profile mismatch for vertical arrays in a deep water pacific environment, *J. Acous. Soc. Am.*, **85**, 2394–2404 (1989).
- Tolstoy, A.
Matched Field Processing for Underwater Acoustics, pp. 1–, World Scientific, 1993.
- Tolstoy, I.
Resonant frequencies and high modes in layered wave guides, *J. Acous. Soc. Am.*, **28**, 1182–1192 (1956).
- Tran, J. M. Q. D and Hodgkiss, W. S.
Matched-field processing of 200-Hz continuous wave (cw) signals, *J. Acous. Soc. Am.*, **89**, 745–755 (1991).
- Urlick, R. J.
Principles of Underwater Sound, McGraw-Hill Book Company, New York 1975.
- Urlick, R. J.
Sound Propagation in the Sea, Peninsula Publishing, Los Altos CA 1982.
- Westwood, E. K. Tindle, C. T. and Chapman, N. R.
A normal mode model for acousto-elastic ocean environment, *J. Acous. Soc. Am.*, **100**, 3631–3645 (1996).
- Westwood, E. K.
ORCA code and User's Guide (Ver 1.0), Feb. 1996.
- Wilmot, M.J., Ozard, J.M. and Woods, B.
An efficient target tracking algorithm for matched-field processing, *OCEANS 93*, **III**, 81–85 (1993).
- Wilmot, M.J., Ozard, J.M. and Brouwer, P.
Evaluation of two efficient target tracking algorithms for matched-field processing with horizontal arrays, *J. Comp. Acous*, **3**, 311–326 (1996).
- Wilmot, M.J., Ozard, J.M. and Yeremy, M.L.
Tracking in range versus time with application of matched-field processing of a vertical line array data, *Can. J. Acoust.*, **25**, 21–27 (1997).

Appendix A

OAR - IDL Codes

```
readf, lun, dum1, dum2, dum3, dum4, dia
grdepth=fltarr(dia, dia)
grlon=fltarr(dia)
grlat=fltarr(dia)
xaxis = findgen(dia)
yaxis = findgen(dia)
```

A.1 Reading Lookup Tables

variables:

pmm, *emm* = number of modes

phh, *ehh* = number of pre-calculated depths

pdpts = number of depth points

PRO TABLES

```
file1 = strcompress('/user/.../project/oar/lookup_tables/EIG_LOOKUP', /remove_all)
```

```
file2 = strcompress('/user/.../project/oar/lookup_tables/PHI_LOOKUP', /remove_all)
```

```
openr, lun1, file1, /get_lun
```

```
openr, lun2, file2, /get_lun
```

```
;
```

```
readu, lun1, startdepth
```

```
readu, lun1, emm, ehh
```

```
eig_table = complexarr(emm, ehh)
```

```
readu, lun1, eig_table
```

```
free_lun, lun1
```

```
readu, lun2, pmm, pdpts, phh
```

```
phi_table = complexarr(pmm, pdpts, phh)
```

```
readu, lun2, phi_table
```

```
free_lun, lun2
```

```
END
```

A.2 Radial depths and coordinate information

```
lon = interpol(xaxis, grlon, reflon)
```

```
;
```

```
refdep = interpol(yaxis, grdepth, lon, lat)
```

```
openr, lun, '/user/.../project/charts/bath4.dat', /get_lun
```



```

; = (indgen(enh)*5)+startdepth
; = PREP LATS & LONS FOR INTERPOLATION
range = (srange+1000.)
rr = fix((range/delr) +1)
radrange = fltarr(2,rr)erator & denominator
; OR ii = 0,emm-1 DO BEGIN
range = range/1852./60_table(ii,*)x,radhh)
delr = delr/1852./60
conv = cos(49.08*!pi/180) ;49.08 is the project site mid-latitude
ii = 0
FOR r = 0.,range,delr DO BEGIN
  y = reflat + (r*cos(theta*!pi/180))
  x = reflon - (r*sin(theta*!pi/180))/conv
; INTERPOLATE RADIAL DEPTHS
  lat = interpol(yaxis,grlat,y)
  lon = interpol(xaxis,grlon,x)
  dep = interpolate(grdepth,lon,lat)
  radrange(0,ii) = r*111120.
  radrange(1,ii) = dep
  ii = ii+1
ENDFOR
free_lun,lun
END
phi_nxr = interpolate(phi_table,x,y,rpts,/grid)

```

A.3 Wave number interpolation and integration

variables: *radrange* is defined in another module that calculated the changes in depth *radrange(1,*)* along a radial length *radrange(0,*)*.

```

const = (1/(rho*sqrt(8*pi)))*exp(i*pi/4)
kph_n = dcomplexarr(rr,emm)
kph_d = dcomplexarr(rr,emm)
k_tmp = dcomplexarr(rr)

```

```

x = (findgen(ehh)*5)+startdepth
xx = findgen(rr)*delr
radhh = radrange(1,*)
; a = dcomplexarr(rr,emm)
; = integrating the numerator & denominator
FOR ii = 0,emm-1 DO BEGIN
  k_tmp = interpol(eig_table(ii,*),x,radhh)
  kph_n(0,ii) = 0.00001 * table(ii,*),x,radhh)
  kph_d(0,ii) = 1.
ENDFOR
FOR ij = 1,rr-1 DO BEGIN
  kph_n(ij,ii) = kph_n(ij-1,ii) + (0.5*delr)*(k_tmp(ij) + k_tmp(ij-1))
  kph_d(ij,ii) = kph_d(ij-1,ii) + (0.5*delr)*(1/k_tmp(ij) + 1/k_tmp(ij-1))
ENDFOR
; calculating NEVA h/p position: 'source,' [m]
ENDFOR /ix(source/5.)

```

A.4 Mode function interpolation

```

sum = phi_mzr(0,xa,0) + phi_mzr(0,*,r) = $
  (exp(i*kph_n(r,0))/sqrt(kn(0,0)*kn(r,0)+kph_d(r,0)))
FOR r = 0,rr-1 DO BEGIN
  sum = phi_mzr(0,xa,0) + phi_mzr(0,*,r) + $
    (exp(i*kph_n(r,m))/sqrt(kn(0,m)*kn(r,m)+kph_d(r,m)))
ENDFOR
x = findgen(emm)
y = findgen(pdpts)
z = findgen(ehh)
hh = (findgen(ehh)*5)+startdepth
rpts = interpol(z,hh,radhh)
phi_mzr = dcomplexarr(emm,pdpts,rr)
phi_mzr = interpolate(phi_table,x,y,rpts,/grid)
p_field = const*adiab

```

A.5 Adiabatic summation

```

const = (sqrt(2*pi)/(rho))*exp(i*pi/4)
; const = (1/(rho*sqrt(8*pi)))*exp(i*pi/4)
;
nh = 16.

```

```

adiab = dcomplexarr(rr,pdpts,nh)
phi = dcomplexarr(pdpts)
sum = dcomplexarr(pdpts)
kn = dcomplexarr(rr,emm)
x = (findgen(ehh)*5)+startdepth
;
FOR ii = 0,emm-1 DO BEGIN
    k_tmp = interpol(eig_table(ii,*),x,radhh)
    kn(*,ii) = k_tmp(*)
ENDFOR
ss = 0
FOR source = 90,315,15 DO BEGIN
print,ss+1,' calculating MEVA h/p position: ',source,' [m]'
    zs = fix(source/5.)
;    adiabatic sum
    FOR r = 0,rr-1 DO BEGIN
        sum = phi_mzr(0,zs,0) * phi_mzr(0*,r) * $
            (exp(i*kph_n(r,0))/sqrt(kn(0,0)*kn(r,0)*kph_d(r,0)))
        FOR m = 1,emm-1 DO sum = sum + (phi_mzr(m,zs,0) * phi_mzr(m*,r) * $
            (exp(i*kph_n(r,m))/sqrt(kn(0,m)*kn(r,m)*kph_d(r,m))))
        adiab(r*,ss) = sum(*)
    ENDFOR
    ss = ss+1
ENDFOR
print,'enter OAR field file name & time (ie oar1920)' & read,file
p_field = const*adiab
;
openw,lun,'/user/.../project/oar/OAR_DATA/'+file,/get_lun
printf,lun,fix(rr),fix(pdpts),fix(nh)
writeu,lun,p_field
free_lun,lun
END

```

Appendix B

MFP - IDL Codes

B.1 Linear Processor: Bartlett

```

;help,replica
free_lun,lun
1
dpts=84
; NORMALISE THE FIELDS
print,'bartlett processing ...'
PRO BARTLETT(rpts,dpts)
common para1
common para2
;
; GET MEASURED DATA
ff1 = ' '
print,' '
print,'enter desired covariance (ie cov1920):' & read,ff1
openr,lun,'/user/ ... /covariance/' + ff1,/get_lun
readf,lun,nh,hr,min
nh = fix(nh)
Cov = complexarr(nh,nh)
readf,lun,Cov
free_lun,lun
print,' '
;help,Cov
;
; GET REPLICATED / MODELED DATA
ff2 = ' '
print,'replica file (ie oar1920):' & read,ff2
openr,lun,'/user/ ... /OAR_DATA/' + ff2,/get_lun
readf,lun,rpts,dpts,nh
print,' '
;print,'range pts:',rpts,' depth pts:',dpts,' h/p:',nh
replica=dcomplexarr(rpts,dpts,nh)
readu,lun,replica

```

```
;help,replica
free_lun,lun
;
dpts=84
; NORMALISE THE FIELDS
print,'bartlett processing ...'
w = complexarr(nh)
PBart = fltarr(rpts,dpts)
FOR d = 0,dpts-1 DO BEGIN
  FOR r = 0,rpts-1 DO BEGIN
    FOR n=0,nh-1 DO w(n) = replica(r,d,n) ;* = nh (number of h/p)
    w = w/float(sqrt(total(w*conj(w))))
    CTw = transpose(conj(w))
;
; BARTLETT PROCESSOR'
;
    PBart(r,d) = (CTw#Cov#w)
  ENDFOR
ENDFOR
openw,lun,'PBartlett.dat',/get_lun
printf,lun,PBart
free_lun,lun
;help,PBart
print,' '
END
```

Partial Copyright License

Vita

Surname: Taillefer

Given Names: Martin Luc

Place of Birth: Montreal, Quebec, Canada

Educational Institutions Attended:

Le College Militaire Royal de St-Jean, P.Q. 1981-1984

Royal Roads Military College, Victoria, B.C. 1984-1987

Diplomas & Degrees Awarded:


D.E.C. Sciences et ingenierie, CMR 1984

Bachelor of Science, RRMC 1987

Honours & Awards:

Canadian Decoration 1994

Author:



Lieutenant(N) Martin L. Taillefer

May 30, 1998

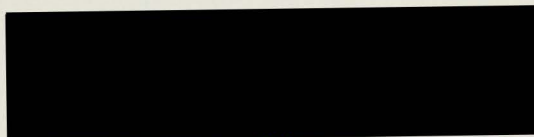
Partial Copyright License

I hereby grant the right to lend my thesis to users of the University of Victoria Library, and to make single copies only for such users or in response to a request from the Library of any other university, or similar institution, on its behalf or for one of its users. I further agree that permission for extensive copying of this thesis for scholarly purposes may be granted by me or a member of the University designated by me. It is understood that copying or publication of this thesis for financial gain shall not be allowed without my written permission.

Title of thesis:

Range Dependent Matched Field Source Localization and Tracking
in Shallow Water on a Continental Slope Region of the
North-East Pacific Ocean

Author:



Lieutenant(N) Martin L. Taillefer

May 30, 1998